Measuring plastic deformation of silicon as a result of thermal oxidation

K. V. Sweers

Report no	: 2018:043
Coaches	: Dr. ir. N. Tolou, Ir. P.R. Kuppens
Professor	: Prof dr. ir. J.L. Herder
Specialisation	: Mechatronic System Design
Type of report	: Master Thesis
Date	: 5 December, 2018

TU Delft Delft University of Technology

Challenge the future

Preface

This thesis would not have been possible without some help and support. I want to thank my supervisor Nima Tolou, for the insightful discussions on the project direction. I want to thank my daily supervisor Reinier Kuppens, especially for the detailed feedback on my writing. The experiments would not have been possible without the Else Kooi Laboratory. I especially want to thank Jia Wei, for the help with fabrication, oxidation, and all processes performed in the lab. Finally, I want to thank my parents for their continued support.

ii

Abstract

Thermal oxidation in silicon microelectromechanical systems (MEMS) induces stress in the oxide film and silicon. Such residual stresses are usually unwanted, as it can influence performance or damage components. It can also cause unwanted plastic deformation in silicon, as was observed in previous research. Current measurement methods in MEMS are not able to distinguish plastic and elastic strain as a result of thermal oxidation. This thesis presents a novel method to distinguish elastic and plastic strain in silicon beams, by removing the oxide layer to show the plastic strain. A lever mechanism is used as a mechanical amplifier. The plasticity model developed by Alexander and Haassen (AH) is used in a numerical model to predict the elastic and plastic strain. Experiments in epitaxially grown silicon show significantly less plastic strain than predicted by the model. We conclude that the AH model is not valid for epitaxially grown silicon with low or zero initial dislocations. As significant plastic deformation was observed in FZ silicon samples in previous research by P.R. Kuppens, it is concluded that epitaxially grown silicon is the better choice when plastic deformation is to be avoided.

Contents

1 Introduction **1**

2 Paper: Measuring plastic deformation in epitaxial silicon after oxidation **5**

3 Literature review: A review of methods for measuring residual stress and plastic deformation in MEMS **17**

4 Reflection **33**
- 4.1 Line of thought . . . 33
- 4.2 Work timeline . . . 34
- 4.3 Contributions . . . 34
- 4.4 Recommendations . . . 35

5 Conclusion **37**

A Modeling **39**
- A.1 Numerical model . . . 39
- A.2 FEM model . . . 48
- A.3 Model verification . . . 50

B Lever mechanism analysis **57**
- B.1 Buckling analysis . . . 57
- B.2 Stiffness analysis . . . 61
- B.3 Sensitivity analysis . . . 63

C Mask design **65**

D Sample images **69**

E Sample holder drawings **71**

F Measurement data **77**

Chapter 1

Introduction

Residual stresses can be a problem in Micro Electro Mechanical Systems (MEMS). MEMS find applications in many daily used products such as accelerometers and gyroscopes in smartphones, pressure sensors in airbags, and inkjet printheads. MEMS are often preferable over conventional size alternatives, as they are small, energy efficient, and easily integrated in electric circuits. Some effects of residual stress are damaged components [1], buckling of thin beams[2], and change of sensitivity of sensors[3].

Several steps of deposition, lithography, and etching are used to build a MEMS device layer by layer. Unfortunately, in almost all depositions of layers stress is introduced. For instance in silicon dioxide, which is commonly used as a sacrificial layer in the etch process, or as electrical insulation. The main cause of stress is the difference in coefficient of thermal expansion (CTE) between the silicon dioxide and the silicon bulk. The oxide film is typically grown at temperatures between 800 °C and 1200 °C, and during cooling the silicon wants to shrink more than the oxide. Since they are connected, a stress is induced in both materials to ensure equal strain in both materials.

Residual stress is not always bad, it can also be exploited. P.R. Kuppens used the residual stress of thermal oxidation to add negative stiffness to a compliant stage, to achieve static balancing. Contrary to normal compliant stages, no energy is needed to move such a stage, as it is at static equilibrium over a certain range of motion. Stiffness reduction also reduces the eigenfrequency, which can be beneficial for energy harvesting or sensor applications.

However, it was observed that the residual stress caused some unexpected plastic deformations in the silicon flexures. The stress in the oxide film stretched the flexures, causing a buckling effect. The oxide film was removed afterwards, and the buckled shape was still present. This indicates plastic deformation, as the stress was removed by stripping the oxide. The buckled shape after oxide removal is shown in Fig. 1.1. The stage should be exactly in the middle if there is no plastic deformation, but you can clearly see that the stage is buckled sideways. At high temperatures silicon starts to behave ductile, while it is very brittle at low temperatures. It is believed that the plastic deformations occurred in this ductile regime during cooling to room temperature.

More insight in plastic deformation of silicon members as a result of thermal oxidation is needed, either to avoid plastic deformations where unwanted, or to exploit the possibilities it might bring. To design devices that use thin film stress from oxidation, it is necessary to know how to minimize or prevent plastic deformation. Applications can include static balancing as proposed by P.R. Kuppens, or other forms of preloading. It will also bring new possibilities. For example, out of plane plastic deformations could potentially be achieved in a passive way using thermal oxidation. Kim et al. [4] have plasticly deformed silicon torsion bars using mechanical touch. If we can control plastic deformation

as a result of thermal oxidation, such deformations can be achieved passively, which makes it faster and cheaper to produce. Out of plane deformations give a new dimension to the usual planar design space of MEMS.

To gain more insight in plasticity in silicon as a result of thermal oxidation, we need to be able to measure this quantitatively. A literature review was done on measurement methods for residual stress from thin film in MEMS, with a special interest in measurements of plastic deformations. It was found that many methods exist to measure elastic strain, but none are designed for plastics strain measurements.

This thesis presents a novel method to distinguish elastic and plastic strain in silicon beams, by removing the oxide layer to show the plastic strain. A lever mechanism is used as a mechanical amplifier. The plasticity model by Alexander and Haassen (AH) is used in a numerical model to predict the elastic and plastic strain. Experiments in epitaxially grown silicon show significantly less plastic strain than predicted by the model. We conclude that the AH model is not valid for epitaxially grown silicon with low or zero initial dislocations. As significant plastic deformation was observed in FZ silicon samples from P.R. Kuppens, it is concluded that epitaxially grown silicon is the better choice when plastic deformation is to be avoided.

The main body of this thesis is presented as a paper in chapter 2. It describes the design of a measurement method to distinguish elastic and plastic strain, the analysis and modeling, and experimental results. Chapter 3 presents the literature review on measurement methods for residual stress. It is followed by a reflection in chapter 4.4, and a conclusion in chapter 5. The model details can be found in appendix A. Appendix B contains extra analysis on the lever mechanism. The mask design for the experimental samples is included in appendix C. Additional sample images are shown in appendix D. Customized containers were made to store the samples safely. Drawings of these sample holders can be found in appendix E. Appendix F contains the raw measurement data.

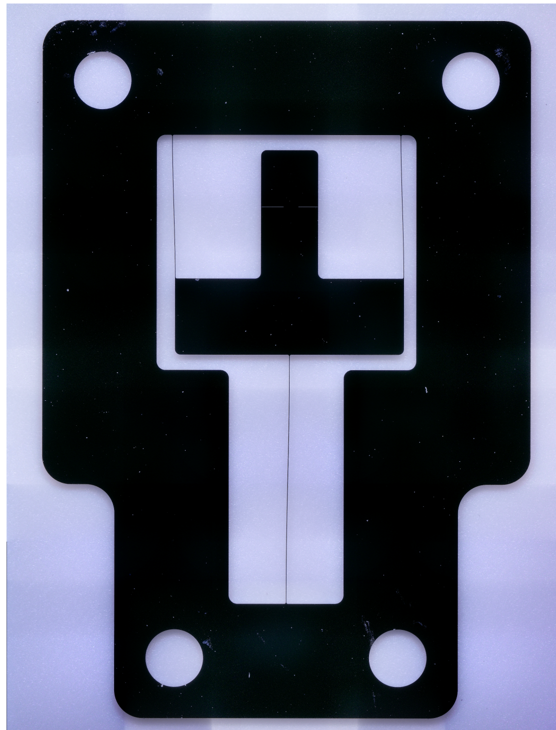

Figure 1.1: Statically balanced stage by P.R. Kuppens after removal of oxide film. It is shown that the stage is slightly buckled to the right, indicating plastic deformation.

Chapter 2

Paper: Measuring plastic deformation in epitaxial silicon after oxidation

Measuring plastic deformation in epitaxial silicon after oxidation

K.V. Sweers, P.R. Kuppens, N. Tolou
Corresspondent author: P.R. Kuppens

December 5, 2018

Abstract

Residual stress from thermal oxidation can cause plastic deformation in silicon microelectromechanical systems (MEMS). This paper presents a novel method to distinguish elastic and plastic strain in silicon beams, by removing the oxide layer to show the plastic strain. A lever mechanism is used as a mechanical amplifier. The plasticity model by Alexander and Haassen (AH) is used in a numerical model to predict the elastic and plastic strain. Experiments in epitaxially grown silicon show significantly less plastic strain than predicted by the model. We conclude that the AH model is not valid for epitaxially grown silicon with low or zero initial dislocations. As significant plastic deformation was observed in FZ silicon samples in previous research by the authors, it is concluded that epitaxially grown silicon is the better choice when plastic deformation is to be avoided.

1 Introduction

Thermal oxidation in silicon microelectromechanical systems (MEMS) induces stress in the oxide film and bulk silicon. This residual stress causes deformations in the silicon, which can be partially plastic under certain conditions. These plastic deformations are not completely understood yet. Some effects of residual stress in MEMS include damage [1], warpage [2], reduced sensitivity of ultrasonic sensors [3], and buckling [4].

Thermal oxide is typically used as a sacrificial layer in the etch process, or for electrical insulation. It is grown in an oxygen rich environment, at high temperatures typically ranging from 800 °C to 1200 °C to speed up the process. When cooling down to room temperature, the mismatch of the coefficient of thermal expansion (CTE) is the main cause for stress. At these high temperatures silicon behaves ductile, in contrast to the very brittle behavior at room temperature. Usually the film is very thin compared to the silicon bulk, so stress in the bulk is low and no plastic strain occurs. For relative thicker oxide compared to the bulk, significant plastic deformation was observed by previous research of the authors.

Literature provides many methods to measure residual stress and strain in thin films. The most common method is to measure the wafer curvature [5, 6], and calculate thin film stress using the Stoney equation [7]. Some of other commonly used methods include buckling beams [8, 9, 10], piezo [11, 12], motion amplifying mechanisms [13, 14, 15, 16], x-ray diffraction [17, 18]. Although these studies all measure strain, none make the distinction between elastic and plastic strain.

Measurements of the plastic behavior of oxidized thin silicon beams have not been done before. Better understanding of this behavior gives designers the insight to either avoid or exploit plastic deformation after oxidation. It could be used to permanently deform silicon members in a passive way, contrary to Frühauf et al. [19] and Kim et al. [20] who used active mechanical contact to obtain out of plane plastic deformations. Another application is to create preloading in silicon members [21]. This can be used to provide negative stiffness to compliant stages, to achieve overall stiffness reduction and low eigenfrequencies. Some examples where this is beneficial are energy harvesters and accelerometers [22].

This paper presents elastic and plastic strain measurements in epitaxial silicon beams, as a result of thermal oxidation. A novel measurement method is used to distinguish elastic and plastic strain, by removing the oxide film to show the plastic strain. A lever mechanism is used as a mechanical amplifier. Experiments are performed with different beam widths and oxidation temperatures. A numerical model is presented to predict elastic and plastic strain, which are compared to experimental results.

The working principle and design of the lever mechanism, as well as the modeling, are described in section 2. Experimental and theoretical results are presented in section 3. The results are discussed in section 4 and a conclusion is given in section 5.

2 Methods

2.1 Working principle

A silicon dioxide film is grown on the surfaces of silicon beams at elevated temperatures. EerNisse [23] has shown that silicon dioxide grows in a stress free state above the viscous flow point, which is between 950 °C and 975 °C. It is therefore assumed that the only cause for stress is the difference of CTE between silicon dioxide and silicon. A surface stress will be induced when the specimen cools down to room temperature. This surface stress in the silicon dioxide film induces a net axial tensile stress in the silicon cantilever beam. This stress causes elongation of

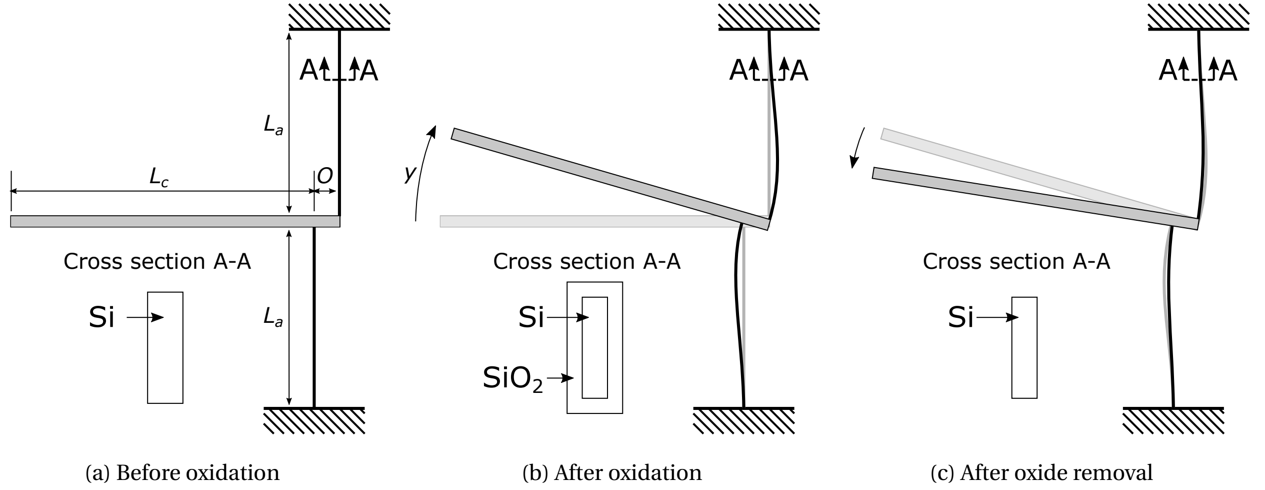

(a) Before oxidation (b) After oxidation (c) After oxide removal

Fig. 1: Working principle of the lever mechanism. Fig. 1a shows the initial position, before oxidation. Fig. 1b shows the position after oxidation. The beam rotates with tip displacement y because of the stress in beams L_A. After the oxide is removed, the elastic component of the strain is released. Only plastic deformation remains, which is shown in fig 1c.

the beam, which can have a plastic component besides an elastic one. Plastic deformation can theoretically occur if there is sufficient stress above the brittle-ductile transition temperature [24]. In thicker beams less stress is induced, and they will stretch less than thinner beams. The total strain, which can be measured at room temperature, is the sum of elastic and plastic strain. To distinguish these, the oxide film is removed in our method. This eliminates the source of stress in the silicon beam, so only the plastic strain remains. The measurement method proposed in this work uses this principle to separate elastic from plastic strain.

Elastic and plastic strains are expected to be in the order of 0.01 %. Without amplification, this would result in elongations in the order of 0.1 µm for 1 mm long beams, which is too small for accurate measurements. Therefore a lever mechanism is used to amplify the displacement, and obtain a sufficient measurement resolution. This type of mechanism is well known for thin film stress measurements [13, 14, 15, 16]. In these devices, the mechanism is etched in the thin film only. When it is freed from the underlying sacrificial layer, the film stress is released, causing the mechanism to rotate.

In this work, the mechanism is etched in a layer of epitaxial silicon, after which a silicon dioxide film is grown on all surfaces of the mechanism. The working principle of this mechanism is schematically shown in Fig. 1. Strain in beams L_a cause beam L_c to rotate. The small gap O and length of L_c amplifies this rotation, like a lever. The rotation is observed at the tip of the rotating beam, and is used to calculate the strain in beams L_a.

A vernier scale at the tip of the rotating beam is used to allow for easy read out of tip displacement under an optical microscope. An example measurement can be seen in fig. 7c.

Van Drieënhuizen et al. [16] derived the kinematic relation between strain ε and tip displacement y:

$$\varepsilon = \frac{y}{L_a\left(1+2\frac{L_c}{O}\right)} \tag{1}$$

For this relation, ideal joints are assumed. The dimensions are chosen based on fabrication and measurement limitations, and are $L_a = 1000\,\mu\text{m}$, $L_c = 4000\,\mu\text{m}$, and $O = 100\,\mu\text{m}$. The vernier scale is dimensioned to have a resolution of 1 µm tip displacement. With these dimensions, a strain resolution of 1.2×10^{-3} % is obtained.

A finite element method (FEM) analysis in COMSOL shows a deviation from this linear relation of Eq. 1, which can be seen in Fig. 2. It is found that a correction factor in the form of the second order polynomial from eq. 2 gives a good fit to the FEM data. A least squares fit on the FEM data in the range of 0 % to 0.14 % strain gives values for C_1 and C_2 of 1.0235 and 442.9039. With this fit, the maximum error in this range is reduced from 0.0093 % to 0.0005 % strain. Eq. 2 is used to calculate the strain from experimental tip displacement data.

$$\varepsilon = \frac{C_1 y + C_2 y^2}{L_a\left(1+2\frac{L_c}{O}\right)} \tag{2}$$

The elongation of the thin beams cause the lever mechanism to be under compressive load. To prevent undesired buckling, a buckling analysis is performed using the FEM model. The first linear buckling mode is sideways, as illustrated in fig. 3. A small perturbation in the form of this buckling mode is added to the initial shape in the FEM model, after which nonlinear time domain simulations are performed. The mechanism rotated as intended in the nonlinear analysis, instead of buckling sideways. Extreme values of beam widths and thermal stress are investigated to eliminate risk of buckling in the experimental devices.

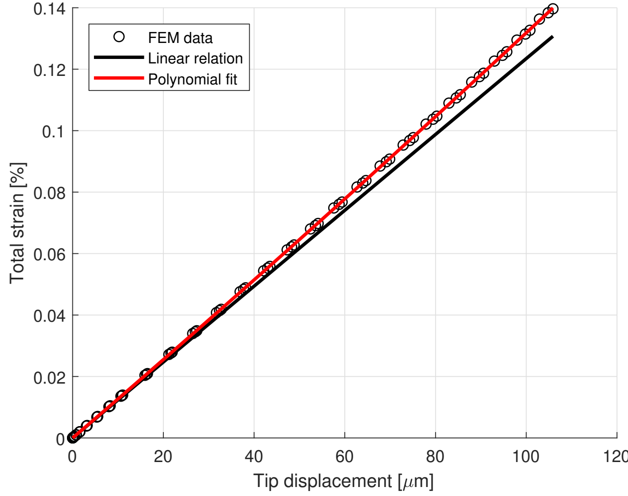

Fig. 2: Relation between tip displacement and strain. A polynomial fit gives a good approximation to the FEM data.

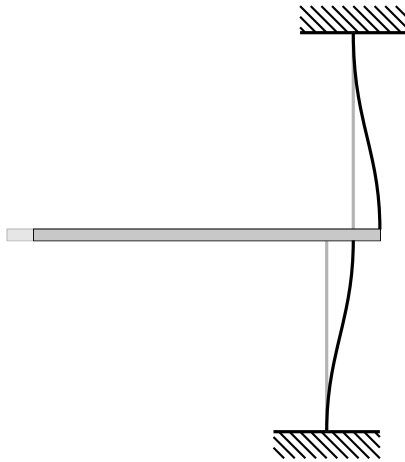

Fig. 3: First linear buckling mode.

2.2 Fabrication and measurements

A silicon on insulator (SOI) wafer is used with a 300 µm thick handling layer, 2 µm silicon dioxide layer, and a 50 µm thick epitaxial silicon layer in the (100) orientation. Deep reactive ion etching (DRIE) is used to etch the lever mechanisms in the epitaxial silicon layer from the front, and also from the backside to etch a cavity in the handling layer to release the mechanisms. A schematic of the cross section is shown in fig. 4. Samples are made with beams aligned to the <100> and <110> directions.

A 10 mm x 10 mm stepper mask is used. Each sample contains six rotating beams, as can be seen in fig. 6. Devices are fabricated with beam widths of 6.48 µm, 11.48 µm, and 16.48 µm, where overetching and consumed silicon by the silicon dioxide are considered. The target widths of the silicon beams after oxidation are 5 µm, 10 µm, and 15 µm. Each sample contains two devices of each beam width. Markers are etched to identify the beam width corresponding to the vernier scale, and to read the displacement of the scale. This is shown in fig. 7.

An silicon dioxide layer of 1 µm thick is grown using wet thermal oxidation at 900 °C, 950 °C, 1000 °C, 1050 °C, and 1100 °C. The oxide film is grown on all silicon surfaces, as shown in fig. 4. The oxidation times are calculated using the Deal-Grove model [25]. The samples are placed horizontally in the furnace, eliminating in-plane gravity effects. After oxidation, the furnace cools to 800 °C. The samples are annealed at this temperature for about 16 hours before they are removed from the furnace. The temperature profile is shown in Fig. 5. The oxide thickness is measured with spectral reflectance using the Leitz MPV SP at 3 different locations across the front side of the sample.

The oxide is removed with vapor hydrofluoric acid (VHF). For one beam of each width per sample, the width is measured with a Keyence VHX-6000 optical microscope at 3 locations. For one sample of <100> and <110>, the beam widths are also measured from the backside.

The strain measurement consists of multiple readouts in different stages of the fabrication process. The tip displacement is obtained by observing the vernier scales under a Keyence VHX-6000 optical microscope. An initial measurement is done before oxidation. The total strain, which is the sum of elastic and plastic strain, is measured after oxidation. The plastic strain is measured after the silicon dioxide is removed using the VHF.

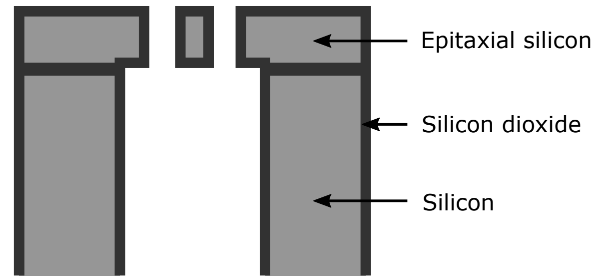

Fig. 4: Schematic of a the process.

2.3 Modeling

Stress and strain during cooling in oxidized fixed-free silicon cantilever beams, oriented in the <100> and <110> directions, are numerically modeled in MATLAB. Elongation of the thin beams cause an additional compressive stress in the thin beams, originating from the bending of the thin beams. The FEM model of the lever mechanism shows that this compressive stress from stiffness of the mechanism is negligible compared to the thermal stress in the silicon, and is thus neglected.

The total strain rate in silicon and silicon dioxide must be equal at their interface, and is assumed to be uniform throughout the cross section. This is verified by the FEM model. The total strain rate for both materials consists of elastic, plastic and thermal strain rates. The total strain

rate equation is given by:

$$\dot{\varepsilon}_{Si,th} + \dot{\varepsilon}_{Si,el} + \dot{\varepsilon}_{Si,pl} = \dot{\varepsilon}_{SiO_2,th} + \dot{\varepsilon}_{SiO_2,el} + \dot{\varepsilon}_{SiO_2,pl} \tag{3}$$

Where $\dot{\varepsilon}_{Si,th}$, $\dot{\varepsilon}_{Si,el}$ $\dot{\varepsilon}_{Si,pl}$ are the thermal, elastic, and plastic strain rates of the silicon, and $\dot{\varepsilon}_{SiO_2,th}$, $\dot{\varepsilon}_{SiO_2,el}$, and $\dot{\varepsilon}_{SiO_2,pl}$ the thermal, elastic and plastic strain rates of the silicon dioxide.

Plastic strain in silicon is governed by the movement of dislocations. As these crystallograhpic defects move, the lattice is rearranged causing permanent deformation. The silicon crystal structure contains 12 slip systems on which dislocations can move [26]. The resolved shear stress τ_r on a slip system is related to a tensile stress σ by the Schmid factor M:

$$\tau_r = \sigma M \tag{4}$$

M depends on the relative orientation of the tensile stress to the slip system. The slip systems with the highest resolved shear stress, and thus the highest Schmid factor, are considered active. The plastic strain rate for silicon is given by the Orowan equation [27]:

$$\dot{\varepsilon}_{Si,pl} = M n N_m v b \tag{5}$$

Where n is the number of active independent slip systems with Schmid factor M, N_m the mobile dislocation density for each slip system, v the average dislocation velocity, and b the length of the Burgers vector. The model by Alexander and Haassen (AH) is universally used to describe dislocation velocity and evolution of the dislocation density. The parameter values from Yonenaga and Sumino [28] are used in this model. The dislocation velocity v is:

$$v = B_0 \left(\frac{\tau_{eff}}{\tau_0}\right)^m \exp\left(\frac{-Q}{k_b T}\right) \tag{6}$$

Where B_0 is a reference velocity equal to $4.3 \times 10^4\,\mathrm{m\,s^{-1}}$, τ_{eff} the effective shear stress, τ_0 a reference stress, Q the activation energy, k_b the Boltzmann constant, and T the temperature.

The effective shear stress τ_{eff} is given by:

$$\tau_{eff} = \left\langle \sigma M - \frac{G b \sqrt{N_m}}{\beta} \right\rangle \tag{7}$$

Where G is the shear modulus, and β a parameter characterizing the interaction between dislocations. If $x > 0$, $\langle x \rangle = x$, and if $x \leq 0$, $\langle x \rangle = 0$. The dislocation density is assumed to increase proportionally to the area swept by the dislocations and the effective shear stress:

$$\dot{N}_m = K N_m v \tau_{eff} \tag{8}$$

Where K is a constant with value $3.1 \times 10^{-4}\,\mathrm{m\,N^{-1}}$.

Force equilibrium allows the axial stress in the silicon dioxide to be expressed by the stress in the silicon:

$$\sigma_{SiO_2} = \frac{-\sigma}{A_r} \tag{9}$$

Where σ_{SiO_2} is the axial stress in the silicon dioxide, and A_r the ratio of cross sectional area of silicon dioxide over silicon.

The plastic strain rate of silicon dioxide is modeled with a viscous flow model, as proposed by Irene et al. [29]. The plastic strain rate of the silicon dioxide is given by:

$$\dot{\varepsilon}_{SiO_2,pl} = \frac{-\sigma}{\eta A_r} \tag{10}$$

Where η is the temperature dependent velocity. The temperature dependence proposed by Irene et al. [29] is used.

Silicon is an anisotropic material, so the elastic modulus depends on the relative orientation to the crystal lattice. For uniaxial tension, the appropriate elasticity modulus E can be simplified to a single value [30]. The cantilever beams aligned with the <100> and <110> directions have elasticity moduli:

$$E_{si,100} = \frac{1}{s_{11}} \tag{11}$$

and

$$E_{si,110} = \frac{4}{2s_{11} + 2s_{12} + s_{44}} \tag{12}$$

where s_{11}, s_{12}, and s_{44} are components in the compliance tensor.

The second order temperature dependence of the components in the compliance tensor found by Bourgeois et al. [31] are used in this study. Even though this relation is based on measurements at lower temperatures, Swarnakar et al. [32] found similar values for higher temperatures and thus confirms validity. The elastic strain rate is given by:

$$\dot{\varepsilon}_{Si,el} = \frac{\dot{\sigma}}{E_{si}} \tag{13}$$

Silicon dioxide is modeled as an isotropic material. The elastic modulus E_{SiO_2} is assumed to be independent of temperature with a value of 64 GPa[33]. The elastic strain rate for silicon dioxide is:

$$\dot{\varepsilon}_{SiO2,el} = \frac{-\dot{\sigma}}{A_r E_{SiO_2}} \tag{14}$$

The thermal strain rates for silicon and silicon dioxide depend on the cooling rate $\dot{T}$ and the thermal expansion coefficient. For silicon, the thermal strain rate is:

$$\dot{\varepsilon}_{Si,th} = \alpha_{Si} \dot{T} \tag{15}$$

Where α_{Si} is the thermal expansion coefficient for silicon. The empirical formula proposed by Okada and Tokumaru [34] for the temperature dependence of α_{Si} is used in this model. There is an additional term in the axial thermal strain rate equation for silicon dioxide, because the lateral strain is fixed by the silicon. The thermal strain rate is:

$$\dot{\varepsilon}_{SiO_2,th} = \alpha_{SiO_2} \dot{T} + \left(\alpha_{SiO_2} - \alpha_{Si}\right) \nu \dot{T} \tag{16}$$

Where α_{Si} is the thermal expansion coefficient for silicon dioxide, and ν the Poisson ratio of silicon dioxide. The

temperature dependence determined by Tada et al. [33] is used.

The cooling process is modeled by solving the differential equations 5, 8, 10, 13, 14, 15, 16 numerically for $T(t)$ in MATLAB. The initial value for the dislocation density is assumed to be $1 \times 10^4\,\text{cm}^{-2}$ [35],[36].

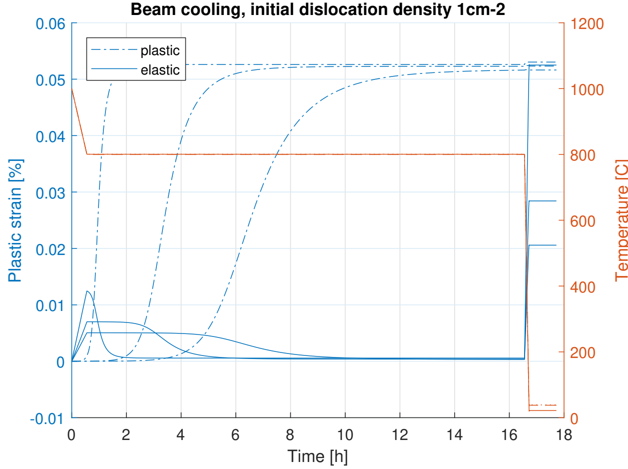

Fig. 5: Temperature profile for oxidation at 1000 °C, and elastic and plastic strain during cooling. Plastic strain from left to right resemble the beams with 5 µm, 10 µm, and 15 µm respectively.

3 Results

3.1 Characterization

Fig. 6 shows an example of a fabricated sample. The oxide thickness measurements can be seen in Tab. 1. For the samples oxidized at 1100 °C the oxide thickness was very close to the target. For the other samples, there was an increasing deviation from the target for samples oxidized at lower temperatures. The average measured beam width from the front are shown in tab. 1. The beam widths of the samples oxidized at 1000 °C were also measured from the backside. The beam widths from the backside are on average 1.22µm smaller then from the front side. The beam width measurements from the front side are corrected with this average when calculating A_r for comparison with the model.

3.2 Measurements

An example of a read out of the vernier scale is shown in fig. 7. The elastic and plastic strain measurements for the <100> and <110> aligned samples are plotted in fig. 8-12, together with simulation results with and without the plasticity model for silicon. In general, very little plastic strain was observed. An attempt to obtain larger plastic strains was made by growing 2µm oxide films at 1100 °C, with different annealing times. This did not result in larger strains, as seen in fig. 12.

The elastic strain was predicted well by the model where plasticity in silicon was disabled for most oxidation temperatures. The model underpredicted the elastic strain for oxidation at 900 °C, and overpredicted elastic strain for oxidation at 1100 °C with high A_r.

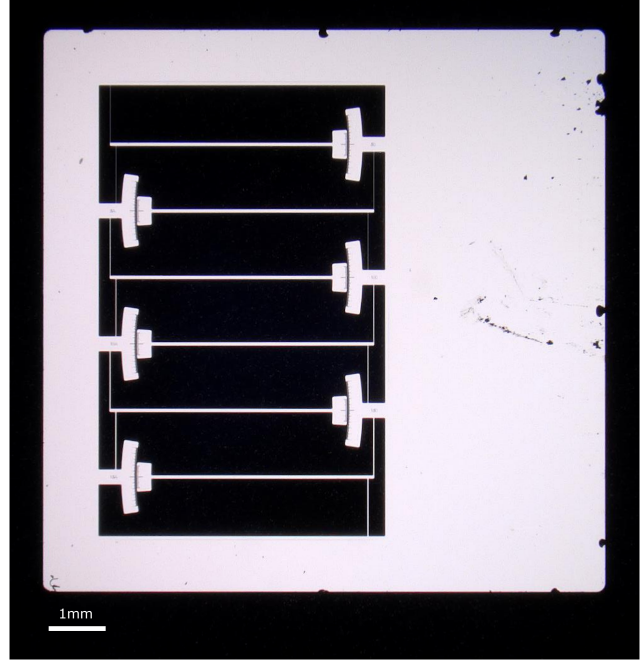

Fig. 6: Optical microscope image of a sample.

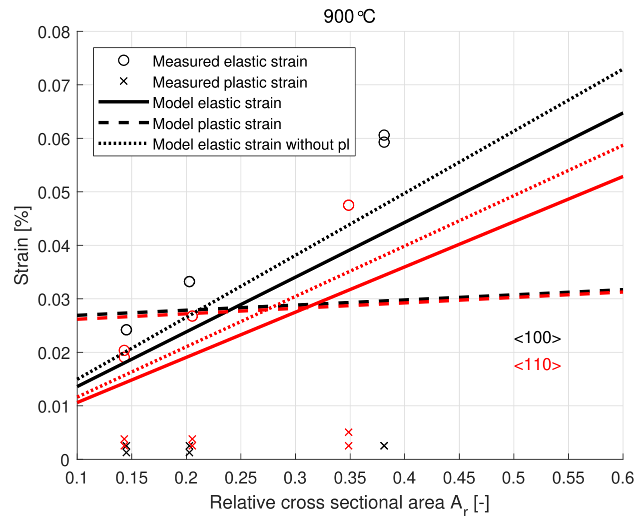

Fig. 8: Experimental and model results for elastic and plastic strain for oxidation at 900 °C.

Tab. 1: Process data

Oxidation temperature	Annealing time	Target thickness	Oxide thickness	<100> beam width in µm			<110> beam width in µm		
900 °C	60 h	1 µm	801 nm	5.35	10.30	15.25	5.84	10.15	15.51
950 °C	16 h	1 µm	940 nm	5.30	10.19	15.18	5.50	10.41	15.50
1000 °C	16 h	1 µm	965 nm	5.47	10.49	15.39	4.97	10.13	14.95
1050 °C	16 h	1 µm	986 nm	5.06	10.08	15.03	5.18	10.18	15.06
1100 °C	16 h	1 µm	1004 nm	4.42	9.70	14.67	4.90	9.71	14.91
1100 °C	16 h	2 µm	1994 nm	2.92	7.73	12.67	2.80	7.51	12.49
1100 °C	30 h	2 µm	1996 nm	2.91	7.85	12.56	2.81	7.72	12.74

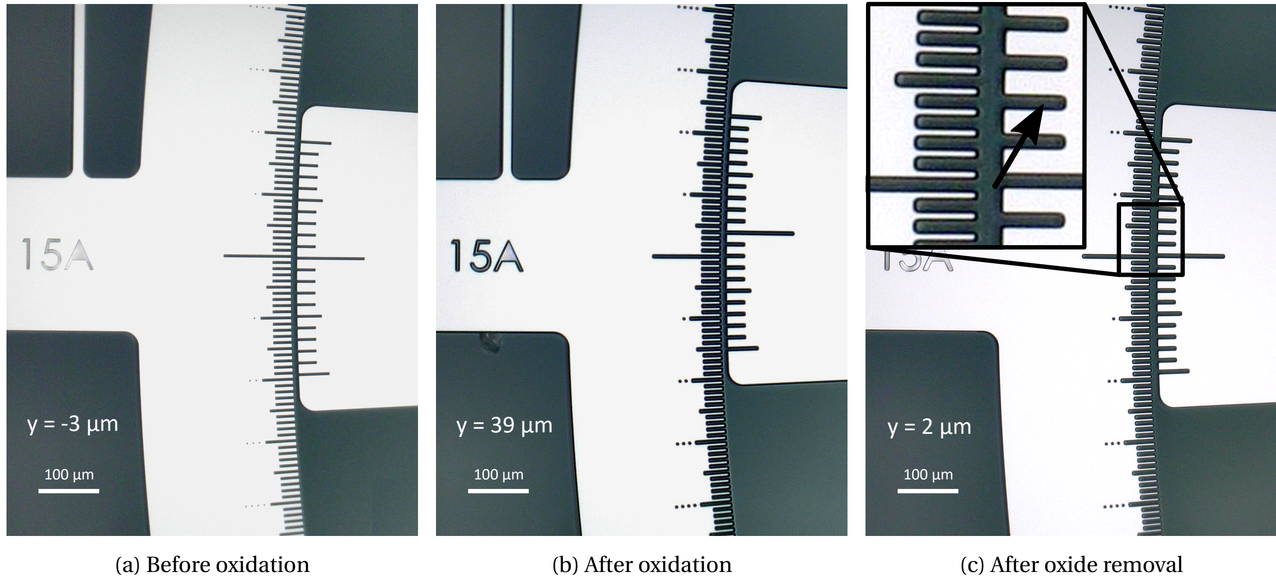

(a) Before oxidation (b) After oxidation (c) After oxide removal

Fig. 7: Example of a measurement read out. A measurement from a 15 µm beam aligned to the <110> direction, 2 µm thick oxide grown at 1100 °C. Fig. 7a shows the initial read out, Fig. 7b shows the read out of the total strain, and Fig. 7c read out after oxide removal. The plastic deformation at the tip is thus 5 µm (0.006 % strain), and the elastic deformation 37 µm(0.048 % strain).

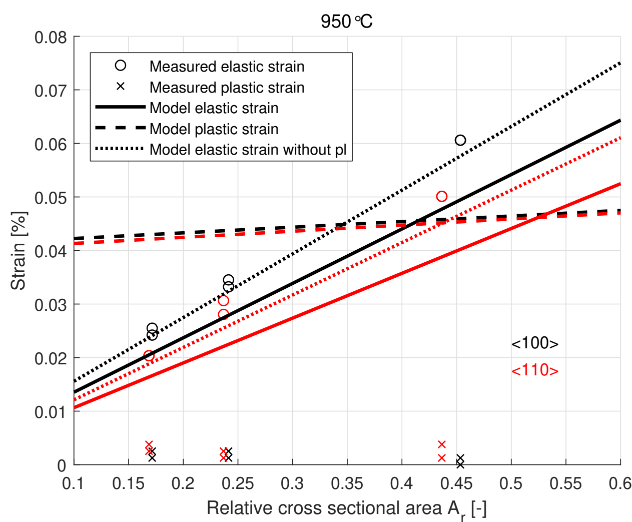

Fig. 9: Experimental and model results for elastic and plastic strain for oxidation at 950 °C.

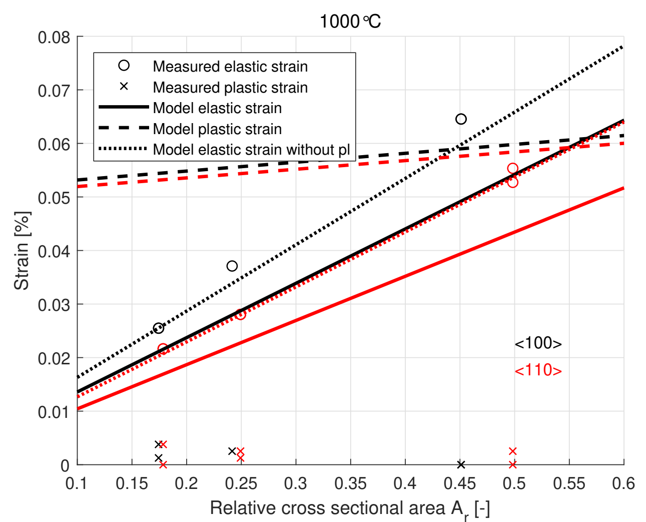

Fig. 10: Experimental and model results for elastic and plastic strain for oxidation at 1000 °C.

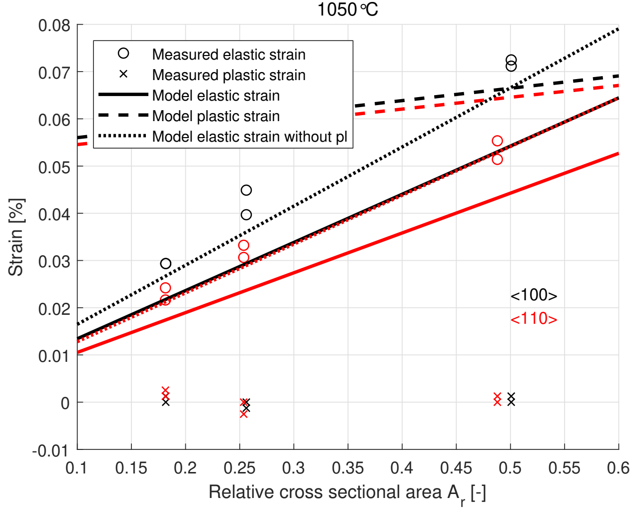

Fig. 11: Experimental and model results for elastic and plastic strain for oxidation at 1050 °C.

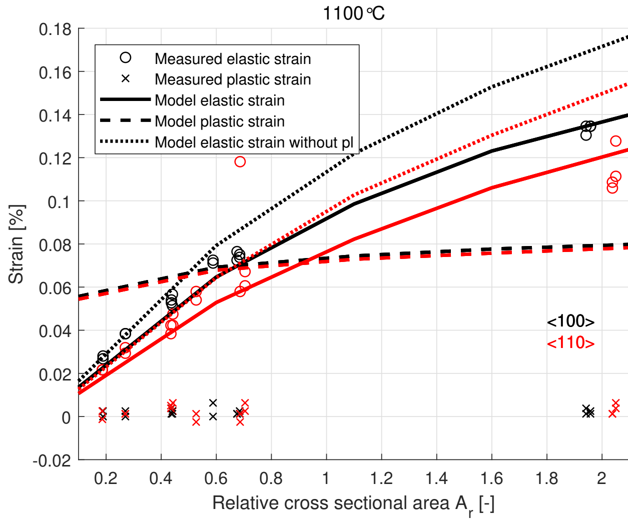

Fig. 12: Experimental and model results for elastic and plastic strain for oxidation at 1100 °C.

4 Discussion

We have successfully measured both elastic and plastic strain in silicon beams as a result of thermal oxidation.

The maximum observed plastic strains was 0.006 %, which is about 10 times less than predicted. We have performed experiments with multiple oxidation temperatures for different beam widths. The oxidation temperature and beam width show no influence on the measured plastic strains. Attempts to induce more plastic strain were made by growing extra thick 2 µm oxide at 1100 °C, and by longer annealing. The observed plastic strains were still in the same range.

In previous experiments by the authors, significant plastic deformation was observed in oxidized silicon micro beams. These samples were etched in bulk FZ silicon wafers, and oxidized using the same process. These type of structures were also fabricated on the same epitaxial silicon wafer as used in this work. No plastic deformation was observed in these samples.

These observations show that epitaxially grown silicon is more resistant than FZ silicon to plastic deformation caused by thermal oxidation, and is therefore a better choice to use when plastic deformations are to be avoided.

The model predictions of plastic strain were inaccurate. It was assumed that the initial dislocation density was in the order of $1 \times 10^{4}\,cm^{-2}$, which is a common value for single crystal silicon in literature [37],[38],[35],[36]. Lower nonzero dislocation densities would still not explain the observed results, as the model is very insensitive for the initial dislocation density because of the large annealing times. This can be seen in Fig. 5. For an extremely low dislocation density of 0.1cm2, the model predicts the same order of plastic strain as for a dislocation density of $1 \times 10^{4}\,cm^{-2}$. For reference, in a 10µm width beam, $0.1\,cm^{-2}$ means a total of 0.5 nm dislocation length. This is equal to the silicon crystal lattice spacing, so this could be seen as the minimum possible nonzero dislocation length.

With the AH plasticity model used in this work, a zero dislocation density would predict zero plastic strain. Sugiura and Yamaguchi [39] have measured zero dislocations in epitaxial grown silicon grown with a special heat treatment. However, it is unlikely that there are zero crystal defects or impurities at all that can function as dislocation sources in any of our samples. It would also not explain the small trend of plastic strain that is observed in the measurements.

The AH model is validated for dislocation densities in the order of $1 \times 10^{4}\,cm^{-2}$ to $1 \times 10^{6}\,cm^{-2}$ [40]. The model may not be valid for extremely low or zero dislocation densities. For instance, the assumptions of uniformly distibuted dislocations may be violated or the assumed multiplication mechanisms may be invalid at extremely low dislocation densities. Future research on plasticity in epitaxial silicon by means of tensile or compression tests could provide insight in the observed results in this work.

Elastic strain measurements are generally in good agreement with the model, where the plasticity of silicon was disabled by simulating with an initial dislocation density of zero. Elastic strain between 0.019 % and 0.135 % are measured. Because plastic strain works stress relieving, the model including plasticity predicts lower elastic strain. At lower oxidation temperatures, the measured elastic strains are significantly larger than predicted. It is likely that at these oxidation temperatures, the stress from volume increase of the oxide is not completely relieved by the viscosity of the oxide. This is in agreement with literature [23], which states that the oxide grows stress-free above 950 °C to 975 °C. The assumption of stress free oxide growth is thus invalid for the oxidations at 900 °C and 950 °C and questionable for 1000 °C. For more accurate predictions at lower oxidation temperatures, this should be included in the model.

We have shown that the lever mechanism was able to distinguish elastic and plastic strain as a result of thermal oxidation. However, the observed plastic strains were smaller than the lever mechanism was designed for. Future research should evaluate the performance for higher plastic strains. This could be achieved by using silicon with more initial dislocations. As previous research by the authors has shown, FZ grown silicon could be used to achieve this. Another option is to use a high level of boron doping in the epitaxial silicon layer. Maseeh and Senturia [4] have observed plastic deformation in heavily Boron-doped oxidized silicon membranes.

For the thinnest 5 µm beams the scale was often deviated out of plane, most likely as a result of gravity. This made it harder to read the scale, because the microscope could not focus on both sides of the scale. At lower magnification, 200x instead of 300x, it was possible to find a focus point where both sides of the scale were still readable. Some of these beams deflected out of plane, and sticked to the sample holder, after vibrations from carrying. These beams sprung back after a small touch, but this could have had an impact on measurements.

5 Conclusion

In this research, we used a lever mechanism to successfully measure both elastic and plastic strain in silicon beams as a result of thermal oxidation. Measurements for different beam widths are performed on samples which were oxidized at temperatures from 900 °C to 1100 °C. We presented a model to predict elastic and plastic strain.

The maximum plastic strain was 0.006 %, which is significantly less than predicted by the model. The oxidation temperature and beam width did not influence plastic strain. The AH model is not accurate for epitaxial silicon with low or zero initial dislocations. As significant plastic deformations were observed in FZ silicon samples from earlier research by the authors, we conclude that epitaxial silicon is a better choice when plastic deformation is to be avoided. Future research is needed on plastic deformation in epitaxial silicon for a more accurate model.

Elastic strain from 0.019 % to 0.135 % was measured, which agrees well with the model for oxidation temperatures from 950 °C to 1100 °C. For oxidation at 900 °C, the model underestimates elastic strain because intrinsic stress originating from volume expansion of silicon dioxide during growth is neglected.

Acknowledgements

The authors would like to thank Else Kooi Laboratory, in particular Jia Wei, for help with fabrication and experiments.

References

[1] Yin Zhang and Ya-pu Zhao. An effective method of determining the residual stress gradients in a micro-cantilever. *Microsystem technologies*, 12(4):357–364, 2006.

[2] Ching-Yu Liu, Frank Yang, Chih-Chiao Teng, and Long-Sheng Fan. A contact-lens-shaped ic chip technology. *Journal of Micromechanics and Microengineering*, 24(4):045025, 2014.

[3] Seungmock Lee, Tsunehisa Tanaka, and Koji Inoue. Residual stress influences on the sensitivity of ultrasonic sensor having composite membrane structure. *Sensors and Actuators A: Physical*, 125(2):242–248, 2006.

[4] Fariborz Maseeh and Stephen D Senturia. Plastic deformation of highly doped silicon. Technical report, Massachusetts Inst of Tech, 1989.

[5] Yu Jie Tang, Jing Chen, Yu Bo Huang, Sha Sha Wang, Zhi Hong Li, Wen Dong Zhang, et al. Ultra-sensitive, highly reproducible film stress characterization using flexible suspended thin silicon plates and local curvature measurements. *Journal of Micromechanics and Microengineering*, 17(10):1923, 2007.

[6] M Finot, IA Blech, S Suresh, and H Fujimoto. Large deformation and geometric instability of substrates with thin-film deposits. *Journal of Applied Physics*, 81(8):3457–3464, 1997.

[7] G Gerald Stoney. The tension of metallic films deposited by electrolysis. *Proceedings of the Royal Society of London Series A*, 82(553):172–175, 1909.

[8] J Laconte, F Iker, S Jorez, N André, J Proost, T Pardoen, D Flandre, and J-P Raskin. Thin films stress extraction using micromachined structures and wafer curvature measurements. *Microelectronic engineering*, 76(1):219–226, 2004.

[9] H Guckel, D Burns, C Rutigliano, E Lovell, and B Choi. Diagnostic microstructures for the measurement of intrinsic strain in thin films. *Journal of Micromechanics and Microengineering*, 2(2):86, 1992.

[10] H Guckel, T Randazzo, and DW Burns. A simple technique for the determination of mechanical strain in thin films with applications to polysilicon. *Journal of Applied Physics*, 57(5):1671–1675, 1985.

[11] Aditya Kumar, Xiaowu Zhang, Qing Xin Zhang, Ming Chinq Jong, Guanbo Huang, Lee Wen Sheng Vincent, Vaidyanathan Kripesh, Charles Lee, John H Lau, Dim Lee Kwong, et al. Residual stress analysis in thin device wafer using piezoresistive stress sensor. *IEEE Transactions on Components, Packaging and Manufacturing Technology*, 1(6):841–851, 2011.

[12] Tommy CP Lo and Philip CH Chan. Design and calibration of a 3-d micro-strain gauge for in situ on chip stress measurements. In *Semiconductor Electronics, 1996. ICSE'96. Proceedings., 1996 IEEE International Conference on*, pages 252–255. IEEE, 1996.

[13] Nathan D Masters, Maarten P de Boer, Brian D Jensen, Michael S Baker, and David Koester. Side-by-side comparison of passive mems strain test structures under residual compression. In *Mechanical Properties of Structural Films*. ASTM International, 2001.

[14] AB Horsfall, JMM dos Santos, SM Soare, NG Wright, AG O'neill, SJ Bull, AJ Walton, AM Gundlach, and JTM Stevenson. Direct measurement of residual stress in sub-micron interconnects. *Semiconductor science and technology*, 18(11):992, 2003.

[15] Fredric Ericson, Staffan Greek, Jan Söderkvist, and Jan-Åke Schweitz. High-sensitivity surface micromachined structures for internal stress and stress gradient evaluation. *Journal of micromechanics and microengineering*, 7(1):30, 1997.

[16] BP Van Drieënhuizen, JFL Goosen, PJ French, and RF Wolffenbuttel. Comparison of techniques for measuring both compressive and tensile stress in thin films. *Sensors and Actuators A: Physical*, 37:756–765, 1993.

[17] Bernd Kämpfe. Investigation of residual stresses in microsystems using x-ray diffraction. *Materials Science and Engineering: A*, 288(2):119–125, 2000.

[18] P Goudeau, N Tamura, B Lavelle, S Rigo, T Masri, A Bosseboeuf, T Sarnet, J-A Petit, and J-M Desmarres. X-ray diffraction characterization of suspended structures for mems applications. 2005.

[19] Joachim Frühauf, Eva Gärtner, and Erhard Jänsch. Silicon as a plastic material. *Journal of Micromechanics and Microengineering*, 9(4):305, 1999.

[20] Jongbaeg Kim, Hyuck Choo, Liwei Lin, and Richard S Muller. Microfabricated torsional actuators using self-aligned plastic deformation of silicon. *Journal of Microelectromechanical Systems*, 15(3):553–562, 2006.

[21] Michael W Judy, Y-H Cho, Roger T Howe, and Albert P Pisano. Self-adjusting microstructures (sams). In *Micro Electro Mechanical Systems, 1991, MEMS'91, Proceedings. An Investigation of Micro Structures, Sensors, Actuators, Machines and Robots. IEEE*, pages 51–56. IEEE, 1991.

[22] Boris Anton Boom, A Bertolini, E Hennes, Robert Anton Brookhuis, Remco J Wiegerink, JFJ Van den Brand, MG Beker, A Oner, and D Van Wees. Nano-g accelerometer using geometric anti-springs. In *Micro Electro Mechanical Systems (MEMS), 2017 IEEE 30th International Conference on*, pages 33–36. IEEE, 2017.

[23] EP EerNisse. Stress in thermal sio2 during growth. *Applied Physics Letters*, 35(1):8–10, 1979.

[24] Alex Masolin, Pierre-Olivier Bouchard, Roberto Martini, and Marc Bernacki. Thermo-mechanical and fracture properties in single-crystal silicon. *Journal of Materials Science*, 48(3):979–988, 2013.

[25] Bruce E Deal and AS Grove. General relationship for the thermal oxidation of silicon. *Journal of Applied Physics*, 36(12):3770–3778, 1965.

[26] Bing Gao, Satoshi Nakano, H Harada, Y Miyamura, and K Kakimoto. Effect of cooling rate on the activation of slip systems in seed cast-grown monocrystalline silicon in the [001] and [111] directions. *Crystal Growth & Design*, 13(6):2661–2669, 2013.

[27] E Orowan. Problems of plastic gliding. *Proceedings of the Physical Society*, 52(1):8, 1940.

[28] Ichiro Yonenaga and K Sumino. Dislocation dynamics in the plastic deformation of silicon crystals ii. experiments. *Physica status solidi (a)*, 51(2):217, 1979.

[29] EA Irene, E Tierney, and J Angilello. A viscous flow model to explain the appearance of high density thermal sio2 at low oxidation temperatures. *Journal of the Electrochemical Society*, 129(11):2594–2597, 1982.

[30] Matthew A Hopcroft, William D Nix, and Thomas W Kenny. What is the young's modulus of silicon? *Journal of microelectromechanical systems*, 19(2):229–238, 2010.

[31] C Bourgeois, E Steinsland, N Blanc, and NF De Rooij. Design of resonators for the determination of the temperature coefficients of elastic constants of monocrystalline silicon. In *Frequency Control Symposium, 1997., Proceedings of the 1997 IEEE International*, pages 791–799. IEEE, 1997.

[32] Akhilesh K Swarnakar, Omer Van der Biest, and Jan Vanhellemont. Determination of the si young's modulus between room and melt temperature using the impulse excitation technique. *physica status solidi (c)*, 11(1):150–155, 2014.

[33] Haruna Tada, Amy E Kumpel, Richard E Lathrop, John B Slanina, Patricia Nieva, Paul Zavracky, Ioannis N Miaoulis, and Peter Y Wong. Thermal expansion coefficient of polycrystalline silicon and silicon dioxide thin films at high temperatures. *Journal of Applied Physics*, 87(9):4189–4193, 2000.

[34] Yasumasa Okada and Yozo Tokumaru. Precise determination of lattice parameter and thermal expansion coefficient of silicon between 300 and 1500 k. *Journal of Applied Physics*, 56(2):314–320, 1984.

[35] Koji Sumino and Ichiro Yonenaga. Difference in the mechanical strengths of dislocation-free crystals of czochralski silicon and float-zone silicon. *Japanese Journal of Applied Physics*, 20(9):L685, 1981.

[36] J Cochard, I Yonenaga, S Gouttebroze, M MâĂŹHamdi, and ZL Zhang. Constitutive modelling of silicon: Parameters identification of classical models using crystal plasticity. 2009.

[37] J Ren, M Ward, Peter Kinnell, and Russell Cradock. Finite element modeling for the mechanical behavior of silicon diaphragms using comsol multiphysics.

[38] H-S Moon, L Anand, and SM Spearing. A constitutive model for the mechanical behavior of single crystal silicon at elevated temperature. *MRS Online Proceedings Library Archive*, 687, 2001.

[39] H Sugiura and M Yamaguchi. Growth of dislocation-free silicon films by molecular beam epitaxy (mbe). *Journal of Vacuum Science and Technology*, 19(2): 157–160, 1981.

[40] Ichiro Yonenaga and K Sumino. Dislocation dynamics in the plastic deformation of silicon crystals i. experiments. *Physica status solidi (a)*, 50(2):685–693, 1978.

Chapter 3

Literature review: A review of methods for measuring residual stress and plastic deformation in MEMS

A review of methods for measuring residual stress and plastic deformation in MEMS

K. V. Sweers, P.R. Kuppens, N. Tolou

December 5, 2018

Abstract

Residual stress in microelectromechanical systems (MEMS) can cause malfunctioning or damage. Residual stress in silicon mechanisms at elevated temperatures can even cause plastic deformations. The objective of this study is to give an overview of current methods for residual stress and plastic strain measurement. No methods were found that measure plastic strain as a result of residual stress. The possibilities to measure plastic strain with the measurement methods found in this study are discussed.

1 Introduction

Residual stress is a common problem with microelectromechanical systems (MEMS). It can cause malfunctioning or change of behavior of micro mechanisms. For example, the geometry of the mechanism can change due to buckling[1], or the stress can change the sensitivity of a MEMS sensor[2]. Residual stress is stress that remains in the material after the original cause for the stress is removed. Causes of residual stress can be classified as chemical, mechanical and thermal[3].

Compliant mechanisms work by using elastic deformation of flexible members, instead of conventional joints. Compliant joints give the possibility of monolithic design, without the need for assembly of components. Because relative motion rigid bodies is absent in compliant mechanisms, there are some great advantages, such as a lack of friction, backlash, and necessary lubrication. These advantages make them perfect for downscaling to the micro scale. Monolithic design eliminates the need for assembly, which would otherwise be hard, slow, and cost ineffective in the micro scale. Downsizing compliant mechanisms gives possibilities for cost reduction, integrated electronics components, and batch production[4].

Micro compliant mechanisms are typically fabricated out of silicon. In a single crystal form, it is an almost perfect Hookean material, meaning that there is almost no hysteresis in the elastic domain[5]. At room temperature, silicon is very brittle. Cracks propagate without any plastic deformation, which means that material failure is characterized by a sudden fracture, without plastic yield. Above a certain temperature, however, silicon starts to behave ductile [6]. Instead of a sudden fracture, plastic yield occurs when the yield stress is exceeded. If the stress is removed, the material will not fully return to its original state, but remains partially deformed.

An example where this can be a cause for problems is thermal oxidation of silicon. Thermal oxidation is often used in the fabrication of MEMS, to create a layer that is electrically insulated or for masking purposes [7, 8]. This process occurs at elevated temperatures, which can get high enough for the silicon to become ductile. When the specimen cools, stresses are introduced due to mismatching thermal expansion coefficiënts. The introduced stresses at elevated temperatures can cause the silicon to yield plastically, leading to a permanent deformation of the mechanism.

Accurate measurement of residual stress and plastic deformation in MEMS is needed to predict and control the effects on micro mechanisms. Literature proposed several methods to measure residual stress, and a few reviews have been published [3, 9]. Some examples of existing techniques to measure residual stress are the wafer curvature method[10], the use of buckling beams in a thin film[11], and mechanisms that use smart geometries to quantify stress[12]. No specific research about measuring plastic deformation in MEMS has been published yet. Investigation is needed how plastic deformation can be measured, and if this could be integrated in stress measurements methods.

The goal of this review is to give an overview of and compare all methods to measure residual stress and plastic deformation in MEMS. The research question is: *What are the current methods for measuring elastic and plastic strain due to residual stress in silicon micro compliant mechanisms?*

The contribution of this paper is an overview on the state of the art of methods to measure residual stress and plastic deformation in micro compliant mechanisms. A categorization presented to compare the found sensing methods. The results are intended to help designers to select the best method for their application.

Section 2 describes the methods for searching, filtering, and classification of the literature. The results are shown in section 3 and discussed in section 4. Conclusions are made in section 5.

2 Method

2.1 Residual stress

Residual stress is stress that remains in the material after the original cause for the stress is removed. Residual stress can influence performance and functionality of MEMS. A few examples are geometry change, a change in sensor sensitivity [2] and change in natural frequency [13]. The origin of residual stress can lay in numerous sources, which Kandil et al. [3] classified as mechanical, thermal and chemical. A few examples of sources that are common in MEMS are:

- **Thermal**
  - Mismatch of thermal expansion coefficients between layers.
- **Chemical**
  - Chemical surface treatments
- **Mechanical**
  - Wafer back-grinding [14].
  - Plastic deformation [15].

2.2 Search method

Scopus is used to search for literature. Different sets of keywords were made for the key subjects concerning the topic. The sets of keywords are then combined in Scopus into a search profile. The sets are shown in table 1. Sets 1,2,3,4,5 and 4,5,7 were used to search for literature concerning residual stress measurement, and sets 1,2,3,4,6 and 4,6,7 for plastic deformation. The search profiles were used to search in titles, abstracts and keywords. The results were filtered based on the title and abstract. The resulting literature was skim read to determine the relevancy. The references were checked, and were filtered with the same procedure.

Table 1: Keywords

nr	Set	Keywords
1	Compliant	Compliant, Flexible, Flexure, Monolithic, Soft
2	Mechanism	Mechanism, Device, Structure, Design, Instrument, Apparatus
3	Measuring	Sens*, Measur*
4	Micro Scale	Nano, Micro, Mini, Small, Silicon, Wafer, MEMS, miniature
5	Residual Stress	Residual stress, Surface Tension, Film stress, Layer stress, Layer tension
6	Plastic deformation	Plastic strain, Plastic deformation, Plastic elongation
7	PCM	Process control monitor, PCM

2.3 Classification

A classification is made to compare the different methods for measuring residual stress. The classification consists of two levels.

2.3.1 Strain amplification

The first level aims to distinguish fundamental differences between general methods for strain amplification. Strain amplification is useful to increase the sensitivity of the sensor. The idea is that the displacement caused by the residual stress is amplified, in order to achieve a smaller step size and thus a higher precision. Strain amplification can be achieved in multiple ways. In this classification, a distinction is made between methods that use bending, geometric amplification, and no strain amplification. Bending principles work if there is a stress gradient in the material. The maximum deflection of a bent specimen can be designed to be much more than the actual maximum strain in the material without amplification. Devices that amplify strain by using a smart geometry, are classified under geometric amplification.

2.3.2 Working principle

The second level contains subcategories, which groups literature that uses the same working princippe. The different working principles in the bending category are wafer curvature, electrostatic deflection, piezo, vibrational, membrane pressure, and buckling. The subgroups of geometric amplification are lever mechanisms, and narrow-bent beams mechanisms. The group with no strain amplification only contains devices that use x-ray diffraction. The working principles will be further discussed in section 3. The classification is shown in table 2.

Table 2: Classification

Strain amplification	Working principle
Bending	Wafer curvature Electrostatic deflection Piezo Vibrational Membrane pressure Buckling
Geometric amplification	Lever mechanisms Narrow-bent beams
-	X-ray diffraction

2.4 Key properties

The performance of the devices and further characterization is evaluated using a set of key properties. These properties help to describe and compare the different devices. If the information is not available, the fields will be left blank, unless it can be approximated from the given information. The key properties are:

- **Bulk/film:** The device uses either the bulk or film to measure stress. This is an important property to asses if it can be used for plastic strain measurements. If the device does not use the bulk to measure stress, it will not be able to measure plastic deformation in the bulk.
- **In/out of plane:** The device amplifies the strain in plane or out of plane. This can be a useful property to investigate if the device can be used for plastic strain measurement.
- **Sensing:** The method of sensing the strain or stress.
- **Size:** The total area consumed by the device.
- **Resolution:** The minimum stepsize of stress that the device can measure.
- **Standard deviation:** The measured stress by the device, and the standard deviation.

3 Results

Only devices found that measure elastic deformation, no devices specify use for measuring plastic deformation as a result of residual stress. The devices are briefly explained in the next paragraphs. An overview of the literature is shown in table 3.

3.1 Bending

3.1.1 Wafer curvature

If there is a residual stress in a thin film on a wafer, the wafer will bend due to this stress. For tensile stresses the wafer will bend the wafer in a convex shape, and compressive stresses will cause a concave shape of the wafer. This is illustrated in figure 1. Wafer curvature stress measurement uses the bending of the wafer as a measure for film stress, and is therefore a bulk mechanism. The bending is always out of plane.

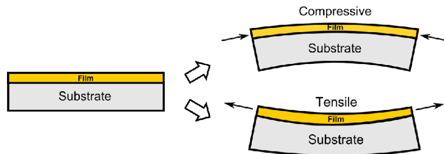

Figure 1: Wafer curvature. Image obtained from [35].

The curvature of a substrate is related to the stress in the thin film by the Stoney equation. This relation requires the substrate to be thick compared to the film, and the film should be in a state of plane stress, meaning that it is in independent from the direction. For isotropic materials, the Stoney equation is: [36, 37]

$$\sigma_f t_f = \frac{E_s h^2}{6(1-\upsilon_s)R} \tag{1}$$

Where σ_f is the in-plane stress in the film, t_f the thickness of the film, E_s the Young's modulus of the substrate, υ_s Poisson's ratio for the substrate, h the thickness of the substrate and R the radius of curvature of the (initial flat) substrate. The Stoney equation for single crystal silicon is slightly different, depending on the orientation of the crystal. For exaple, the Stoney eqauation for single crystal Si(100) wafers is:[37]

$$\sigma_f t_f = \frac{h^2}{6\left(s_{11}^{Si} + s_{12}^{Si}\right)R} \tag{2}$$

Where s_{11}^{Si} and s_{11}^{Si} are values in the compliance tensor.

Laconte et al. [10] used this method to measure the residual stress of nitride and silicon oxide films. A mechanical profilometer was used to measure the curvature of the wafer. In order to measure local curvature more precisely, Tang et al. [16] made a suspended, thinned area in the wafer to measure residual stress in silicon nitride films. A schematic of this test structure is shown in figure 2. With this method, only 1 mm area of the wafer is used, instead of the whole wafer. The thinning of the wafer reduced its stiffness for bending. This gave a larger curvature, and a higher sensitivity. The curvature was measured using optical interferometry, giving it a resolution of 1.5 MPa. A SEM image of the device is shown in figure 3.

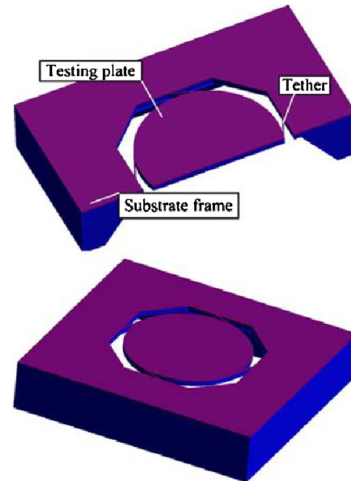

Figure 2: Schematic of thinned local wafer curvature [16]

Table 3: Overview of residual stress measurement methods

Strain amplification	Working principle	Reference	Bulk/Film	In/out of plane measurement	Sensing	Size	Resolution	Standard deviation
Bending	Wafer curvature	[16]	Bulk	Out	Electromagnetic	1mm2	1.5MPa	-
		[10]	Bulk	Out	Mechanical	Whole wafer	-	-
	Electrostatical deflection	[17]	Film	Out	Electromagnetic	0.2mm2	-	5+-0.5MPa
		[18]	Film	Out	Electrical	16mm2		10+-1 Mpa
	Piezo	[14]	Bulk	Out	Electrical	0.16mm2	-	-
		[19]	Bulk	Out	Electrical	-	-	-
	Vibrational	[20]	Film	Out	Electromagnetic	4.5mm2	-	12+-1MPa
		[21]	Film	-	Acoustic	-	-	-
	Membrane pressure	[22]	Film	Out	Optical	0.6mm2	-	1.3+-3.75MPa
		[23]	Film	Out	Electromagnetic	16mm2	-	1000+-10MPa
		[24]	Film	Out	Optical	4mm2	-	30+-0.2MPa
	Buckling	[10]	Film	Out	Electromagnetic	400um2	-	-
		[25]	Film	Out	Optical	24mm2	40MPa	-
		[11]	Film	Out	Electromagnetic	2mm2	-	-
Geometric amplification	Lever mechanisms	[26]	Film	In	Optical	1mm2	5MPa	-
		[27]	Film	In	Electromagnetic	0.1mm2	4MPa	-
		[10]	Film	In	Electromagnetic	0.01mm2	-	-
		[28]	Film	In	Optical	0.1mm2	-	-
		[29]	Film	In	Optical	-	-	-
		[30]	Film	In	Optical	-	3MPa	96+-9MPa
		[12]	Film	In	Optical	1mm2	-	51+-2MPa
		[31]	Film	In	Electromagnetic	0.5mm2	1.4MPa	-
		[32]	Film	In	Optical	3.2mm2	10MPa	-
	Narrow-bent beams	[32]	Film	in	Optical	1.35mm2	3MPa	-
		[33]	Film	In	Optical	0.1mm2	9MPa	18+-5Mpa
-	X-ray diffraction	[15]	Bulk	-	Electromagnetic	very small	-	-
		[34]	bulk	-	Electromagnetic	very small	-	-

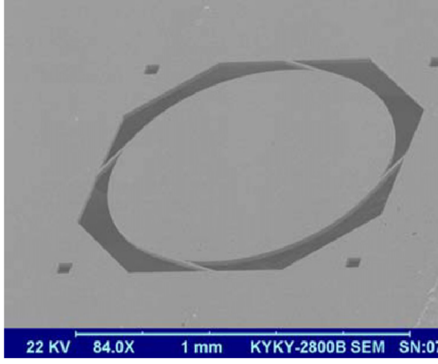

Figure 3: SEM image of thinned local wafer curvature [16]

3.1.2 Electrostatic deflection

Baker et al. [17] use electrostatic deflection to measure residual stress in a polysilicon film. A clamped=clamped beam is made out of the film, and the deflection is measured under an electrostatic force using interferometry. The residual stress is obtained from a best fit between a FEM model and the measured data. The schematic is shown in figure 4a, and an example of a measured interferogram of the deflection is shown in figure 4b. The area consumed by the device is 0.2 mm^2. The mechanism uses the film to obtain the residual stress, and out of plane deflection is measured. Stress values of 5 ± 0.5MPa.

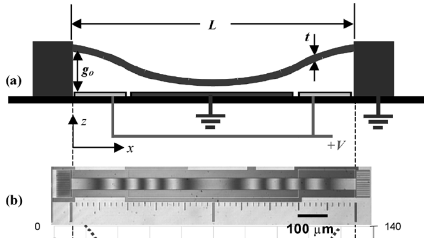

Figure 4: Electrostatic deflection. a) schematic, b) interferogram of the deflection. [17]

Osterberg and Senturia [18] measure the necessary voltage to imply pull-in of a clamped-clamped silicon beam. The beams are fabricated by wafer bonding, and thinning to 14µm afterwards. The voltage is slowly increased, and at a certain point, the clamped-clamped beams will buckle and the pull-in is detected by an increased electrical current. This pull-in point is a sharp instability in the behavior of elastic beams subjected to a parallel-plate electrostatic force, and is therefore a well-suited measurement point. The pull-in voltage is used to calculate the residual stress. The test is done for beams of multiple lengths, and the results are fitted to a 2D distributed model to obtain the residual stress. The total area consumed by the structures is 16 mm.

3.1.3 Piezo sensors

Piezoresistive sensors change electrical resistivity due to an applied strain. So these can be used to measure residual stresses. These devices use the bending of the wafer, so they are considered bulk sensors, working out of plane. Lo and Chan [19] and used piezoresistive stress sensors to measure the electrical resistance to quantify the bending of the wafer, and thus the residual stress. The relation between electrical resistance and stress is evaluated by calibrating the sensor with a known stress. A four-point bending fixture was used to calibrate the sensors, which is shown in figure 6. Kumar et al. [14] used a similar method to measure residual stress due to wafer back grinding. During calibration, the applied stress is known, and the piezoresistive coëfficients π_{11}, π_{12} and π_{44} are determined. The test chip is shown in figure 5, and the sensors consume 0.16 mm^2 on the wafer. The residual stress is now evaluated with the following formulas:

$$\sigma_x = \frac{\pi_{44}\left(\frac{\Delta R_1}{R_{10}} + \frac{\Delta R_3}{R_{30}}\right) + (\pi_{11} + \pi_{12})\left(\frac{\Delta R_1}{R_{10}} - \frac{\Delta R_3}{R_{10}}\right)}{2\pi_{44}(\pi_{11} + \pi_{12})} \tag{3}$$

$$\sigma_y = \frac{\pi_{44}\left(\frac{\Delta R_1}{R_{10}} + \frac{\Delta R_3}{R_{30}}\right) - (\pi_{11} + \pi_{12})\left(\frac{\Delta R_1}{R_{10}} - \frac{\Delta R_3}{R_{10}}\right)}{2\pi_{44}(\pi_{11} + \pi_{12})} \tag{4}$$

Where σ_x and σ_y are the stresses in x and y direction, ΔR_i and R_{i0} are the change in electric resistance and the initial resistance of the ith sensor. A compressive residual stress was found due to the backgrinding, and it increased exponentially with the decrease in wafer thickness.

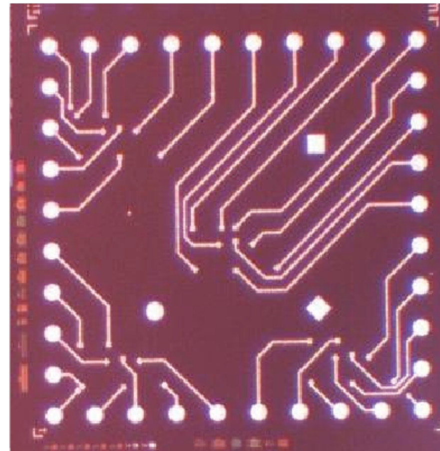

Figure 5: Optical image of piezoresistive stress sensor showing the metallization lines with probing pads [14]

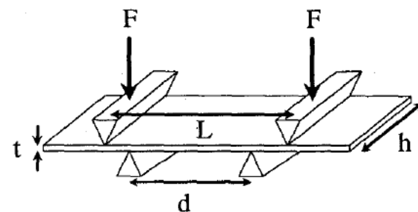

Figure 6: Schematic of a four-point bending fixture [19]

3.1.4 Vibrational

Kim and Allen [21] use the first eigenfrequency of string structures in the film to determine residual stress. The velocity of wave propagation in a string v depends on the tension in the string T and the linear density μ (mass per unit length), and is also proportional to the product of the wavelength λ and frequency f:

$$v = \sqrt{\frac{T}{\mu}} = \lambda f \tag{5}$$

The fundamental frequency of the string has nodes on both ends of the string, and consists of half a wavelength. The wavelength can be expressed in terms of length L of the string:

$$\lambda = 2L \tag{6}$$

Combining equations 5 and 6 gives:

$$f = \frac{\sqrt{\frac{T}{\mu}}}{2L} \tag{7}$$

The string tension and linear density can be expressed in terms of stress, cross sectional area and density:

$$T = \sigma A \qquad \mu = A\rho \tag{8}$$

where σ is the stress in the string, A the cross sectional area of the string, and ρ the density of the string. Combining equations 7 and 8 gives the relation between the stress in the string and the first eigenfrequency:

$$\sigma = 4L^2 f^2 \rho \tag{9}$$

The strings used by Kim and Allen [21] are actuated by acoustic waves from a speaker. The sound waves are sensed by a high-sensitivity microphone on the other side of the strings. If the acoustic waves have the same frequency as the eigenfrequency of the strings, energy transfer from the sound waves into the strings occur, inducing string vibration. Due to this energy transfer, a lower signal is sensed by the microphone. This way, the eigenfrequency of the strings is determined. A schematic of the test setup is shown in figure 7, and an image of the strings is shown in figure 8. Note that only tensile film stresses can be measured.

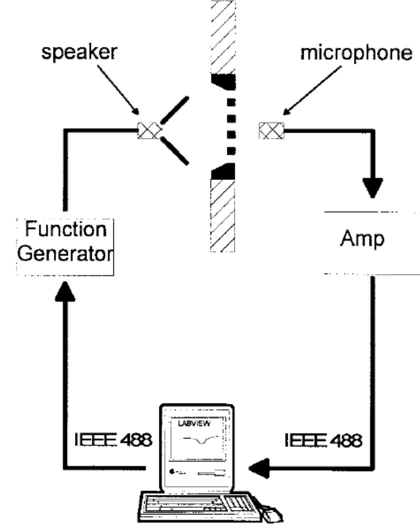

Figure 7: Schematic of acoustic string vibrations setup [21]

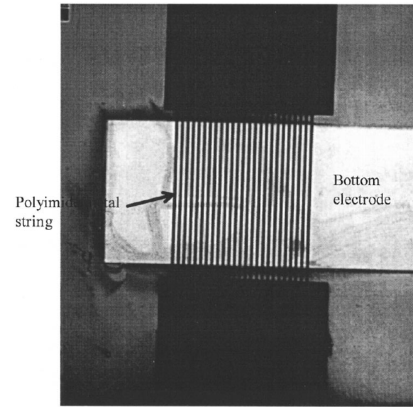

Figure 8: Optical image of strings [21]

Ikehara et al. [20] use the eigenfrequency of clamped-clamped polysilicon beams to evaluate compressive residual stresses. Beams of different lengths are used, in order to obtain a length dependence curve of the resonant frequency. The chip is actuated by a PZT (Lead Zirconate Titanate) plate, and the frequencies are sensed by a laser-Doppler vibrometer and a spectrum analyzer. Finite-element calculations are fitted tot the measured data to obtain the residual stress. The approximate relation between strain and eigenfrequency for these type of beams is given by: [38]

$$f = 1.028 \left[\frac{E}{rho}\right]^{\frac{1}{2}} \frac{h}{l^2} \left[1 + 0.295 \left(\frac{l}{h}\right)^2 \varepsilon\right]^{\frac{1}{2}} \tag{10}$$

It is found that the post-buckling frequency is more sensitive to compressive residual strain than before buckling. A residual stress of 12 ± 1MPa is found in the film. A schematic is shown in figure 9. The total area of the sensor is $4.5\,\text{mm}^2$.

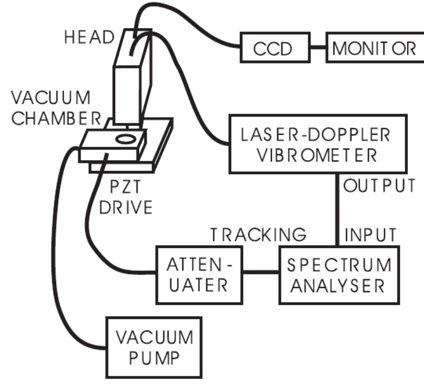

Figure 9: Schematic of test setup by Ikehara et al. [20]

3.1.5 Membrane pressure

Tabata et al. [23] measured deflection of thin polysilicon and silicon nitride membranes, when applying an pressure. The maximum out of plane deflection is influenced by the stress in the film. The analytical relation between the residual stress σ and membrane deflection h for a rectangular membranes with side lengths a and b derived by is:

$$\sigma = \frac{a^2}{C_1 th}\left(p - \frac{C_2 Eth^3}{a^4}\right) \tag{11}$$

Where t is the membrane thickness, p the pressure, and E the Young's modulus. C_1 and C_2 are constants determined by the membrane shape b/a and Poisson's ratio v. Interferometry was used to determine the deflection profile of the film. The area of the device was $16\,\text{mm}^2$, and a residual stress of 1000 ± 10MPa was measured.

Ziebart et al. [22] used a similar setup for the measurement of residual stress of silicon nitride films, but measured the out of plane deflection with an optical profilometer. A schematic is shown in figure 10. The sensor area is $0.6\,\text{mm}^2$, and a residual stress of 1.3 ± 3.75MPa is measured.

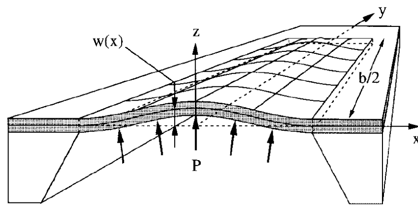

Figure 10: Schematic of membrane pressure [22]

Allen et al. [24] used the membrane pressure method to measure residual stress of a polyimide film. The deflection was measured using a calibrated microscope. The sensor area was $4\,\text{mm}^2$, and a stress of 30 ± 0.2MPa was measured in the batch with the least deviation.

3.1.6 Buckling

Buckling of a beam only happens if the compressive stress on a beam reaches a certain limit. Below the limit, the beam will compress purely axially. Above the limit, the beam will bend. This is a sharp instability, and therefore useful to determine the residual stress in the material. Buckling is out of plane in these structures, and acts in the film. The critical load P_{cr} for a beam to buckle is described by: [39]

$$P_{cr} = -\frac{\pi^2 EI}{K^2 L^2} \tag{12}$$

Where E is the Young's modulus, I the area moment of inertia of the cross section of the beam, K the effective length factor, depending on the end conditions, and L the length of the beam. For beams with a rectangular cross section and fixed-fixed end conditions, $I = \frac{bh^3}{12}$ and $K = 0.5$. The relation between the geometry of the beam and the critical strain ε_{cr} can now be derived as:

$$\varepsilon_{cr} = -\frac{\pi^2 h^2}{3L^2} \tag{13}$$

Buckling can only occus under a compressive stress. Tensile stresses can be inverted to compressive stresses to use the buckling principle. A commonly used method is the ring-and-beam structure, which is used by Guckel et al. [25] and shown in figure 11a. If points A in the ring in figure 11c are moved in direction Q due to a compressive stress, point B will move towards the center of the circle. If a beam is present between points B, a compressive stress will occur. The buckling of this beam can be used to determine the residual stress.

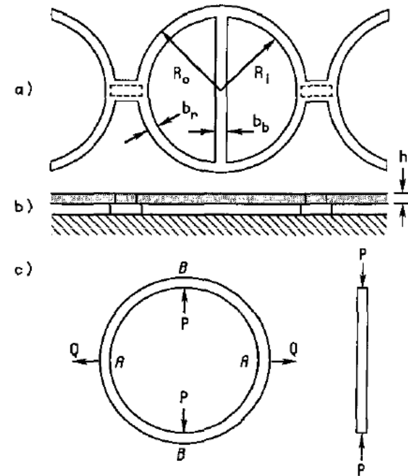

Figure 11: Schematic of ring-and-beam structure [25]

Guckel et al. [25] used clamped-clamped polysilicon beams of multiple lengths, and evaluates at which length buckling occurs. This critical length is used to calculate the residual stress. They used optical microscopy to see if buckling occurs. The area of the beams was $24\,\text{mm}^2$. The resolution is directly related to the step size in length difference of the beams, and translates to 40 MPa.

Guckel et al. [11] used a similar method, but used interference contrast microscopy to sense the buckling in

polysilicon beams. The used area was 2 mm². An image of a buckled beam in shown in figure 12.

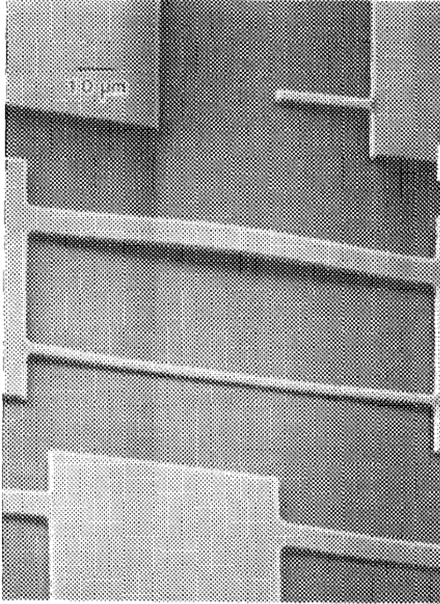

Figure 12: A buckled beam due to residual stress [11]

Laconte et al. [10] used clamped-clamped beams made of silicon oxide and ring-and-beam structures out of nitride films to measure the compressive and tensile stresses. Not the critical length of the beams, but the amount of buckling is measured to evaluate the stress. Interferometry is used to measure the deflection in the post-buckling state. A SEM image from the ring-and-beam structure is shown in figure 14, and an interferogram is shown in figure 13. The residual strain ε_R is given by:[32]

$$\varepsilon_R = \frac{\pi^2}{L^2}\left(\frac{A^2}{4} + \frac{t^2}{3}\right) \quad (14)$$

Where L is the beam length, A the buckling amplitude and t the beam thickness. The beams used 400µm² on the wafer.

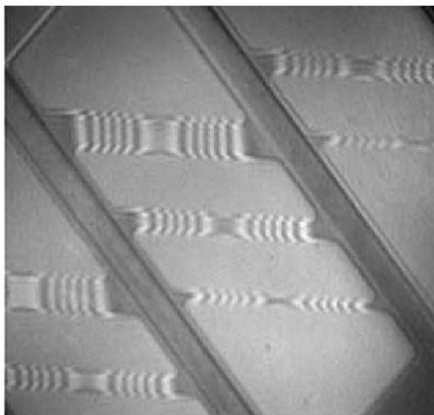

Figure 13: Interferogram of buckling beam [10]

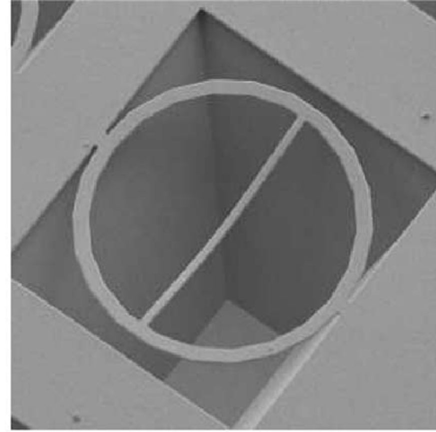

Figure 14: Ring-and-beam buckling structure [10]

3.2 Geometric amplification

This section described sensors that use a smart geometry to amplify the strain. All devices in this section are able to sense both tensile and compressive stresses. The mechanisms in this section all move in-plane, and are constructed in the thin film. These mechanisms are compliant, which means that they use flexible members instead of rigid bodies. These compliant mechanisms have a geometry that increases the strain.

3.2.1 Lever mechanisms

Lever mechanisms are often used to amplify strain. An example is the device made by Masters et al. [32], which is shown schematically in figure 15. It was used to evaluate residual stress in a polysilicon film. When the structure is released from the sacrificial layer, only the anchor points are connected to the substrate. These are indicated by gray areas. As the structure is released, the arms indicated with L_A and L_B will contract or extend to relieve any residual stress. The pointer beam will rotate, because the connections between the arms and pointer beam are off-centered with a spacing O. The residual strain is be modeled analytically. The residual strain ε_R is given by:

$$\varepsilon_R = \frac{O_Y}{(L_A + L_B)(L_C + O/2)}\frac{1}{C_F} \quad (15)$$

Where L_A,L_B,L_C,O_Y and O are defined in figure 15. The first part of the equation assumes an ideal relationship between residual strain and the displacement of the tip. The second part, $(\frac{1}{C_F})$, is a correction factor that accounts for non-idealities. This factor is derives from finite element models. This device used 3.2 mm² on the wafer, and had a resolution of 10MPa. An optical microscope was used to read the deflection of the pointer.

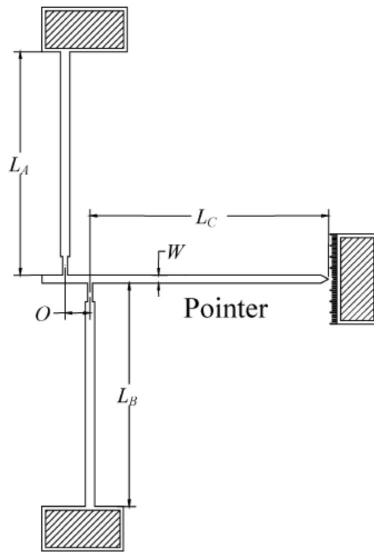

Figure 15: Schemetaic of rotating beam mechanism [32]

Very similar geometries were used by Kasbari et al. [27],Horsfall et al. [28], and Zhang et al. [12].

Kasbari et al. [27] measures the residual stress in copper films. The deflection is read using a SEM. The area of the structure was 0.1 mm^2. A resolution of 4 MPa was obtained.

Horsfall et al. [28] uses the lever mechanism to measure residual stress in aluminum films. An optical microscope was used to evaluate the angle of the pointer beam. The area of the mechanism was 0.1 mm^2.

Zhang et al. [12] measured residual stress in polysilicon and silicon nitride films. An optical microscope was used to read the deflection, and a stress of 51 ± 2MPa was measured. The mechanism consumed an area of 1 mm^2. A photograph of the device is shown in figure 16.

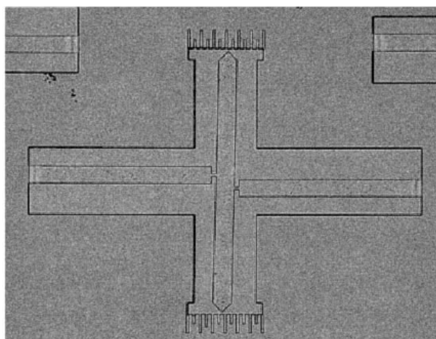

Figure 16: Lever mechanism by Zhang et al. [12]

Ericson et al. [31] used a similar mechanism, but in a duplicated form to achieve two opposite deflections. This increases the sensitivity. The device is shown in figure 17. The deflection is measured with an optical microscope, which achieved a resolution of 5 MPa for an aluminum film. The sensor consumed 1 mm.

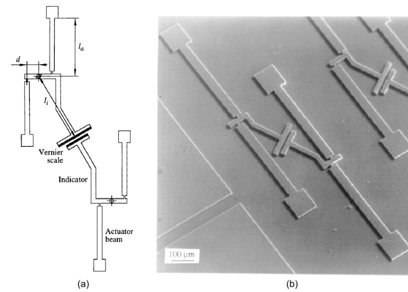

Figure 17: (a) A schematic of the mechanism by Ericson et al. [31] and (b) a SEM image of the device.

Laconte et al. [10] and Lin et al. [30] used a slightly different geometry, with only one arm. A schematic of the device from Laconte et al. [10] is shown in figure 18. The tip deflection is measured with an SEM, with the use of a scale. Both silicon oxide and nitride films were used. The area of the device was 0.01 mm^2.

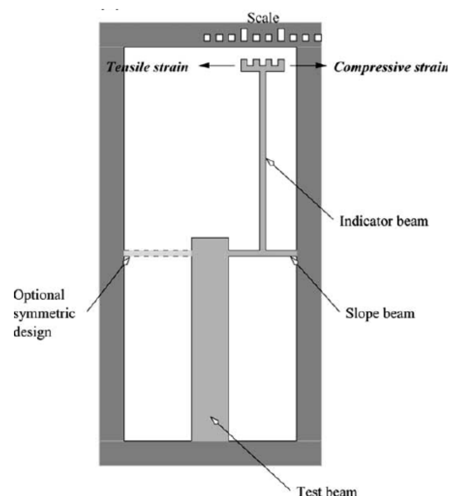

Figure 18: Lever mechanism with vernier scale [10]

A SEM image of the device by [30] is shown in figure 19. It was used to evaluate residual stress in polysilicon and silicon nitride films. An optical microscope was used to read the displacement of the tip, with the help of a vernier gauge. An example of a measurement is shown in figure 20. The resolution was 3 MPa, and 96 ± 9MPa was achieved.

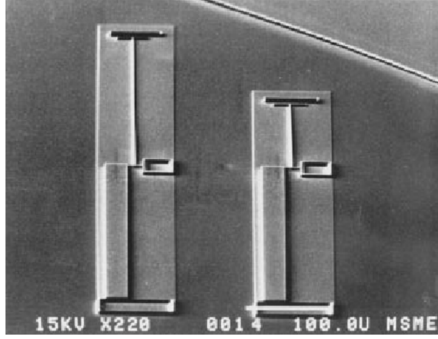

Figure 19: Lever mechanism by Lin et al. [30]

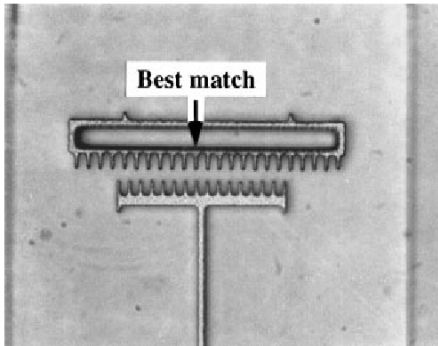

Figure 20: An example of a measurement under an optical microscope [30]

Arrazat et al. [26] used a "H" geometry, as shown in figure 21. It could be described by a mirrored lever mechanism, where the pointer beams are connected. A residual stress will force the connected pointer beam to bend. The device is used to measure the stress in aluminum films. A finite element model is used to calculate the residual stress from the maximum displacement in the center of the pointer beam. The displacement is obtained optically. The minimum stepsize in measurement translates to a stepsize of 5 MPa in residual stress. The device used 1 mm^2.

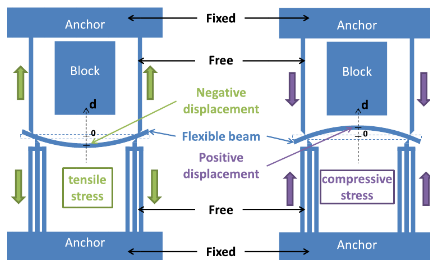

Figure 21: Schematic of "H" sensor with a flexible beam [26]

Pan and Hsu [29] use a structure of parallel beams with different lengths. The elongation of a beam is proportional to the length of the beam, when it is free to relieve any residual stress. The beams in the structure have different lengths, so the elongation will also be different. The beams are connected at the end by a rigid block, so as a result of the residual stress, the beams will bend. The structure is shown in figure 22. The structure was used to measure residual stress in silicon dioxide and polysilicon films. The residual stress is obtained by using the deflection of the beams in a analytical and FEM model.

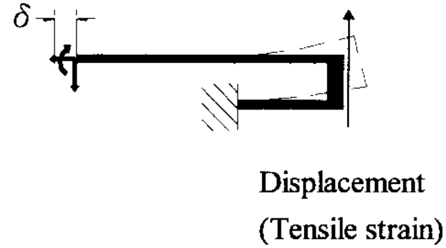

Figure 22: Schematic of deflecting beams with different length by Pan and Hsu [29]

3.2.2 Narrow-bent beams

Masters et al. [32] use narrow-bent beams to amplify the strain in polysilicon films. The mechanism is shown in figure 23. The strain in the beams is amplified by the small angle between the beams. Because of this angle, the distance between the centers of the beams will change due to the residual stress. A scale is used for precise measurements with an optical microscope. The area of the device was 1.35 mm^2.

$$\varepsilon_R = \delta \frac{\left[\frac{2b_{BB}tL_{BB}^3\sin\phi}{\cos^4\phi} + \frac{12I_{yy}L_{BB}}{\sin\phi} + \frac{6I_{yy}L_{Ind}}{\sin\phi\cos\phi}\right]}{\left[(2L_{BB}+L_{Ind})\left(\frac{wtL_{BB}^3}{\cos^3\phi} - \frac{12I_{YY}L_{BB}}{\cos\phi}\right)\right]} \tag{16}$$

Where δ is the measured displacement, t the thickness of the beams, $I_{yy} = \frac{tb_{BB}^3}{6}$ is the in-plane area moment of inertia of the beams. A resolution of 3 MPa was obtained.

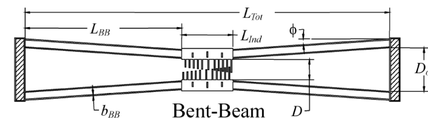

Figure 23: Schematic of narrow-bent beams by Masters et al. [32]

Gianchandani and Najafi [33] used the same type of device to measure residual stress in polysilicon films. The structure used 0.1 mm^2. A residual stress of 18± 5MPa was measured. The strain was read with optical microscopy, with the help of a vernier scale. This is shown in figure 24.

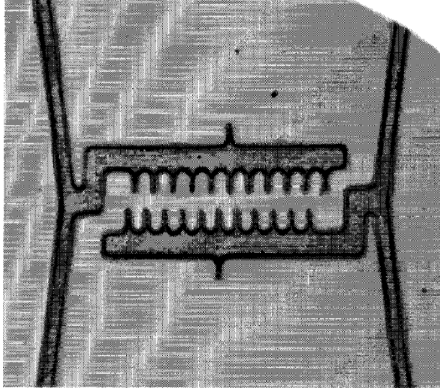

Figure 24: Vernier scale by Gianchandani and Najafi [33]

3.3 No strain amplification

3.3.1 X-ray diffraction

Kämpfe [15] proposed a method to use x-ray diffraction to measure stress in micro systems The lattice spacing is determined by the diffraction of x-ray beams, which is shown schematically in figure 25. Goudeau et al. [34] used x-ray diffraction to measure residual stress in gold thin films, which were deposited on polysilicon beams. The curvature of the beams was also measured, and used to calculate residual stress in the film as a comparison to the x-ray method. A SEM image of the beams is shown in figure 26. The stress measured with x-ray diffraction was similar to the stress measured using the curvature of the beams. This type of devices use the bulk to measure residual stress. No deflection in or out of plane is necessary for these measurements.

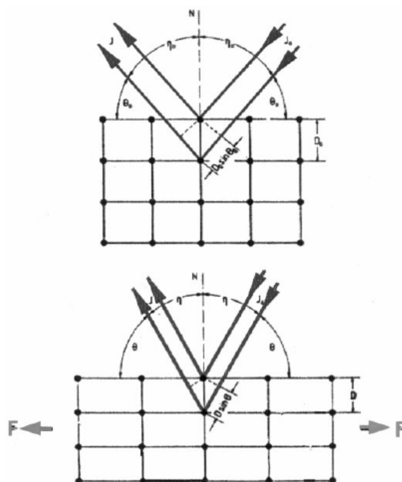

Figure 25: X-ray diffraction working principle [15]

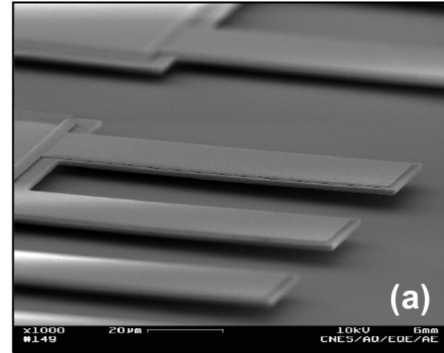

Figure 26: SEM image of gold films on polysilicon beams, used by Goudeau et al. [34]

4 Discussion

In this section, the results are compared to each other and discussed. Several methods to measure residual stress in MEMS were found, but no literature was found that presented a method to quantify resulting plastic deformation. First, the methods for residual stress measurements are compared, using the performance criteria. After that, it will be discusses which methods could theoretically be used to measure plastic strain.

4.1 Bulk/film

Most devices use the film to measure the stress. Only wafer curvature, piezo, and x-ray diffraction use the bulk. The importance of this property is mostly related to the suitability for measuring plastic strain, and will be discussed later.

4.2 In/out of plane

Bending mechanisms always use out of plane measurement, and geometric amplification always use in plane measurements. For wafer curvature and piezo, the film is deposited on one side of the wafer, giving an out of plane bending. Other bending methods impose bending of the film only, without the substrate. Out of plane bending is the most convenient, due to the small film thickness compared to width of the structures. Geometric amplification mechanisms have found to be always in-plane. It is the easiest method to design structures in-plane, since the structures then can be 2D. Out of plane structures would require more lithography steps, and is therefore more complex and expensive.

It is interesting that the devices that use in-plane measurements, always use the film to measure. In theory, in plane measurements could also be taken with the bulk, if the film is deposited symmetrically on both sides of the substrate. However, it is less convenient, because stress in the bulk is much lower due to the thickness difference between film and substrate.

4.3 Sensing methods

The general method for sensing the strain in geometric amplification methods is to produce an image of the device, and use this image to measure a deflection. The images are either taken with an optical or scanning electron microscope. A vernier scale is sometimes used to achieve a better resolution. Methods that use out of plane deflections are sensed by interferometry, or by mechanical touch. Piezo and electrostatical deflection use electrical signals as a quantification of stress. The resolutions are typically in the order of megapascals for all methods where a resolution was given. It is difficult to compare the different methods based on resolution. A resolution was given for only 9 of the 27 devices. Also, they are not necessarily designed to measure in the same stress range, which can influence the resolutions.

4.4 Size

Small size of a stress measurement device gives the possibility to add multiple devices on a wafer. With more data, a higher accuracy can be achieved. With multiple devices, it is also possible to measure stress gradients across the wafer. If the devices are small enough, they can be incorporated as process control monitors on a wafer, with no or minimal extra cost. The size of the found devices differs a lot. In general, the methods using geometric amplification (lever mechanisms and narrow-bent beams) use between $0.01\,mm^2$ and $3\,mm^2$. Bending methods use often a bit more space, between $0.004\,mm^2$ and $24\,mm^2$. The normal wafer curvature even requires the whole wafer, so this should be avoided when size is important. When small size is desired, one of the remaining methods can be used.

4.5 Resolution

Unfortunately, the resolution and standard deviations of residual stress measurements were often not given. The given resolutions do not indicate a clear performance difference for the methods. Most resolutions are in the order of 1.5 MPa to 10 MPa. The resolution is usually limited by the sensing equipment. For example, the resolution of Ericson et al. [31] with a SEM was 1.4 MPa, where the best result with an optical microscope was 3 MPa [30].

4.6 Standard deviation

The standard deviation was often not given. The given values are hard to compare, since different materials are measured with different processes. Therefore the residual stresses differ greatly, and the standard deviation too. The extreme differences are best seen in the membrane pressure category, where the measured stresses vary from 1.3 MPa to 1000 MPa, with corresponding standard deviations of 3.75 MPa and 10 MPa.

It can be concluded that there are no clear best or worst methods to measure residual stress. The choice for which method to use should be based on the available production processes and the available sensing equipment.

4.7 Use for plastic strain

No literature has been found where a distinction between plastic and elastic strain has been made. In theory, plastic strain could be measured by first determining the stress and strain, and then measure the strain after the cause for stress is removed. So it is important to know what causes the residual stress. We will discuss here which methods can be used for cases where the residuals stress is caused by a thin film. If the film is removed, the original cause for the residual stress is removed and the plastic strain can be measured. To measure plastic strain in the silicon, only devices can be used that use the bulk material to measure stress. Device that only use the film, will not be able to sense plastic strain in the bulk, since the film is the cause for the residual stress and has to be removed, and can therefore not measure the plastic strain. An example is a buckling beam, which is fabricated in the thin film that is the origin of residual stress. When the film is removed, there is no beam left that can quantify the plastic deformation.

Wafer curvature, piezo, and x-ray diffraction are the only devices in literature that measure strain in the bulk. So in theory, they could also be used to measure plastic deformation as a result of residual stress. However, x-ray diffraction just measures the spacing of the crystal lattice. This means that it cannot measure plastic deformation, where the lattice is shifted. Measuring plastic deformation with wafer curvature would be convenient, since the method is simple and the equipment is usually accessible. A disadvantage of using the wafer curvature method is that the whole wafer is used, so no local measurements can be performed, and it cannot be incorporated as a process control monitor on the same wafer. Another disadvantage is that the wafer is typically very thick compared to the film. Therefore the stress in the silicon will be small, and plastic deformation will be limited or nonexistent. Piezo sensors have the advantage over wafer curvature of being small. However, it could be a disadvantage that extra process steps are needed to create a piezo sensor. Also, it might be difficult to determine where the piezo material must be placed, as the silicon oxide is grown on the silicon.

Other methods that use the film for measurement could potentially be modified, such that they also use the bulk. Then, they may also be able to measure plastic deformation. One could think of the methods that use buckling or geometric amplification. If the strain amplifying mechanisms are fabricated as a composite of bulk and film, they could theoretically be used to measure both elastic and plastic strain. The sum of the elastic and plastic

strain would be obtained by a measurement of the composite structure. The plastic strain is isolated if the film is removed in a next step. The source of stress is then removed, so only the plastic deformations will remain. It would be a promising research direction to design a sensor for plastic strain, that is convenient and cost efficient to use.

5 Conclusions

An overview and classification of existing residual stress measurement methods has been presented. These results could be used as a tool to select the most appropriate method for a certain application. The different measurement methods are compared to each other. Performance did not differ greatly between different methods, so the most suitable method should be chosen based on available production processes, sensing equipment and space requirements.

It has been discusses that of the residual stress measurement methods, wafer curvature and piezo sensors could be used to measure plastic strain. Theoretically, other modified methods could also be used. If methods which rely on the thin film for the measurements could be modified to work as a composite of bulk and film, they could potentially be used to distinguish elastic and plastic strain. A promising direction for future research would be to design plastic strain sensor based on these concepts.

References

[1] BP Van Drieënhuizen, JFL Goosen, PJ French, and RF Wolffenbuttel. Comparison of techniques for measuring both compressive and tensile stress in thin films. *Sensors and Actuators A: Physical*, 37:756–765, 1993.

[2] Seungmock Lee, Tsunehisa Tanaka, and Koji Inoue. Residual stress influences on the sensitivity of ultrasonic sensor having composite membrane structure. *Sensors and Actuators A: Physical*, 125(2):242–248, 2006.

[3] FA Kandil, JD Lord, AT Fry, and PV Grant. A review of residual stress measurement methods. *A Guide to Technique Selection, NPL, Report MATC (A)*, 4, 2001.

[4] Mohammad I Younis. *MEMS linear and nonlinear statics and dynamics*, volume 20. Springer Science & Business Media, 2011.

[5] Sunipa Roy and Chandan Kumar Sarkar. *MEMS and Nanotechnology for Gas Sensors*. CRC Press, 2017.

[6] Alex Masolin, Pierre-Olivier Bouchard, Roberto Martini, and Marc Bernacki. Thermo-mechanical and fracture properties in single-crystal silicon. *Journal of Materials Science*, 48(3):979–988, 2013.

[7] Fabricating mems and nanotechnology, . URL `https://www.mems-exchange.org/MEMS/fabrication.html`.

[8] Mems thin film deposition processes, . URL `https://www.memsnet.org/mems/processes/deposition.html`.

[9] VT Srikar and SM Spearing. A critical review of microscale mechanical testing methods used in the design of microelectromechanical systems. *Experimental mechanics*, 43(3):238–247, 2003.

[10] J Laconte, F Iker, S Jorez, N André, J Proost, T Pardoen, D Flandre, and J-P Raskin. Thin films stress extraction using micromachined structures and wafer curvature measurements. *Microelectronic engineering*, 76(1):219–226, 2004.

[11] H Guckel, T Randazzo, and DW Burns. A simple technique for the determination of mechanical strain in thin films with applications to polysilicon. *Journal of Applied Physics*, 57(5):1671–1675, 1985.

[12] Xin Zhang, Tong-Yi Zhang, and Yitshak Zohar. Measurements of residual stresses in thin films using micro-rotating-structures. *Thin Solid Films*, 335(1):97–105, 1998.

[13] C.C. Lee, GZ Cao, and IY Shen. Effects of residual stresses on lead–zirconate–titanate (pzt) thin-film membrane microactuators. *Sensors and Actuators A: Physical*, 159(1):88–95, 2010.

[14] Aditya Kumar, Xiaowu Zhang, Qing Xin Zhang, Ming Chinq Jong, Guanbo Huang, Lee Wen Sheng Vincent, Vaidyanathan Kripesh, Charles Lee, John H Lau, Dim Lee Kwong, et al. Residual stress analysis in thin device wafer using piezoresistive stress sensor. *IEEE Transactions on Components, Packaging and Manufacturing Technology*, 1(6):841–851, 2011.

[15] Bernd Kämpfe. Investigation of residual stresses in microsystems using x-ray diffraction. *Materials Science and Engineering: A*, 288(2):119–125, 2000.

[16] Yu Jie Tang, Jing Chen, Yu Bo Huang, Sha Sha Wang, Zhi Hong Li, Wen Dong Zhang, et al. Ultra-sensitive, highly reproducible film stress characterization using flexible suspended thin silicon plates and local curvature measurements. *Journal of Micromechanics and Microengineering*, 17(10):1923, 2007.

[17] Michael S Baker, Maarten P de Boer, Norman F Smith, Larry K Warne, and Michael B Sinclair. Integrated measurement-modeling approaches for evaluating residual stress using micromachined fixed-fixed beams. *Journal of microelectromechanical systems*, 11(6):743–753, 2002.

[18] Peter M Osterberg and Stephen D Senturia. M-test: a test chip for mems material property measurement

using electrostatically actuated test structures. *Journal of Microelectromechanical systems*, 6(2):107–118, 1997.

[19] Tommy CP Lo and Philip CH Chan. Design and calibration of a 3-d micro-strain gauge for in situ on chip stress measurements. In *Semiconductor Electronics, 1996. ICSE'96. Proceedings., 1996 IEEE International Conference on*, pages 252–255. IEEE, 1996.

[20] T Ikehara, RAF Zwijze, and K Ikeda. New method for an accurate determination of residual strain in polycrystalline silicon films by analysing resonant frequencies of micromachined beams. *Journal of Micromechanics and Microengineering*, 11(1):55, 2001.

[21] Yong-Jun Kim and Mark G Allen. In situ measurement of mechanical properties of polyimide films using micromachined resonant string structures. *IEEE Transactions on Components and Packaging Technologies*, 22(2):282–290, 1999.

[22] Volker Ziebart, Oliver Paul, U Munch, Jürg Schwizer, and Henry Baltes. Mechanical properties of thin films from the load deflection of long clamped plates. *Journal of Microelectromechanical Systems*, 7 (3):320–328, 1998.

[23] Osamu Tabata, Ken Kawahata, Susumu Sugiyama, and Isemi Igarashi. Mechanical property measurements of thin films using load-deflection of composite rectangular membranes. *Sensors and actuators*, 20(1-2):135–141, 1989.

[24] Mark G Allen, Mehran Mehregany, Roger T Howe, and Stephen D Senturia. Microfabricated structures for the insitu measurement of residual stress, youngâĂŹs modulus, and ultimate strain of thin films. *Applied Physics Letters*, 51(4):241–243, 1987.

[25] H Guckel, D Burns, C Rutigliano, E Lovell, and B Choi. Diagnostic microstructures for the measurement of intrinsic strain in thin films. *Journal of Micromechanics and Microengineering*, 2(2):86, 1992.

[26] Brice Arrazat, Sebastian Orellana, Christian Rivero, P Fornara, Antonio Di Giacomo, and Karim Inal. From stress sensor towards back end of line embedded thermo-mechanical sensor. *Microelectronic Engineering*, 120:41–46, 2014.

[27] M Kasbari, C Rivero, S Blayac, F Cacho, and R Fortunier. Metallization local stress monitoring in industrial semiconductor processes. In *AIP Conference Proceedings*, volume 945, pages 21–26. AIP, 2007.

[28] AB Horsfall, JMM dos Santos, SM Soare, NG Wright, AG O'neill, SJ Bull, AJ Walton, AM Gundlach, and JTM Stevenson. Direct measurement of residual stress in sub-micron interconnects. *Semiconductor science and technology*, 18(11):992, 2003.

[29] Chi Shiang Pan and Wensyang Hsu. A microstructure for in situ determination of residual strain. *Journal of Microelectromechanical Systems*, 8(2):200–207, 1999.

[30] Liwei Lin, Albert P Pisano, and Roger T Howe. A micro strain gauge with mechanical amplifier. *Journal of Microelectromechanical Systems*, 6(4):313–321, 1997.

[31] Fredric Ericson, Staffan Greek, Jan Söderkvist, and Jan-Åke Schweitz. High-sensitivity surface micromachined structures for internal stress and stress gradient evaluation. *Journal of micromechanics and microengineering*, 7(1):30, 1997.

[32] Nathan D Masters, Maarten P de Boer, Brian D Jensen, Michael S Baker, and David Koester. Side-by-side comparison of passive mems strain test structures under residual compression. In *Mechanical Properties of Structural Films*. ASTM International, 2001.

[33] Yogesh B Gianchandani and Khalil Najafi. Bent-beam strain sensors. *Journal of Microelectromechanical Systems*, 5(1):52–58, 1996.

[34] P Goudeau, N Tamura, B Lavelle, S Rigo, T Masri, A Bosseboeuf, T Sarnet, J-A Petit, and J-M Desmarres. X-ray diffraction characterization of suspended structures for mems applications. 2005.

[35] URL `http://www.iue.tuwien.ac.at/phd/singulani/dissse17.html`.

[36] G Gerald Stoney. The tension of metallic films deposited by electrolysis. *Proceedings of the Royal Society of London Series A*, 82(553):172–175, 1909.

[37] GCAM Janssen, MM Abdalla, F Van Keulen, BR Pujada, and B Van Venrooy. Celebrating the 100th anniversary of the stoney equation for film stress: Developments from polycrystalline steel strips to single crystal silicon wafers. *Thin Solid Films*, 517(6):1858–1867, 2009.

[38] M Elwenspoek H A C Tilmans and J H Fluitman. *Sensors Actuators*. 1992.

[39] R. C. Hibbeler. *Mechanics of Materials*. Pearson, 8th edition, 2011.

Chapter 4

Reflection

This chapter provides a reflection on the work in this thesis. First, line of thought describes the design process of the measurement devices. Then, the original planning is compared to the actual spent time. The contributions of this thesis are briefly discussed. Finally, some recommendations for future research are given.

4.1 Line of thought

Although the literature review did not show any measurement methods to measure plastic strain, it was very helpful for inspiration. Both the narrow bent beams and lever mechanism could theoretically work to distinguish elastic and plastic strain, by etching the structures in the silicon layer. After oxidation they would show the combined elastic and plastic strain, and after the oxide is removed only the plastic strain remains. The lever mechanism was chosen, because this geometry induces less stress as a result of stiffness from the mechanism than for the narrow bent beams. The oxide film induces a tensile stress in the silicon, while the stiffness will induce a compressive stress. Therefore, the most tensile stress will be in the silicon beams if the stiffness is minimized. The total compressive stress on the oxidized silicon beams required a buckling analysis, to ensure proper working of the mechanism.

First, a linear buckling analysis was performed in COMSOL. This analysis showed that sideways buckling was likely to occur as a first buckling mode, while a rotational buckling was preferred as this was the intended motion. To overcome this, concepts with 3 and 4 beam configurations were simulated, where the extra beams constrained the sideways buckling. However, these configurations still showed unwanted buckling modes. To further analyze the buckling behavior, we performed nonlinear transient simulations. These simulations revealed that the sideways buckling would not occur for the simple 2-beam lever mechanism. The rotation of the lever prevents the buckling from happening. This was an interesting learning experience to see the limits of linear analysis, even though the rotations were small.

The original idea for the experiments was to use the same kind of FZ silicon wafers as used in previous work, where plastic deformation was observed. Unfortunately, the recipes for bulk DRIE could no longer be used, so this was not an option. The alternative was to join on a production batch of SOI wafers. The devices would then be etched in 50 µm thick epitaxial silicon, instead of 525 µm thick FZ silicon. This seemed like a great idea, because the thinner layer allowed for thinner beams. The oxide

thickness is limited by the oxidation time, which rapidly increases for oxide over 1 μm. Thinner beams mean a larger A_r is possible, so more plastic strain is expected. However, the experiments showed only very little plastic strain. Attempts were made with longer annealing and increasing the oxide thickness to 2 μm, but without success. Even though it was disappointing that we could not obtain larger plastic strains, this result is actually very useful for future work where plastic strain is to be avoided.

4.2 Work timeline

The original timeline and the actual course of events are shown in Tab. 4.1. Almost all steps took some more time than planned. It was substantially more difficult and time consuming than predicted to implement the plasticity model of silicon in a numerical model in MATLAB and COMSOL. Also, the need for the extensive buckling analysis was not accounted for in the original planning. The mask design needed some iterations to minimize risk of damage during fabrication. During fabrication, I could spend some time on writing the research paper, which minimized lost time. Looking back at the original timeline, it is safe to say that it was too ambitious.

Table 4.1: Timeline

Task	Planning	Actual
Literature review	Sep - Dec	Sep - Jan
Modeling in MATLAB	Jan	Feb - Mar
Modeling and analysis in COMSOL	Feb	Apr - Jul
Mask design	Apr	Jul - Aug
Fabrication	May	Aug - Sep
Experiments	Jun	Okt
Documentation	July-Aug	Nov - Dec

4.3 Contributions

The work in this thesis contributes to using thermal oxidation to accomplish static balancing, as proposed by P.R. Kuppens. The new knowledge that plastic deformations are very limited in epitaxial silicon is a useful in future designs exploiting thermal stress from oxidation. Static balancing is an important topic in MEMS, as the positive stiffness of conventional compliant stages is often a drawback. Translational stages that are statically balanced over a certain range are useful for a variety of applications, such as accurate force transmission, low frequency oscillators, and efficient mechanical motion amplifiers.

4.4 Recommendations

- Tensile or creep tests of epitaxial silicon samples at elevated temperature can give information on the early stage of plastic deformation. With such experiments, it might be possible to develop a better model to predict plastic strain in epitaxial silicon.
- Dislocation measurements in both the previously used FZ wafers and in the epitaxial silicon used in this study will add valuable information to support the conclusions. These measurements were unfortunately not feasible in this work.
- The same experiments should be performed on FZ wafers. This will make it possible to compare plastic strain in FZ silicon and epitaxial silicon for the exact same conditions. The samples could be fabricated from a FZ wafer, by first etching the mechanism from the front with DRIE. Then, the backside cavity could be etched with DRIE from the back. This should give the same dimensions for the lever mechanisms in FZ silicon.
- In this work, we only see the resulting deformations at room temperature. It would be interesting to see the deformations at higher temperatures as well. If we can see the deformations in situ during the cooling process, it would give stress information which can be used to validate parts of the model. For instance, this would give information on the viscous flow point of the oxide, and the amount of intrinsic stress in silicon dioxide grown at 900 °C.
- For future design of the lever mechanism, it is recommended to reduce the mass of the vernier scale on the lever beam. For the thinnest beams of 5 µm wide, the scale deflected slightly due to gravity. This made it more difficult to focus the microscope on both sides of the scale. The dimensions of the lever mechanism can be further optimized, depending on the objective. This could for instance be to minimize out of plane deflection, optimize strain resolution, or minimize mechanism stiffness.
- The working principle of the proposed measurement method should be validated for larger plastic strain. One method to achieve this could be to fabricate the samples using laser cutting. If the heat affected zone is deep enough, this could create enough initial dislocations to show plastic deformation. Another promising method is to dope the silicon with boron, as Maseeh and Senturia [2] have observed plastic deformation in heavily boron-doped oxidized silicon membranes. The silicon can be doped during epitaxy to obtain an uniform distribution.

Chapter 5

Conclusion

Thermal oxidation of thin silicon beams in MEMS can cause plastic deformations, as a result of thermal stress induced by the oxide film. It was found that there are many measurement methods to measure elastic strain as a result of residual stress, but there are currently no measurement methods to measure plastic strain.

In this thesis, a novel method is presented to distinguish elastic and plastic strain in silicon beams as a result of thermal oxidation. A lever mechanism is used as a mechanical amplifier to obtain a sufficient measurement resolution. The combined elastic and plastic strain is measured after oxidation, and the plastic strain is measured after the oxide is removed. Experimental measurements are performed in epitaxial silicon samples, with oxidation temperatures from 900 °C to 1100 °C. Beams aligned to the <100> and <110> directions, with widths of 5 µm, 10 µm, and 15 µm are tested with 1 µm and 2 µm thick oxide. A model is presented that predicts the elastic and plastic strain in the silicon beam during cooling. The commonly used AH plasticity model for silicon was used.

The maximum observed strain was 0.006 %, which is significantly less than predicted by the model. We conclude that the AH model is not valid for epitaxial silicon with low or zero dislocations. Significant plastic deformation in FZ silicon samples as a result of thermal oxidation was observed in earlier research. Epitaxial silicon is therefore a better choice over FZ silicon, if plastic deformation is to be avoided.

Elastic strains were observed from 0.019 % to 0.135 %. The model predicts the elastic strain well for oxidation temperatures of 950 °C to 1100 °C. For oxidation at 900 °C, the model underestimates the elastic strain. This is because stress due to volume expansion during growth of the oxide is neglected in the model.

More research is needed to understand plasticity in epitaxial silicon and to develop a more accurate model. To achieve this, tensile or creep tests of epitaxial silicon samples at elevated temperature are recommended to give information on the early stage of plastic deformation.

Appendix A

Modeling

This appendix describes the models used to predict elastic and plastic strain in an oxidized silicon beam during cooling. First, the numerical model is discussed. Then, the implementation of the material models in COMSOL is shown. Finally, the models are verified by reproducing tensile tests from literature. Plastic and elastic strain during cooling of a beam are simulated in both the numerical model and in COMSOL, and results are compared.

A.1 Numerical model

The model describes strain in a oxidized cantilever fixed-free beam. The cross section is shown in figure A.1. Silicon and silicon dioxide have different coefficients of thermal expansion (CTE). The CTE of silicon is higher than the CTE of silicon dioxide, which means that silicon shrinks more than the oxide in the cooling process, if the two materials were not connected. However, both materials are connected at the interface, and thus need to have the same total strain and strain rate at all times:

$$\dot{\varepsilon}_{Si,tot} = \dot{\varepsilon}_{SiO_2,tot} \tag{A.1}$$

Since the two materials are connected, and thus have the same strain at the interface, a stress is developed to ensure equal strain in both materials. This stress causes a elastic, and possible plastic strain in the materials in order to meet the criterion of equal strain. The total strains and strain rates for the silicon and silicon dioxide should be the same at all times during cooling, since they are connected at the interface. The total axial strain of a silicon beam can be expressed as rate equations: (This is convenient because the plastic behavior of silicon is described by rate equations)

$$\dot{\varepsilon}_{tot} = \dot{\varepsilon}_{th} + \dot{\varepsilon}_{el} + \dot{\varepsilon}_{pl} \tag{A.2}$$

Where $\dot{\varepsilon}_{tot}$ is the total strain rate of the beam, $\dot{\varepsilon}_{th}$ the thermal strain rate, $\dot{\varepsilon}_{el}$ the elastic strain rate, and $\dot{\varepsilon}_{pl}$ the plastic strain rate. Since the total strain of the silicon and silicon dioxide is equal, the following relation is obtained by combining equation A.1 and A.2:

$$\dot{\varepsilon}_{Si,th} + \dot{\varepsilon}_{Si,el} + \dot{\varepsilon}_{Si,pl} = \dot{\varepsilon}_{SiO_2,th} + \dot{\varepsilon}_{SiO_2,el} + \dot{\varepsilon}_{SiO_2,pl} \tag{A.3}$$

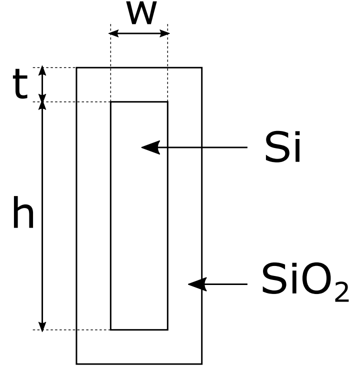

Figure A.1: Cross section of oxidized silicon beam

Plastic strain in silicon

Plastic strain in silicon is governed by movement of dislocations. The crystal lattice is rearranged when dislocations move, causing permanent deformations. Dislocations can move on the {111} planes, where the atoms are the most closely packed[5]. The dislocations can move on this planes in the <110> directions. This gives a total of 12 slip systems, consisting of 4 slip planes with 3 slip directions each. The combinations are shown in table A.1[6]. Each slip systems is assigned a number for convenience.

Table A.1: Slip systems

	1	2	3	4	5	6	7	8	9	10	11	12
s	$[\bar{1}0\bar{1}]$	$[011]$	$[1\bar{1}0]$	$[\bar{1}\bar{1}0]$	$[011]$	$[10\bar{1}]$	$[\bar{1}0\bar{1}]$	$[110]$	$[0\bar{1}1]$	$[10\bar{1}]$	$[0\bar{1}1]$	$[\bar{1}10]$
n	$(\bar{1}\bar{1}1)$	$(\bar{1}\bar{1}1)$	$(\bar{1}\bar{1}1)$	$(1\bar{1}1)$	$(1\bar{1}1)$	$(1\bar{1}1)$	$(\bar{1}11)$	$(\bar{1}11)$	$(\bar{1}11)$	(111)	(111)	(111)

The shear stress acting on a slip system can cause the dislocation to move. This is called the resolved shear stress τ_r. In the modeled beam, an axial tensile stress is applied by the oxide. No shear stress is applied, so the only stress source is axial. The Schmid factor M describes the resolved shear stress as a result of an axial stress. M depends on the relative orientation of the slip plane and the slip direction to the applied stress. This is illustrated in figure A.2. The resolved shear stress on a slip system is then:

$$\tau_r = \frac{\text{resolved shear force}}{\text{slip plane area}} = \frac{F\cos\lambda}{\frac{A}{\cos\phi}} = \frac{F}{A}\cos\lambda\cos\phi = \sigma\cos\lambda\cos\phi \tag{A.4}$$

$$\tau_r = M\sigma, \text{ where } M = \cos\lambda\cos\phi \tag{A.5}$$

The angles ϕ and λ depend on the orientation of the crystal, and the active slip system, as illustrated in figure A.2. In vector notation, a cosine can be calculated by:

$$\cos\theta = \frac{\mathbf{a}\cdot\mathbf{b}}{\|\mathbf{a}\|\,\|\mathbf{b}\|} \tag{A.6}$$

with θ the angle between **a** and **b**. Combining equation A.5 and A.6 gives:

$$M = \frac{\mathbf{u} \cdot \mathbf{s}}{\|\mathbf{u}\| \|\mathbf{s}\|} \frac{\mathbf{u} \cdot \mathbf{n}}{\|\mathbf{u}\| \|\mathbf{n}\|} \tag{A.7}$$

Where **u** is the direction of axial stress, **n** the slip plane normal, and **s** the slip direction. The slip system with the highest Schmid factor M will first generate macroscopic plastic strain[7]. It is assumed that only the slip system(s) with the largest resolved shear stress, and thus with highest M, are active. The other slip systems are neglected. The beams are aligned to the <100> and <110> directions. The Schmid factors for axial stress in these directions are shown in table A.2. For the <100> aligned beams, 8 slip systems are active with an absolute value of 0.4082 for the Schmid factor. For the <110>, 4 slip systems are active with an absolute value of 0.4082 for the Schmid factor.

Table A.2: Schmid factors for <100> and <110> aligned beams.

Slip system	<100>	<110>
1	0.4082	0.4082
2	0	-0.4082
3	-0.4082	0
4	-0.4082	0
5	0	0
6	0.4082	0
7	0.4082	0
8	-0.4082	0
9	0	0
10	0.4082	0.4082
12	0	-0.4082
13	-0.4082	0

For a single active slip system, the axially observed plastic strain rate $\dot{\varepsilon}$ is equal to the plastic shear strain rate $\dot{\gamma}$ times the Schmid factor. The active slip systems are assumed to move independently from each other, so the total axial plastic strain rate $\varepsilon_{si,pl}$ is:

$$\dot{\varepsilon}_{si,pl} = \dot{\gamma}_{si,pl} M n \tag{A.8}$$

Where n is the number of active slip systems, which is 8 for the <100> direction, and 4 for the <110> direction, and $\dot{\gamma}_{si,pl}$ the plastic shear strain rate in the direction of the slip system. It is assumed that only the primary slip systems, which have the same maximum M value, are active. Slip in other slip systems with lower M are neglected.

The macroscopic plastic shear strain rate for a slip system is given by the Orowan equation [9]:

$$\dot{\gamma}_{si,pl} = N_m v b \tag{A.9}$$

Where N_m is the mobile dislocation density of the slip system, v the average slip velocity, and b the Burgers vector. All dislocations are assumed to be mobile. Combined with equation A.8, the plastic strain rate becomes:

$$\dot{\varepsilon}_{si,pl} = M n N_m v b \tag{A.10}$$

The model by Alexander and Haassen (AH) [10] is universally used to describe dislocation velocity and evolution of the dislocation density. The parameter values from Yonenaga and Sumino [11] are used

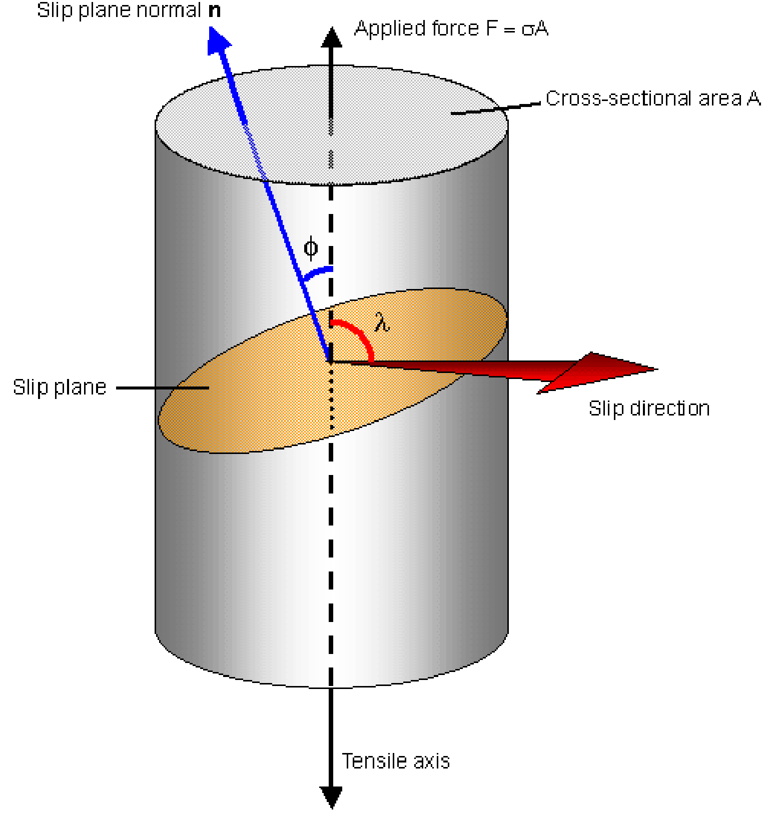

Figure A.2: Sketch of schmid factor. Image adapted from MET [8].

in this model. The average dislocation velocity v is:

$$v = B_0 \left(\frac{\tau_{eff}}{\tau_0}\right)^m \exp\left(\frac{-Q}{k_b T}\right) \tag{A.11}$$

Where B_0 is a reference velocity, τ_{eff} the effective shear stress, τ_0 a reference stress, Q the activation energy, k_b the Boltzmann constant, and T the temperature. The effective shear stress on the dislocations consist of the applied shear stress τ_a and an opposite interaction stress between moving dislocations τ_i [12]. The higher the dislocation density, more stress is required to move dislocations at the same rate. The effective shear stress τ_{eff} is given by:

$$\tau_{eff} = \left\langle \sigma M - \frac{Gb\sqrt{N_m}}{\beta} \right\rangle \tag{A.12}$$

Where σM is the applied shear stress, and $\frac{Gb\sqrt{N_m}}{\beta}$ the interaction stress. G is the shear modulus of silicon, and β a parameter characterizing the interaction between dislocations. β is determined by Yonenaga and Sumino [11] for experiments with a constant strain rate of $1.2 \times 10^{-4}\,\mathrm{s}^{-1}$, $T = 800\,°\mathrm{C}$, and an initial dislocation density of $N_0 = 2 \times 10^4\,\mathrm{cm}^{-1}$. If $x > 0$, $\langle x \rangle = x$, and if $x \leq 0$, $\langle x \rangle = 0$. The dislocation density is assumed to increase proportionally to the area swept by the dislocations and the effective shear stress: [11]

$$\dot{N}_m = K N_m v \tau_{eff} \tag{A.13}$$

Where K is a constant with value $3.1 \times 10^{-4}\,\mathrm{m\,N^{-1}}$. This value is experimentally determined to fit the upper yield stress in experiments from Yonenaga and Sumino [11]. K is determined for a tensile test with a constant strain rate of $1.2 \times 10^{-4}\,\mathrm{s^{-1}}$, $T = 800\,^{\circ}\mathrm{C}$, and an initial dislocation density of $N_0 = 2 \times 10^4\,\mathrm{cm^{-1}}$.

The parameter values for the plasticity model of silicon are summarized in table A.3.

Table A.3: Parameter values plasticity model silicon

Parameter	Value	Source
K	$3.1 \times 10^{-4}\,\mathrm{m\,N^{-1}}$	[11]
B_0	$4.3 \times 10^{4}\,\mathrm{m\,s^{-1}}$	[12]
τ_0	10 MPa	[12]
b	$3.83 \times 10^{-10}\,\mathrm{m}$	[13]
β	3.3	[11]
m	1.1	[11]
Q	2.17 eV	[12]
k_b	$1.380\,648\,52 \times 10^{-23}\,\mathrm{m^2\,kg\,s^{-2}\,K^{-1}}$	
G	80 GPa	

Since the beam is free on one end, there must be force equilibrium between silicon and silicon dioxide.

$$\sigma_{Si} A_{Si} = \sigma_{SiO2} A_{SiO2} \tag{A.14}$$

Where A_{Si} is the cross sectional area of the silicon, and A_{SiO2} the cross sectional area of the silicon dioxide. This allows the stress in silicon dioxide to be written in terms of the stress in silicon:

$$\sigma_{SiO_2} = \frac{-\sigma}{A_r} \tag{A.15}$$

Where A_r the ratio of cross sectional area of silicon dioxide over silicon. The cross sectional area for silicon and silicon dioxide are:

$$A_{Si} = wh \tag{A.16}$$

$$A_{SiO_2} = (h + 2t)(w + 2t) - wh \tag{A.17}$$

Where w is the beam width, h the beam thickness (or height), and t the oxide thickness. This is also illustrated in figure A.1.

Plastic strain in silicon dioxide

Silicon dioxide is modeled as a viscoelastic material, known as a Maxwell material [14]. The plastic strain rate is:

$$\dot{\varepsilon}_{SiO2,pl} = \frac{\sigma_{SiO2}}{\eta} \tag{A.18}$$

Where η is the viscosity. Rewriting in terms of stress in silicon gives:

$$\dot{\varepsilon}_{SiO2,pl} = \frac{\sigma_{Si}}{\eta A_r} \tag{A.19}$$

The viscosity is temperature dependent:

$$\eta(T) = \eta_0 \exp\left(\frac{E_\eta}{RT}\right) \tag{A.20}$$

Where $\eta(T)$ is the viscosity, η_0 a constant, E_η the activation energy. As temperature rises, the viscosity decreases rapidly. Values for η_0 and E_η are calculated from experimental data from Irene et al. [14]. The relaxation time for silicon dioxide grown at 1100 °C and 800 °C are used to calculate η_0 and E_η, and are 9.3998×10^{-12} Pa s and 5.9045×10^5 J mol^{-1}.

Elastic strain in silicon

Silicon is a anisotropic material. The relation between stress and strain is given by the compliance tensor S.

$$\epsilon_{ij} = S_{ijkl}\sigma_{kl} \tag{A.21}$$

In theory there can be 81 variables in S. For silicon, there are only 3 independent variables in the elasticity tensor, due to equivalence of shear conditions and cubic symmetry. The relation between stress and strain for silicon can be seen in equation A.22. Here, simplified subscripts are used, which are explained in table A.4.

$$\begin{bmatrix}\epsilon_1\\\epsilon_2\\\epsilon_3\\\epsilon_4\\\epsilon_5\\\epsilon_6\end{bmatrix} = \begin{bmatrix} s_{11} & s_{12} & s_{12} & 0 & 0 & 0\\ s_{12} & s_{11} & s_{12} & 0 & 0 & 0\\ s_{12} & s_{12} & s_{11} & 0 & 0 & 0\\ 0 & 0 & 0 & s_{44} & 0 & 0\\ 0 & 0 & 0 & 0 & s_{44} & 0\\ 0 & 0 & 0 & 0 & 0 & s_{44}\end{bmatrix}\begin{bmatrix}\sigma_1\\\sigma_2\\\sigma_3\\\sigma_4\\\sigma_5\\\sigma_6\end{bmatrix} \tag{A.22}$$

Table A.4: Simplified subscripts

Direction/face	Simplified subscript
xx or 11	1
yy or 22	2
zz or 33	3
yz or 23	4
zx or 31	5
xy or 12	6

If the stress-strain relation is needed in a different direction, the tensor must be rotated using tensor transformations, so that one of the axes is aligned with the desired direction. There are shortcut formula's to calculate values for the Young's modulus and Poisson's ratio for common cases [15]. The cantilever beams aligned with the <100> and <110> directions have elasticity moduli:

$$E_{si,100} = \frac{1}{s_{11}} \tag{A.23}$$

and

$$E_{si,110} = \frac{4}{2s_{11} + 2s_{12} + s_{44}} \tag{A.24}$$

where s_{11}, s_{12}, and s_{44} are components in the compliance tensor. The elasticity modulus is slightly dependent on the temperature. A second order polynomial fit on the components of the compliance tensor found by Bourgeois et al. [16] are used in this model.

$$s_{ij} = B_0 + B_1(T-25) + B_2(T-25)^2 \tag{A.25}$$

Where s_{ij} are the coefficients of the compliance matrix, B_0, B_1, B_2 are constants, and T is the temperature in °C. The values for B_0, B_1, B_2 depend on s_{ij} and are shown in table A.5.

Table A.5: Temperature dependent coefficients for compliance matrix silicon

s_{ij}	B_0	B_1	B_2
s_{11}	7.69×10^{-12}	64.73×10^{-6}	61.19×10^{-9}
s_{12}	-2.14×10^{-12}	51.48×10^{-6}	72.26×10^{-9}
s_{44}	12.58×10^{-12}	60.14×10^{-6}	54.90×10^{-9}

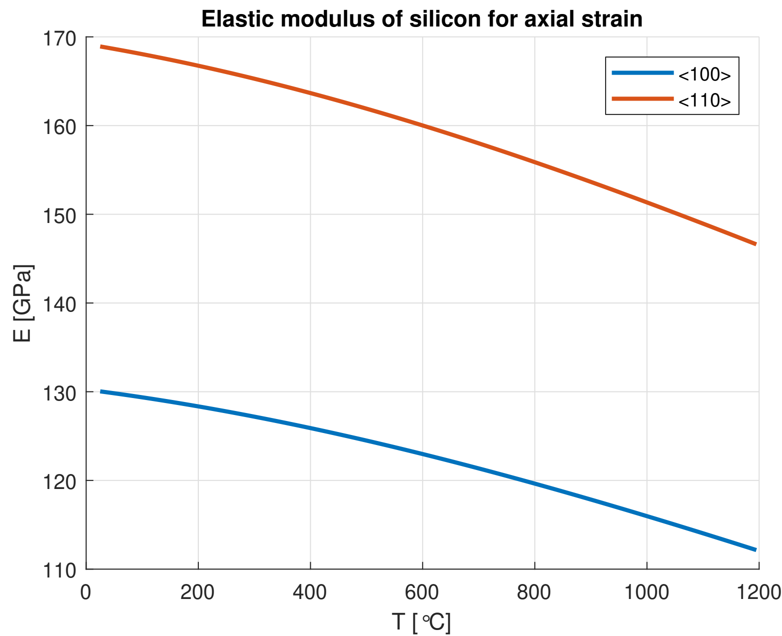

Figure A.3: E for uniaxial tension of silicon for directions <100> and <110>

The elastic strain rate of silicon in the cantilever beam is:

$$\dot{\varepsilon}_{Si,el} = \frac{\dot{\sigma}}{E_{si}} \tag{A.26}$$

Elastic strain in silicon dioxide

Silicon dioxide is an isotropic material, with a elasticity modulus of 64 GPa which is assumed to be independent of temperature [17]. The elastic strain rate for silicon dioxide, as a function of the stress

in silicon, is:

$$\dot{\varepsilon}_{SiO2,el} = \frac{-\dot{\sigma}}{A_r E_{SiO_2}} \tag{A.27}$$

Thermal strain

The thermal strain rates for silicon is given by:

$$\dot{\varepsilon}_{Si,th} = \alpha_{Si} \dot{T} \tag{A.28}$$

The thermal strain rate for silicon dioxide has an additional term, which comes from the strain constraint in the lateral direction. The silicon dioxide must have the same lateral strain as the silicon, because they are connected. This means that there is lateral stress in the silicon dioxide, which has effect on the axial thermal strain. The thermal strain rate for silicon dioxide is given by:

$$\dot{\varepsilon}_{SiO_2,th} = \alpha_{SiO_2} \dot{T} + \left(\alpha_{SiO_2} - \alpha_{Si}\right) \nu \dot{T} \tag{A.29}$$

Where α_{Si} and α_{SiO_2} are the coefficients of thermal expansion for silicon and silicon dioxide, $\dot{T}$ the temperature rate, and ν the Poisson ratio of silicon dioxide. The empirical temperature dependence for α_{Si} determined by Okada and Tokumaru [18] is used for silicon:

$$\alpha_{Si}(T) = \left[3.725\left(1 - \exp\left(-5.88 \times 10^{-3}(T - 124)\right)\right) + 5.548T \times 10^{-4}\right] \times 10^{-6} \tag{A.30}$$

Tada et al. [17] have shown that the TCE of silicon dioxide is constant at $5 \times 10^{-7}\,\mathrm{K}^{-1}$up to about 300 °C, and increases linearly to $1.83 \times 10^{-6}\,\mathrm{K}^{-1}$ at 1000 °C. The thermal coefficient of expansion for silicon dioxide $\alpha_{SiO_2}(T)$ is then described by:

$$\alpha_{SiO_2}(T) = \begin{cases} 0.5 \times 10^{-6}\,\mathrm{K}^{-1} & \text{for } T \leqslant 573.15\,\mathrm{K} \\ (0.0019 \cdot (T - 573.15) + 0.5) \times 10^{-6}\mathrm{K}^{-1} & \text{for } T > 573.15\,\mathrm{K} \end{cases} \tag{A.31}$$

The coefficients of thermal expansion of Si and SiO2 are shown as a function of temperature in figure A.4.

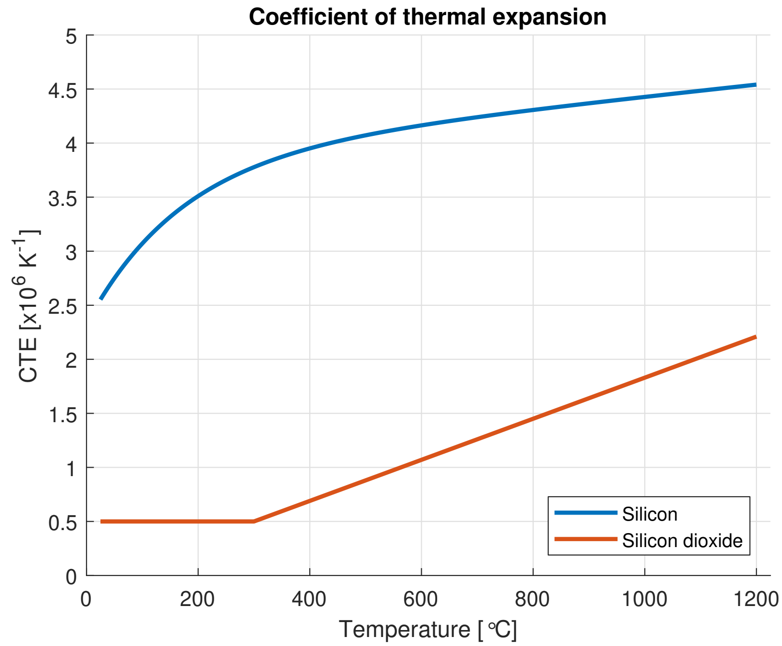

Figure A.4: CTE of silicon and silicon dioxide as a function of temperature.

Combined equations

The elastic, plastic and thermal strain in both silicon and silicon dioxide at room temperature are obtained by solving a set of couples differential equations numerically. Using the previous equations and their relations, the differential equations in A.33 are obtained. The input is a temperature profile as a function of time, so $\dot{T}$ is known. The initial values are shown in equation A.34. The ODE45 solver in MatLab is used, with a max time step of 60 seconds to ensure the steps are not too large to deal with sudden changes in material properties or temperature.

$$y = \begin{bmatrix} y_1 \\ y_2 \\ y_3 \\ y_4 \\ y_5 \\ y_6 \\ y_7 \\ y_8 \\ y_9 \\ y_{10} \end{bmatrix} = \begin{bmatrix} \sigma \\ T \\ N_m \\ \varepsilon_{total} \\ \varepsilon_{Si,th} \\ \varepsilon_{SiO_2,th} \\ \varepsilon_{Si,el} \\ \varepsilon_{SiO_2,el} \\ \varepsilon_{Si,pl} \\ \varepsilon_{SiO_2,pl} \end{bmatrix} \tag{A.32}$$

$$\dot{y} = \begin{bmatrix} \dot{y}_1 \\ \dot{y}_2 \\ \dot{y}_3 \\ \dot{y}_4 \\ \dot{y}_5 \\ \dot{y}_6 \\ \dot{y}_7 \\ \dot{y}_8 \\ \dot{y}_9 \\ \dot{y}_{10} \end{bmatrix} = \begin{bmatrix} \dot{\sigma} \\ \dot{T} \\ \dot{N}_m \\ \dot{\varepsilon}_{total} \\ \dot{\varepsilon}_{Si,th} \\ \dot{\varepsilon}_{SiO_2,th} \\ \dot{\varepsilon}_{Si,el} \\ \dot{\varepsilon}_{SiO_2,el} \\ \dot{\varepsilon}_{Si,pl} \\ \dot{\varepsilon}_{SiO_2,pl} \end{bmatrix} = \begin{bmatrix} \frac{\dot{y}_6 - \dot{y}_5 - \dot{y}_9 + \dot{y}_{10}}{\frac{1}{E_{Si}} + \frac{1}{A_r E_{SiO2}}} \\ \dot{y}_2 \\ K y_3 v \tau_{eff} \\ \dot{y}_5 + \dot{y}_7 + \dot{y}_9 \\ \alpha_{Si} \dot{y}_2 \\ \alpha_{SiO_2} \dot{y}_2 \\ \frac{\dot{y}_1}{E_{Si}} \\ \frac{-\dot{y}_1}{A_r E_{SiO_2}} \\ M n y_3 v b \\ \frac{-y_1}{A_r x} \end{bmatrix} \tag{A.33}$$

Initial conditions:

$$y_0 = \begin{bmatrix} y_{1,0} \\ y_{2,0} \\ y_{3,0} \\ y_{4,0} \\ y_{5,0} \\ y_{6,0} \\ y_{7,0} \\ y_{8,0} \\ y_{9,0} \\ y_{10,0} \end{bmatrix} = \begin{bmatrix} 0 \\ T_{ox} \\ N_{m,0} \\ 0 \\ 0 \\ 0 \\ 0 \\ 0 \\ 0 \\ 0 \end{bmatrix} \tag{A.34}$$

Where T_{ox} is the oxidation temperature, and $N_{m,0}$ the initial dislocation density.

A.2 FEM model

A 2D FEM model is made in COMSOL. The model uses quasi-static transient behavior. The simulations with this model are performed in the time domain. The plasticity model of silicon is implemented by using a Domain ODE for the dislocation density, as shown in figure A.5.

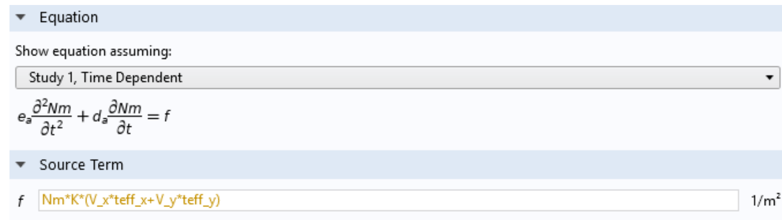

Figure A.5: Domain ODE for the dislocation density

A user defined creep strain rate tensor is used to implement the plastic strain rate in the x and y direction, as shown in figure A.6.

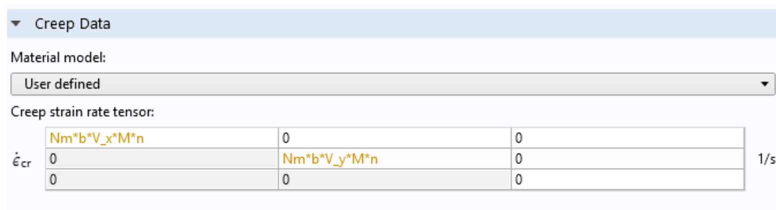

Figure A.6: Custom creep tensor for silicon

The temperature dependent coefficients of the stiffness tensor from Bourgeois et al. [16] are used in the elasticity matrix for silicon:

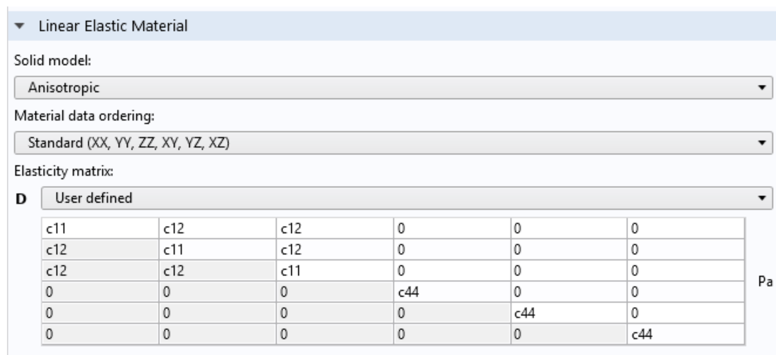

Figure A.7: Elasticity matrix for silicon

The viscosity of silicon dioxide is implemented using a user defined creep strain rate tensor:

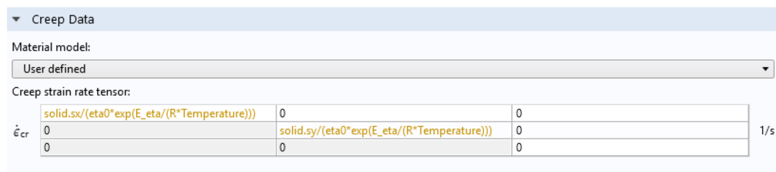

Figure A.8: Viscosity of silicon dioxide

The elasticity of silicon dioxide is modeled as a linear elastic isotropic material, with a Young's modulus of 64 GPa and a Poisson's ratio of 0.17. The thermal strain is modeled using the same coefficients of thermal expansion as in the numerical model.

A.3 Model verification

Tensile test

Tensile tests are simulated with the numerical model in MATLAB and in COMSOL. These are compared with literature to verify correct implementation of the plasticity model. The validated stress-strain curves from Yonenaga and Sumino [11] are used to validate the MATLAB model, which is shown in figure A.9. Tensile tests with $N_{m,0} = 2 \times 10^4\,\mathrm{cm}^{-2}$ at different temperatures are simulated. The virtual sample is stretched with a constant strain rate of $\dot{\varepsilon} = 1.2 \times 10^{-4}\,\mathrm{s}^{-1}$, and the resolved shear stress is plotted on the y axis. The samples from Yonenaga and Sumino [11] were clamped by a non rigid members, which is the reason for different elastic slopes for the different temperatures. The slopes are used to calibrate the flexible members in the MATLAB model. The MATLAB model reproduces the model from literature very accurately, as shown in figure A.10. This verifies that the MATLAB model of plastic strain is accurate.

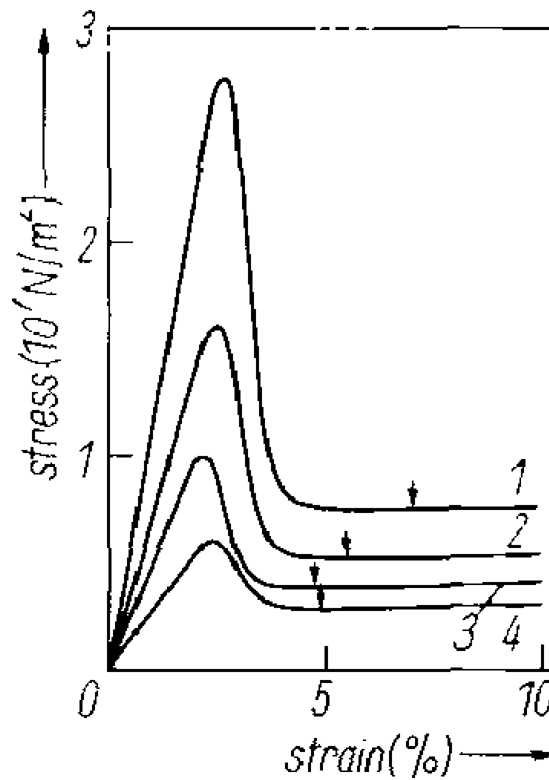

Figure A.9: Model simulations by Yonenaga and Sumino [11]. Resolved shear stress-shear strain curves for $\dot{\varepsilon} = 1.2 \times 10^{-4}\,\mathrm{s}^{-1}$ at various temperatures calculated with $N_{m,0} = 2 \times 10^4\,\mathrm{cm}^{-2}$. Marks show the lower yield points. (1) $T = 800\,°\mathrm{C}$, (2) 850 °C, (3) 900 °C, (4) 950 °C

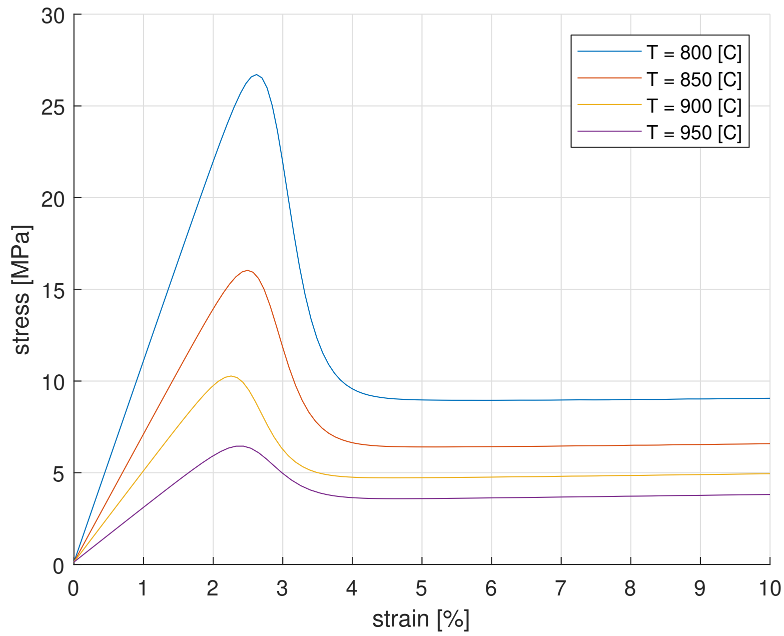

Figure A.10: Matlab simulations to verify the model.

Virtual tensile tests are simulated in MATLAB and COMSOL, without a flexible clamp. This shows the actual axial stress and strain in silicon. Figure A.11 and A.12 show that the models produce the same results. This verifies the plasticity model in COMSOL. The beam used in this study is shown in figure A.13. The beam is fixed on the left end, and a prescribed displacement was applied to the edge on the right. The silicon dioxide film was disabled by setting the Young's modulus to zero.

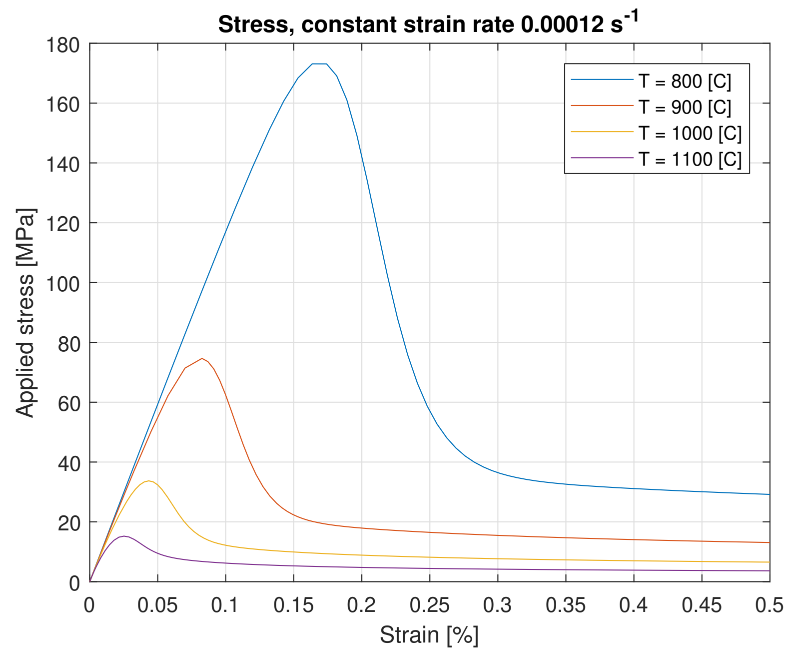

Figure A.11: Tensile test simulation in MatLab

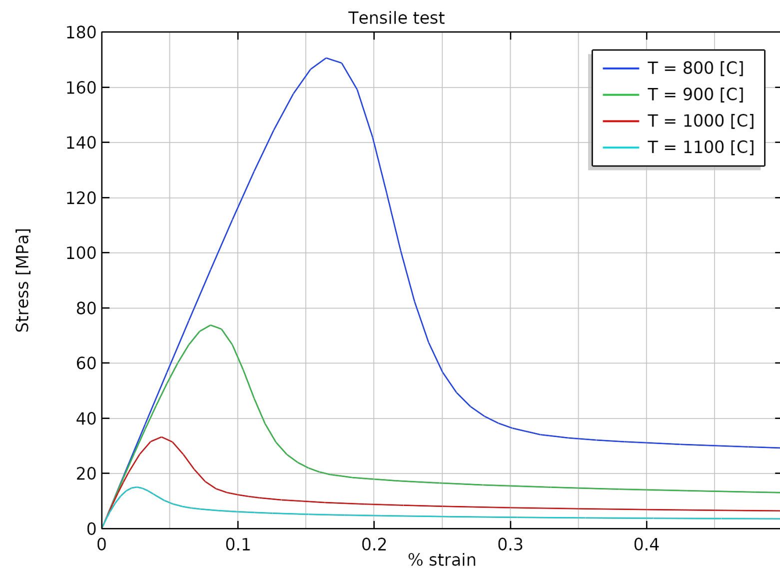

Figure A.12: Tensile test simulation in COMSOL

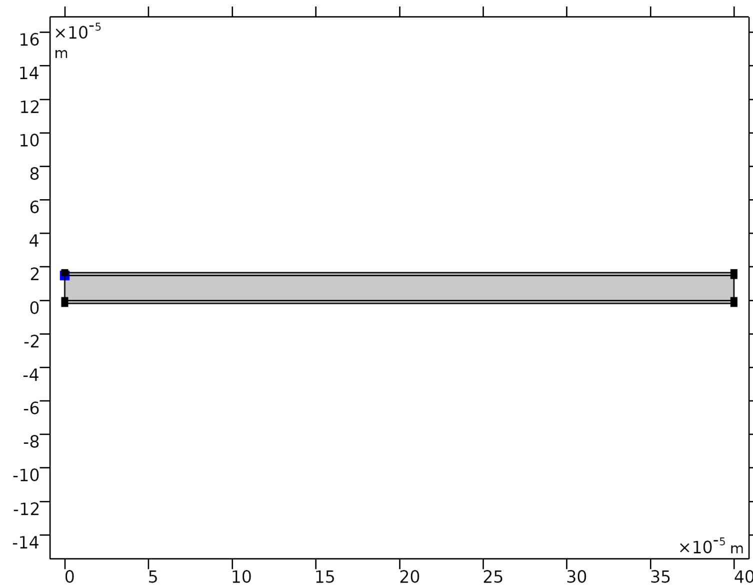

Figure A.13: Beam used in COMSOL to simulate the tensile test.

Beam cooling

In both MATLAB and COMSOL cooling of an oxidized silicon beam is modeled. The COMSOL model is used to verify the assumption of uniform stress in the silicon and silicon dioxide. Since the COMSOL model is 2d, the oxide is on only 2 sides of the beam. The oxide thickness is adjusted in the COMSOL model to obtain the same ratio of cross sectional area of silicon and silicon dioxide. For this simulation, a constant cooling of $-0.1\,°\mathrm{C\,s^{-1}}$ rate is assumed. The start temperature (oxidation temperature) is 1200 °C, and the beam is cooled to a room temperature of 25 °C. The resulting elastic, plastic, and total strain for both models are shown in figure A.14 and A.15. The results are very similar, both models predict almost the same strains.

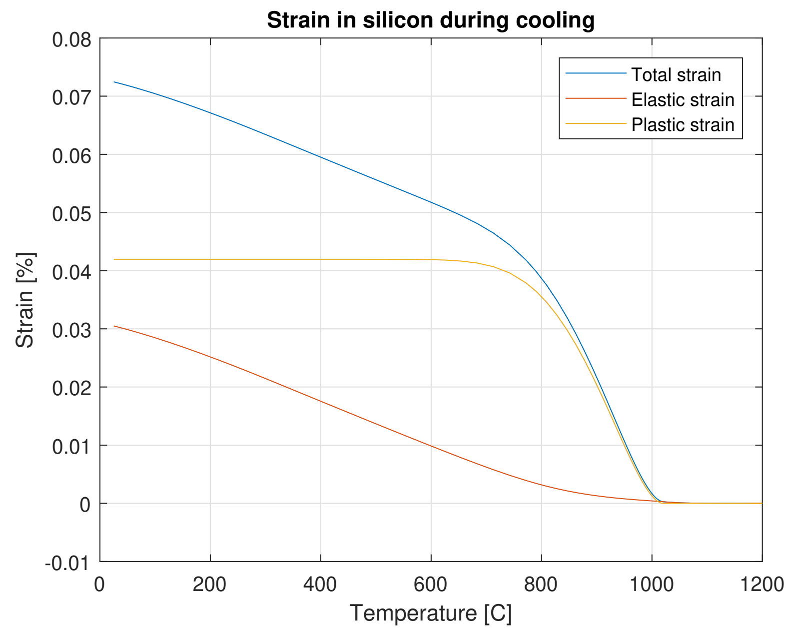

Figure A.14

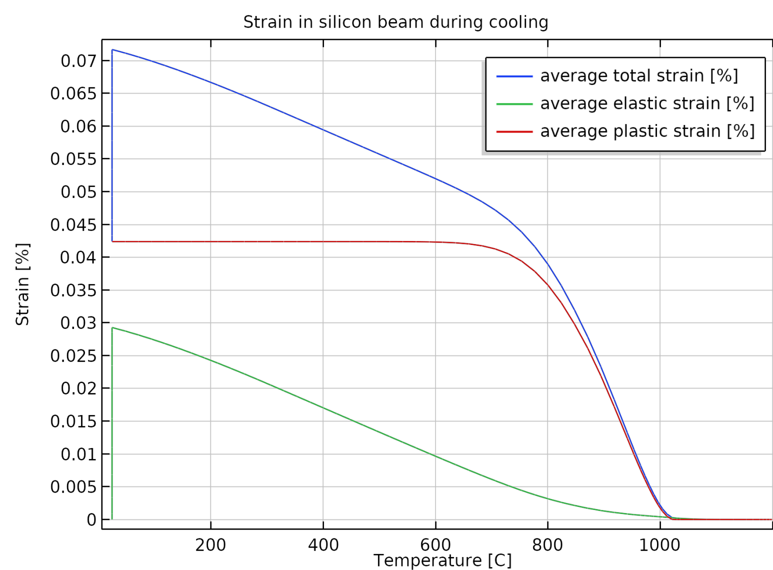

Figure A.15

Figures A.16, A.17, and A.18 show the stress distribution in the beam during cooling. From figure A.17 we can see that at the tip the stress is not uniform in the materials. In the rest of the beam, the stress is uniform. Since the beams in the experiments are much longer than wide, this stress non-uniformity at the tip can be neglected as it is a very small part of the beam. The beam in these simulations is

relatively wider than in the experiments. Together with the quantitative strain results from figures A.14 and A.15, we can conclude that the assumption of uniformly distributed stress in the MATLAB model is valid.

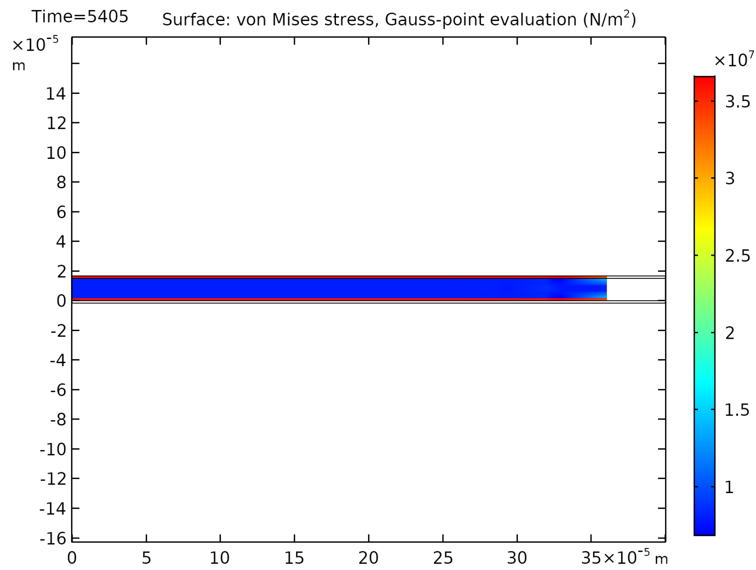

Figure A.16: Stress distribution in the beam during cooling.

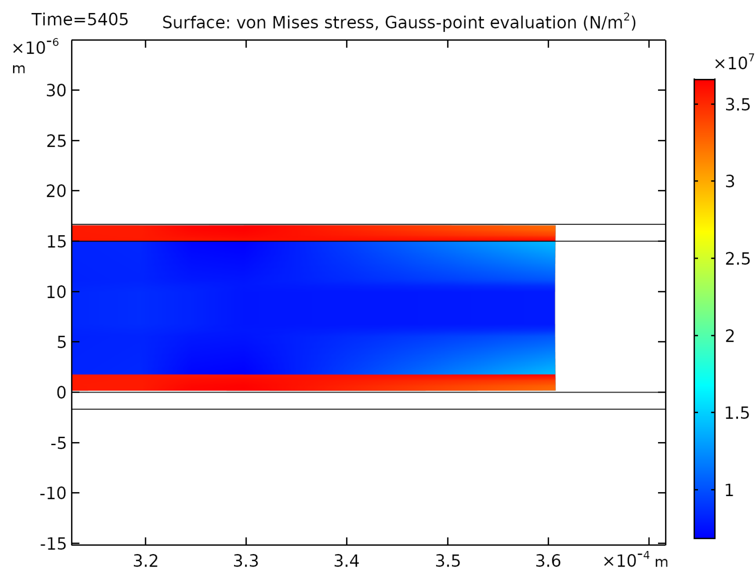

Figure A.17: Stress distribution at the beam tip during cooling.

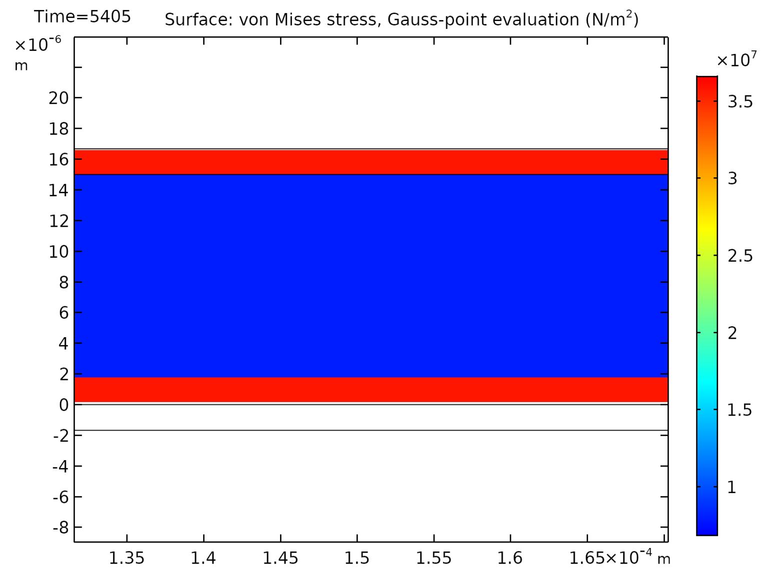

Figure A.18: Stress distribution close-up in the middle of the beam.

Appendix B

Lever mechanism analysis

This appendix contains extra analysis on the lever mechanism. First, the buckling analysis is described. Next, the stiffness of the mechanism is calculated. The resulting stress as a result of this stiffness is compared to stress induced by the oxide. Finally, a sensitivity analysis is performed, to analyze how changes in model parameters influence elastic and plastic strain.

B.1 Buckling analysis

The thin beams elongate because of the induced stress. This means the structure is under compressive load, and might be prone to buckling. A linear buckling analysis is performed in COMSOL to identify the first buckling mode. A nonlinear buckling analysis is performed to evaluate whether this buckling mode will happen during cooling.

Linear buckling analysis

The linear buckling analysis is performed for two beam widths, 4 μm and 16 μm. These are the extreme values that can be expected in worst case after fabrication, so they describe the extreme cases for buckling modes. For both beam widths the first buckling mode is the same, which is shown in figure B.1.

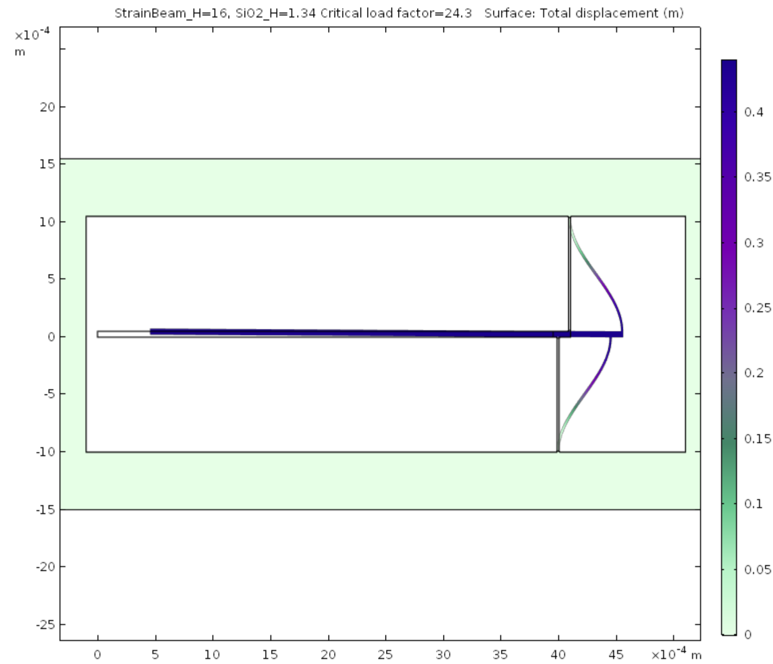

Figure B.1: First linear buckling mode.

Nonlinear buckling analysis

A perturbation to the mesh in the shape of the first buckling mode of the beam width is added to the lever mechanism with 4 µm and 16 µm beams. The mesh of the deformed initial shape for the 16 µm beam is shown in figure B.2. The cooling is simulated for the extreme case of about twice the difference in temperature, from 1200 °C to −1000 °C. The cooling is simulated for deformed and undeformed initial shapes. The simulation is run with nonlinear geometric effects enabled. The buckling does not occur for these extreme cases, so it can be concluded that sideways buckling is very unlikely to occur in the experiments. The rotation of the lever is favored over the sideways linear buckling mode. The results are shown in figures B.3, B.4, B.5, and B.6.

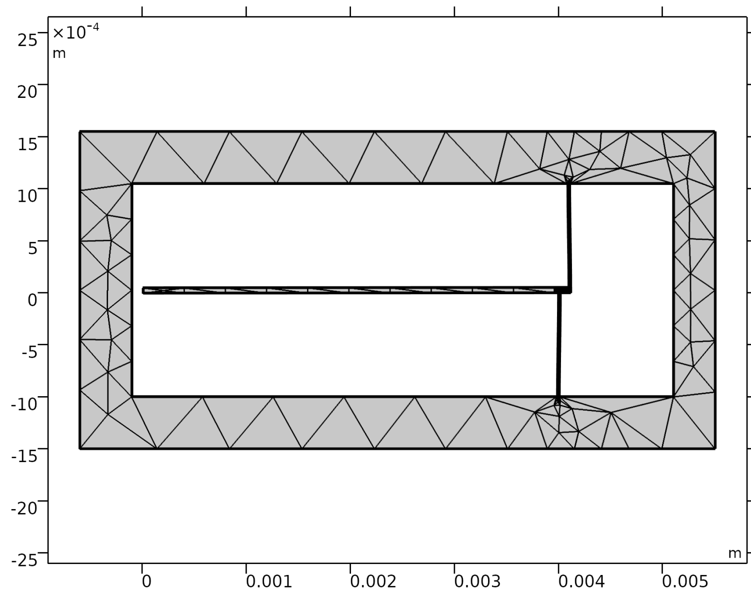

Figure B.2: Deformed mesh for 16 μm beams.

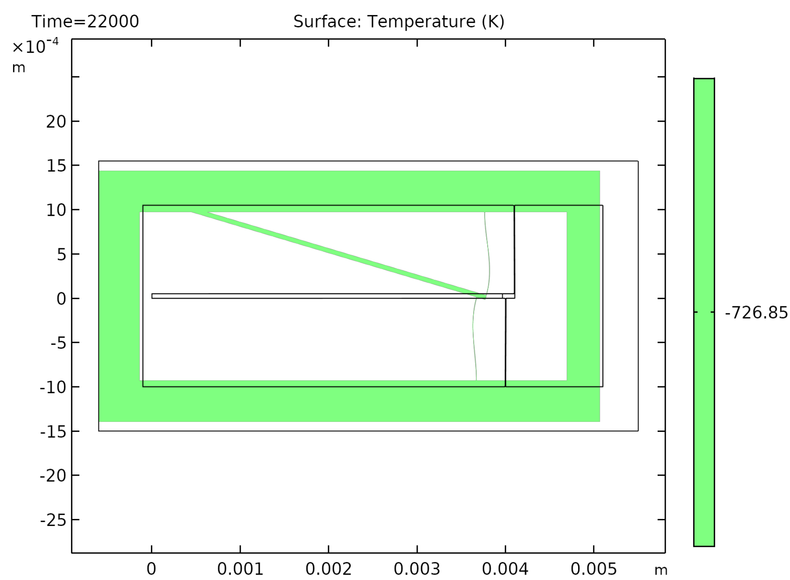

Figure B.3: Nonlinear buckling analysis for a deformed initial shape with 4 μm beams. Displacements are scaled 10X.

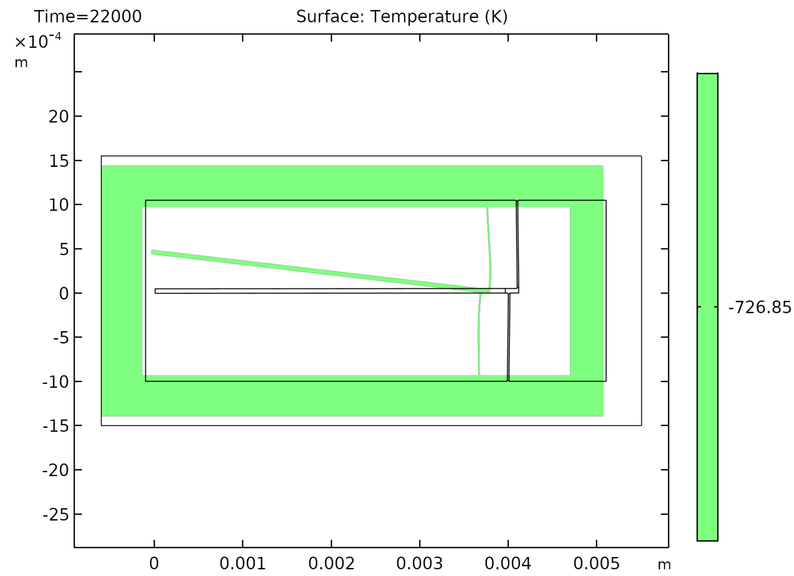

Figure B.4: Nonlinear buckling analysis for a deformed initial shape with 16 μm beams. Displacements are scaled 10X.

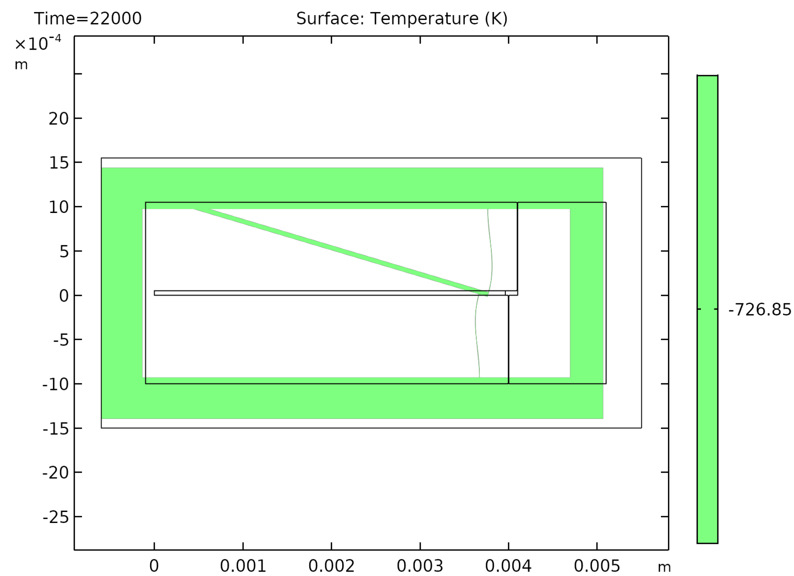

Figure B.5: Nonlinear buckling analysis for an undeformed initial shape with 4 μm beams. Displacements are scaled 10X.

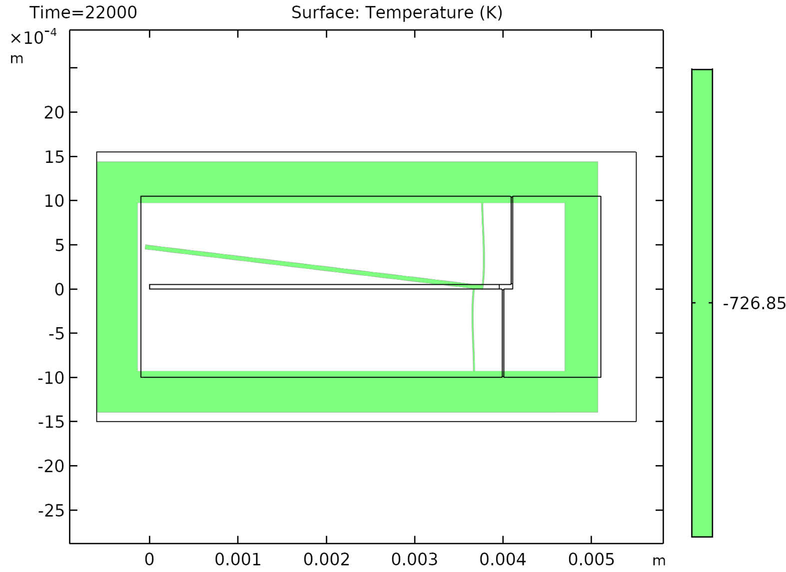

Figure B.6: Nonlinear buckling analysis for n undeformed initial shape with 16 μm beams. Displacements are scaled 10X.

B.2 Stiffness analysis

In this section, the stress as a result of stiffness is compared to the stress induced by the thermal strain. The axial stress as a result of the bending of the beams is analytically calculated, as well as simulated in COMSOL. Due to symmetry of the mechanism, we analyze only half. Elongation of the strain beams cause the lever to rotate, which induces bending in the beams. This bending results in a net axial stress in the silicon. The schematic used for this calculation is shown in figure B.7. Elongation of the strain beam gives a rotation angle:

$$\theta = \frac{\varepsilon L}{O/2} = \frac{2\varepsilon L}{O} \tag{B.1}$$

Bending the beam with angle θ gives an internal moment M in point p_1, which is derived from linear beam theory:

$$M = \frac{4EI\theta}{L} = \frac{8EI\varepsilon}{O} \tag{B.2}$$

Moment equilibrium around point p_2 requires:

$$F = \frac{M}{O/2} = \frac{2M}{O} = \frac{16EI\varepsilon}{O^2} \tag{B.3}$$

EI for a composite material with silicon and silicon dioxide is:

$$EI = E_{si}I_{si} + E_{sio2}I_{sio2} \tag{B.4}$$

Referring to the cross section in figure A.1, I for silicon and silicon dioxide are:

$$I_{si} = \frac{hw^3}{12} \tag{B.5}$$

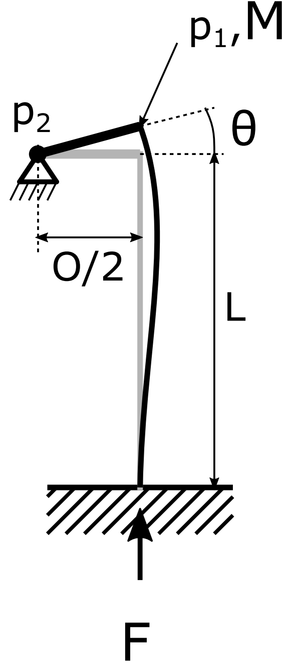

Figure B.7: Schematic for stiffness calculation.

$$I_{sio2} = \frac{(h+2t)(w+2t)^3}{12} - \frac{hw^3}{12} \tag{B.6}$$

The average axial stress in the beam cross section is then:

$$\sigma = \frac{F}{A} = \frac{16EI\varepsilon}{AO^2} \tag{B.7}$$

Where

$$A = (w+2t)(h+2t) \tag{B.8}$$

For $\varepsilon = 0.005\,\%$ strain and parameter values as shown in table B.1, σ is equal to 0.11 MPa. This is also simulated using COMSOL, which gives a result of 0.10 MPa, which is similar. However, this is the average stress in the cross section of the beam, which is not necessarily equal to the axial stress in silicon. Strain in silicon and silicon dioxide must be equal, as they are connected to each other:

$$\varepsilon_{si} = \varepsilon_{sio2} = \frac{\sigma_{si}}{E_{si}} = \frac{\sigma_{sio2}}{E_{sio2}} \tag{B.9}$$

Rewriting gives:

$$\sigma_{sio2} = \frac{E_{sio2}\sigma_{si}}{E_{si}} \tag{B.10}$$

Force equilibrium requires:

$$F = \sigma_{si}A_{si} + \sigma_{sio2}A_{sio2} \tag{B.11}$$

Combining equations gives:

$$\sigma_{si} = \frac{F}{A_{si} + \frac{A_{Sio2}E_{sio2}}{E_{si}}} = \frac{16EI\varepsilon}{O^2\left(A_{si} + \frac{A_{Sio2}E_{sio2}}{E_{si}}\right)} \tag{B.12}$$

Where

$$A_{si} = wh \tag{B.13}$$

And

$$A_{sio2} = (w+2t)(h+2t) - wh \tag{B.14}$$

For the same parameter values, this gives a stress of 0.09 MPa in the silicon beam as a result of stiffness. The total axial stress in the silicon, which is the sum of thermal stress from the oxide and the stress from stiffness, is equal to 5.70 MPa, as calculated in COMSOL. The stress as a result of stiffness is thus only in the order of 1.6 %. For the 15 µm wide beam, this is 3.3 %, which is still very acceptable. We can therefore conclude that the stress as a result of the stiffness of the mechanism can be neglected in the simulations in the numerical model.

Table B.1: Parameter values stiffness analysis

Parameter	Value
E_{si}	110 GPa
E_{sio2}	64 GPa
h	50 µm
w	10 µm
t	1 µm
O	100 µm

B.3 Sensitivity analysis

This sensitivity analysis shows the influence of changes in model parameters to the elastic and plastic strain.

Sensitivity S is defined as:

$$S = \frac{\frac{\partial y}{y}}{\frac{\partial x}{x}} = \frac{\partial y}{\partial x}\frac{x}{y} \tag{B.15}$$

Where y is the model outcome, which can be the elastic or plastic strain, and x a model parameter.

The partial derivatives cannot be calculated analytically, because the model must be solved numerically. Therefore, the partial derivatives are calculated with using central finite differences:

$$\frac{\partial y}{\partial x} = \frac{y\left(x+\frac{1}{2}h\right) - y\left(x-\frac{1}{2}h\right)}{h} \tag{B.16}$$

Where h is a small compared to x. For this study, h was chosen to be 5% of x for all parameters. The sensitivity analysis is performed for $A_r = 0.5$ at 3 different oxidation temperatures. The results are shown in table B.2 and B.3.

Model predictions for plastic strain are very insensitive for $\dot{T}$, A_r, E_{Si}, E_{SiO_2}, α_{SiO_2}, and $N_{m,0}$. α_{Si} has a significantly larger sensitivity, but still less than 1. This means that a relative change or deviation of α_{Si} will have an impact on the plastic strain of the same order of relative magnitude. We can conclude that there are no excessive sensitivities for plastic strain. The model predictions for elastic strain are not extremely sensitive for the parameter deviations. All sensitivities are below an absolute value of 1. There is a very low sensitivity for $\dot{T}$ and α_{SiO_2}.

Table B.2: Sensitivity on plastic strain

Parameter	S(900 °C)	S(1000 °C)	S(1100 °C)
$\dot{T}$	-0.28	0.10	0.12
A_r	0.02	0.06	0.16
E_{Si}	0.01	0.02	0.10
E_{SiO_2}	0.01	0.02	0.17
α_{Si}	0.78	0.83	0.66
α_{SiO_2}	-0.15	-0.16	-0.01
$N_{m,0}$	-0.01	0	0.17

Table B.3: Sensitivity on elastic strain

Parameter	S(900 °C)	S(1000 °C)	S(1100 °C)
$\dot{T}$	0.01	-0.03	0.31
A_r	0.79	0.66	0.99
E_{Si}	-0.83	-0.95	-0.83
E_{SiO_2}	0.79	0.66	0.81
α_{Si}	0.72	0.72	0.54
α_{SiO_2}	-0.14	-0.14	-0.26
$N_{m,0}$	0	0	0.03

Appendix C

Mask design

This appendix contains details on the mask design. Fig. C.1 shows the final mask used to produce the samples. Fig. C.2 shows CAD renders of the design, made in SolidWorks. A DRIE test was done to predict the overetching. This is shown in Fig. C.3. This shows an average deviation of 0.6 µm. The beams are thus designed with an addition 0.6 µm width for overetching compensation, and an additional 0.88 µm to compensate for consumed silicon by the oxide.

Break points were used to keep the samples attached to the wafer during fabrication. The break points worked well, the samples were easily release with a small touch with tweezers. Each sample was held to the wafer by 12 fixed points in the epitaxial layer. Future design could use slightly larger contact points, as some samples from the <100> oriented wafer were accidentally released during fabrication.

Fall out blocks were used in the epitaxial layer to reduce stress on thin silicon features induced by the sacrificial oxide layer. This worked well for most samples. However, some of the blocks were still attached to some of the samples. In the future, this could be prevented by using smaller blocks or wider etch trenches.

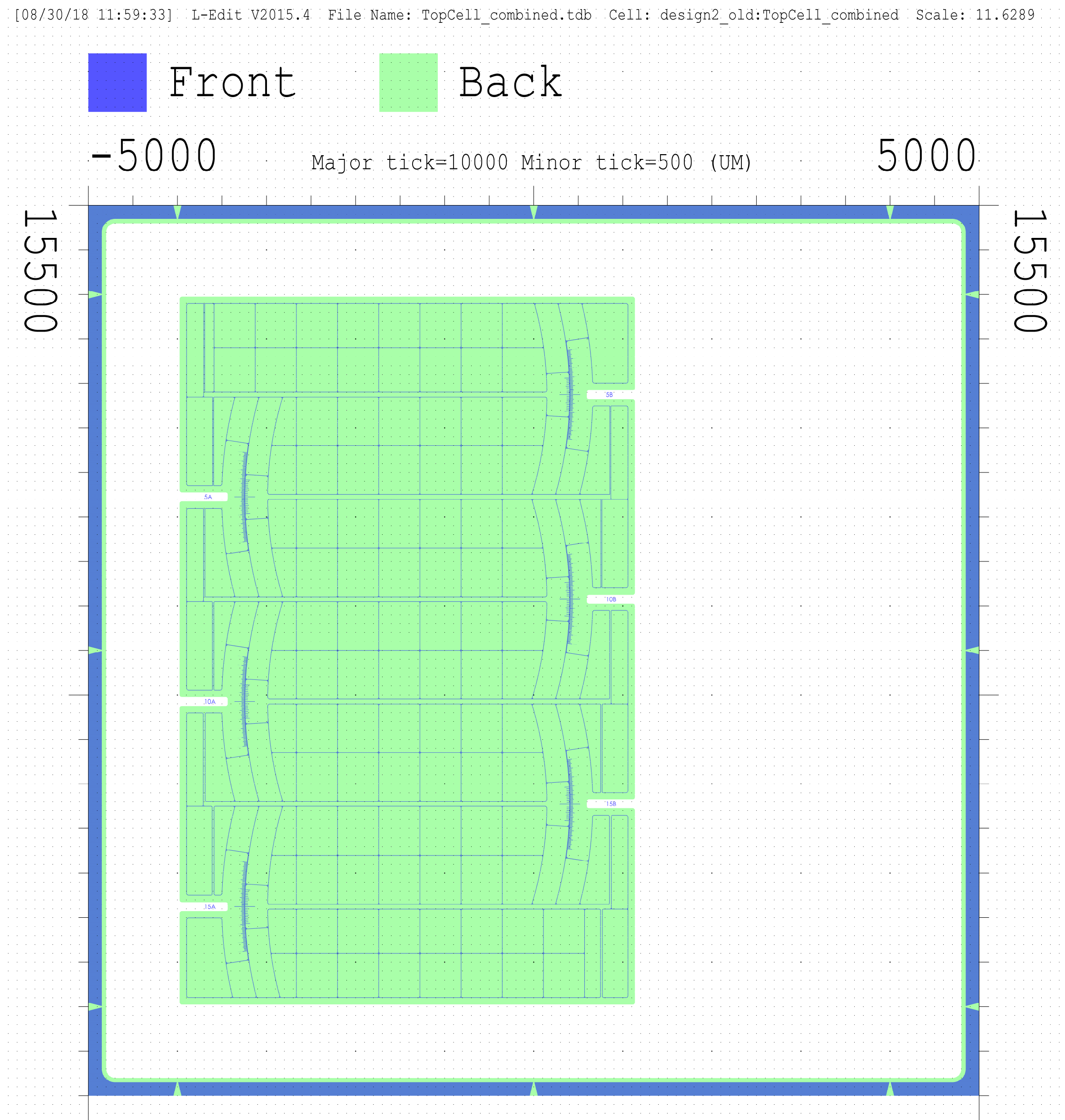

Figure C.1: Final mask design.

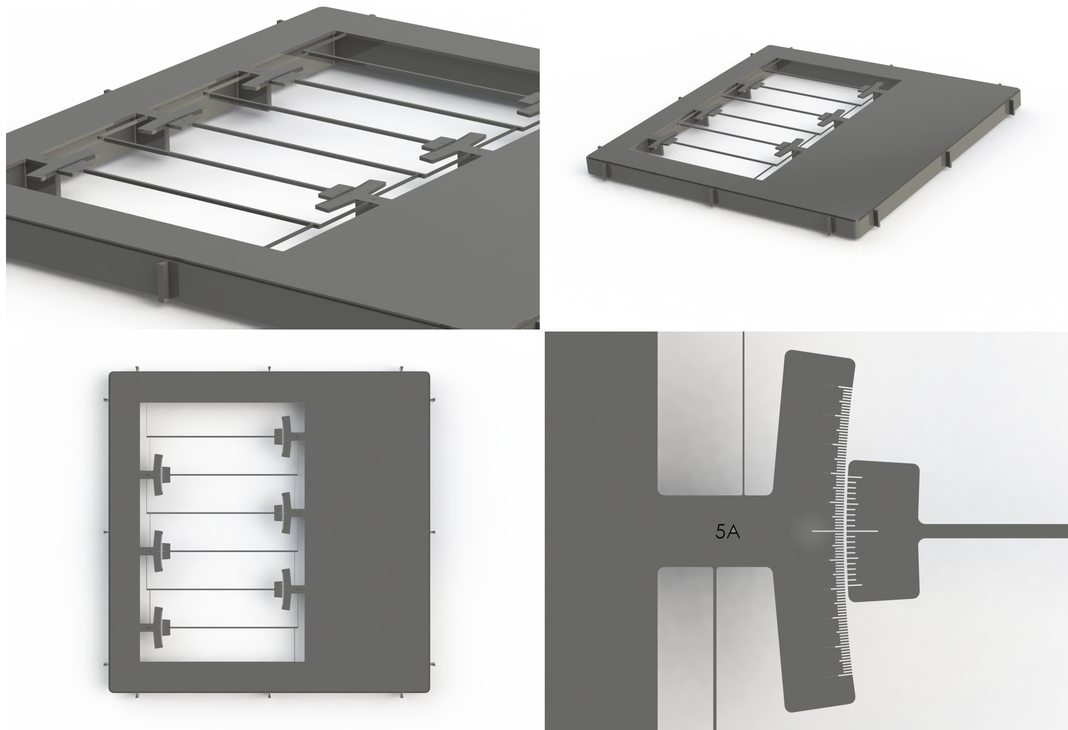

Figure C.2: CAD renders of the sample.

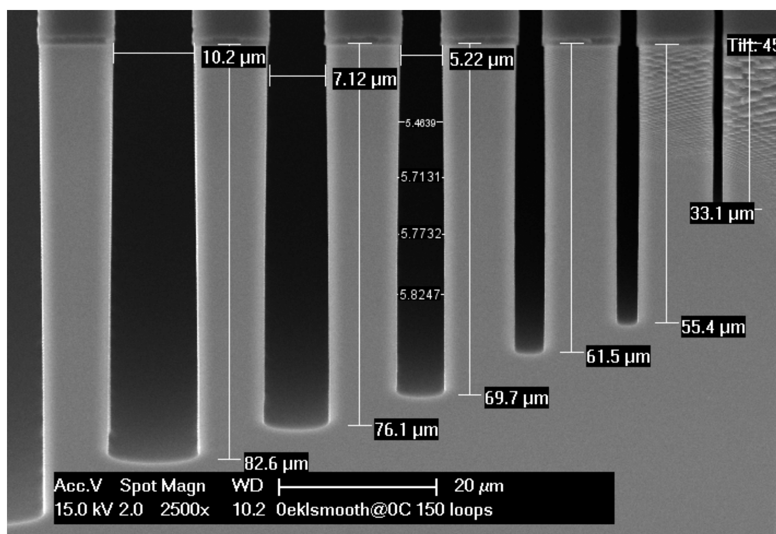

Figure C.3: Overetching measurement of DRIE test. For the 5 µm mask, the average overetching to a depth of 50 µm is 0.6 µm.

Appendix D

Sample images

(a) Broken beam

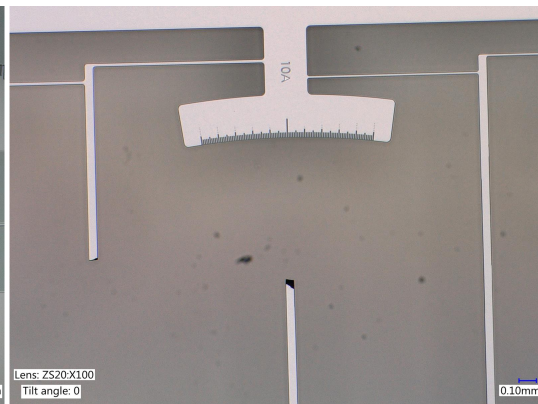

(b) Broken levers

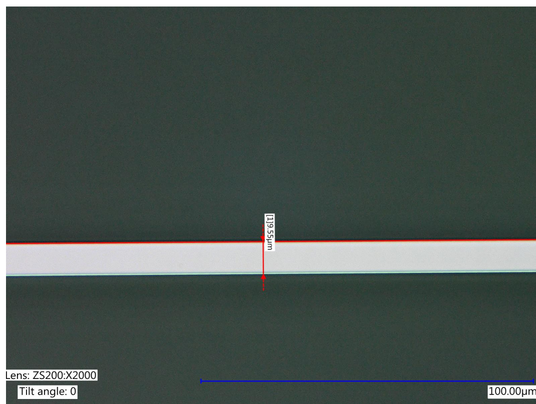

(c) Example of a beam width measurement.

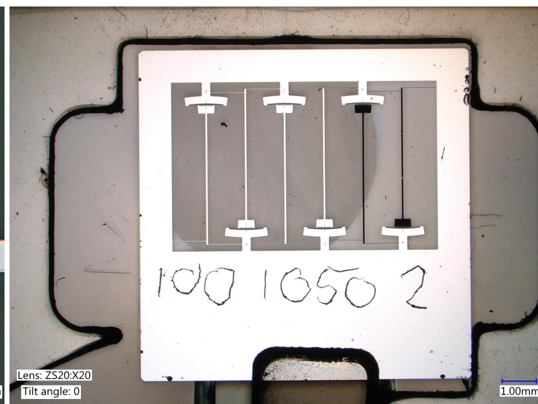

(d) Sample which shows out of plane deflection of 2 levers on the right. After a small touch with tweezers, they sprung back.

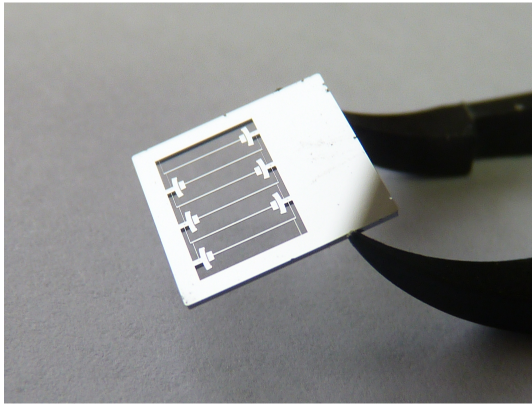

(a) Frontside of a sample.

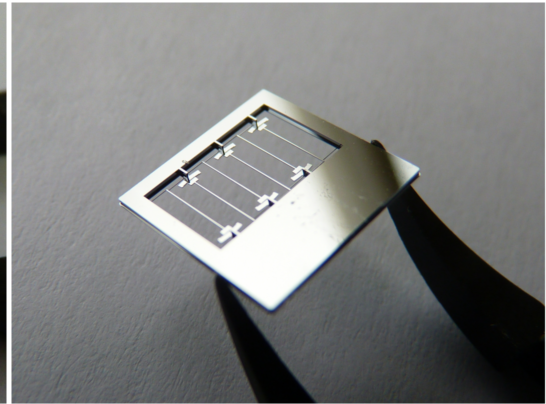

(b) Backside of a sample. The backside cavity is visible.

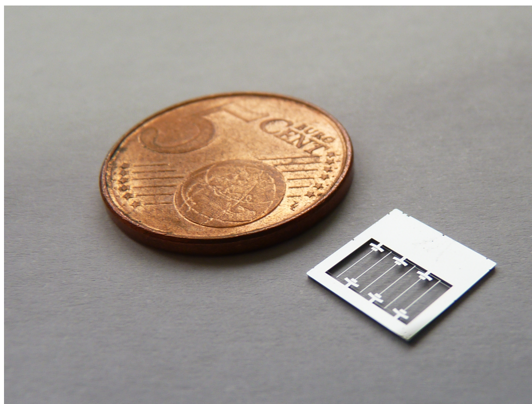

(c)

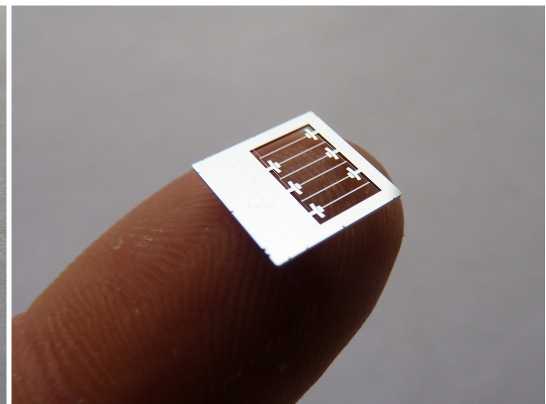

(d) .

Appendix E

Sample holder drawings

Custom sample holders were made to minimize damage to the samples. Lasercut PMMA parts are assembled as shown in Fig. E.1. The technical drawings are also included in this appendix.

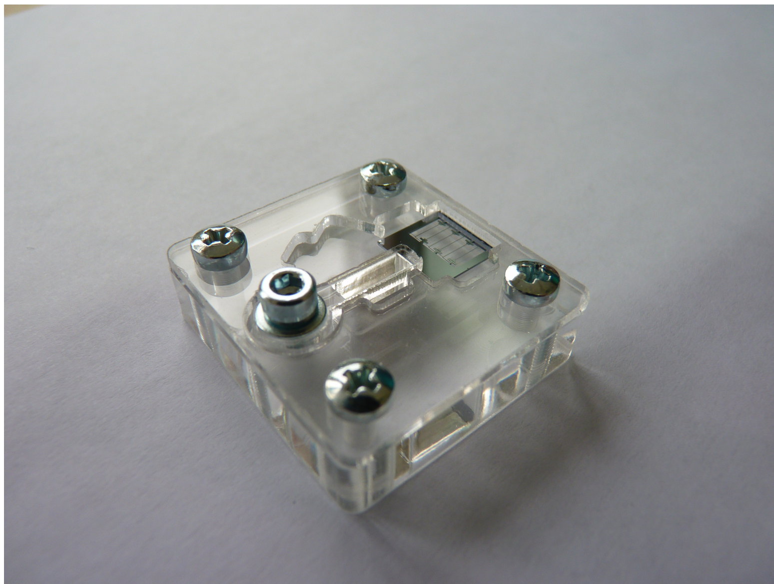

Figure E.1: Sample holder

4 3 2 1

F

E

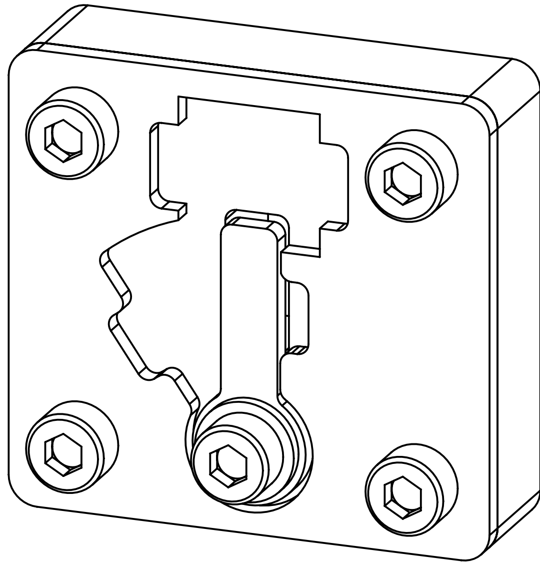

D

C

B

A

UNLESS OTHERWISE SPECIFIED: DIMENSIONS ARE IN MILLIMETERS SURFACE FINISH: TOLERANCES: LINEAR: ANGULAR:	FINISH:	DEBURR AND BREAK SHARP EDGES	DO NOT SCALE DRAWING	REVISION

	NAME	SIGNATURE	DATE		
DRAWN					
CHK'D					
APPV'D					
MFG					
Q.A				MATERIAL:	
				WEIGHT:	

TITLE:

Sample holder assembly

DWG NO.

A4

SCALE:2:1

SHEET 1 OF 1

4 3 2 1

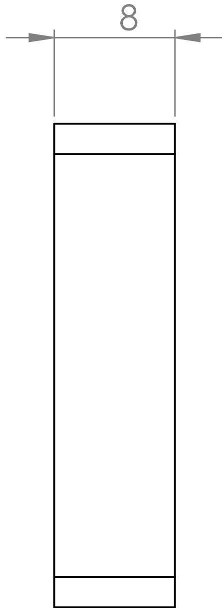

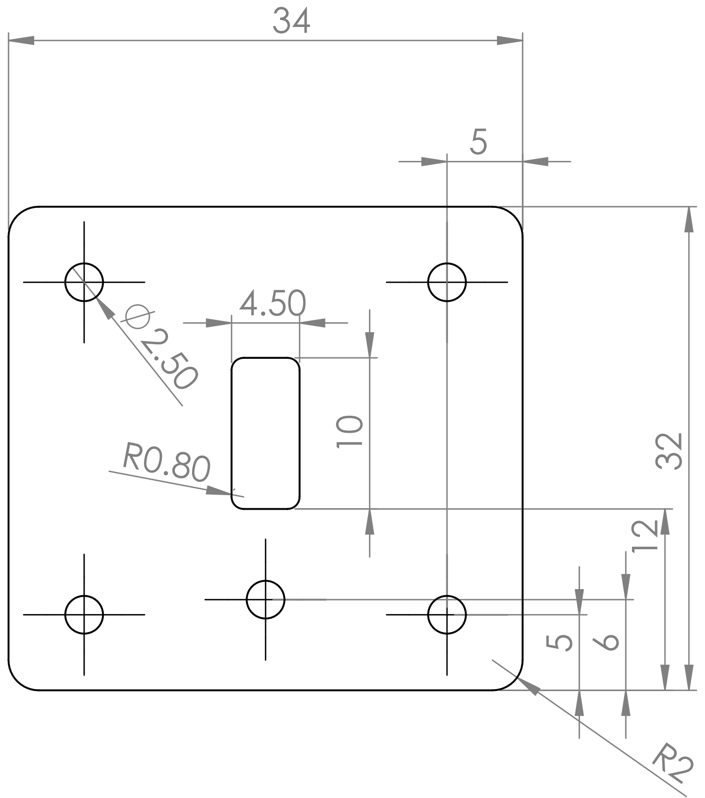

UNLESS OTHERWISE SPECIFIED: DIMENSIONS ARE IN MILLIMETERS SURFACE FINISH: TOLERANCES: LINEAR: ANGULAR:	FINISH:	DEBURR AND BREAK SHARP EDGES	DO NOT SCALE DRAWING	REVISION

	NAME	SIGNATURE	DATE		
DRAWN					
CHK'D					
APPV'D					
MFG					
Q.A				MATERIAL:	
				WEIGHT:	

TITLE:

Sample holder base

DWG NO.	A4
SCALE:2:1	SHEET 1 OF 1

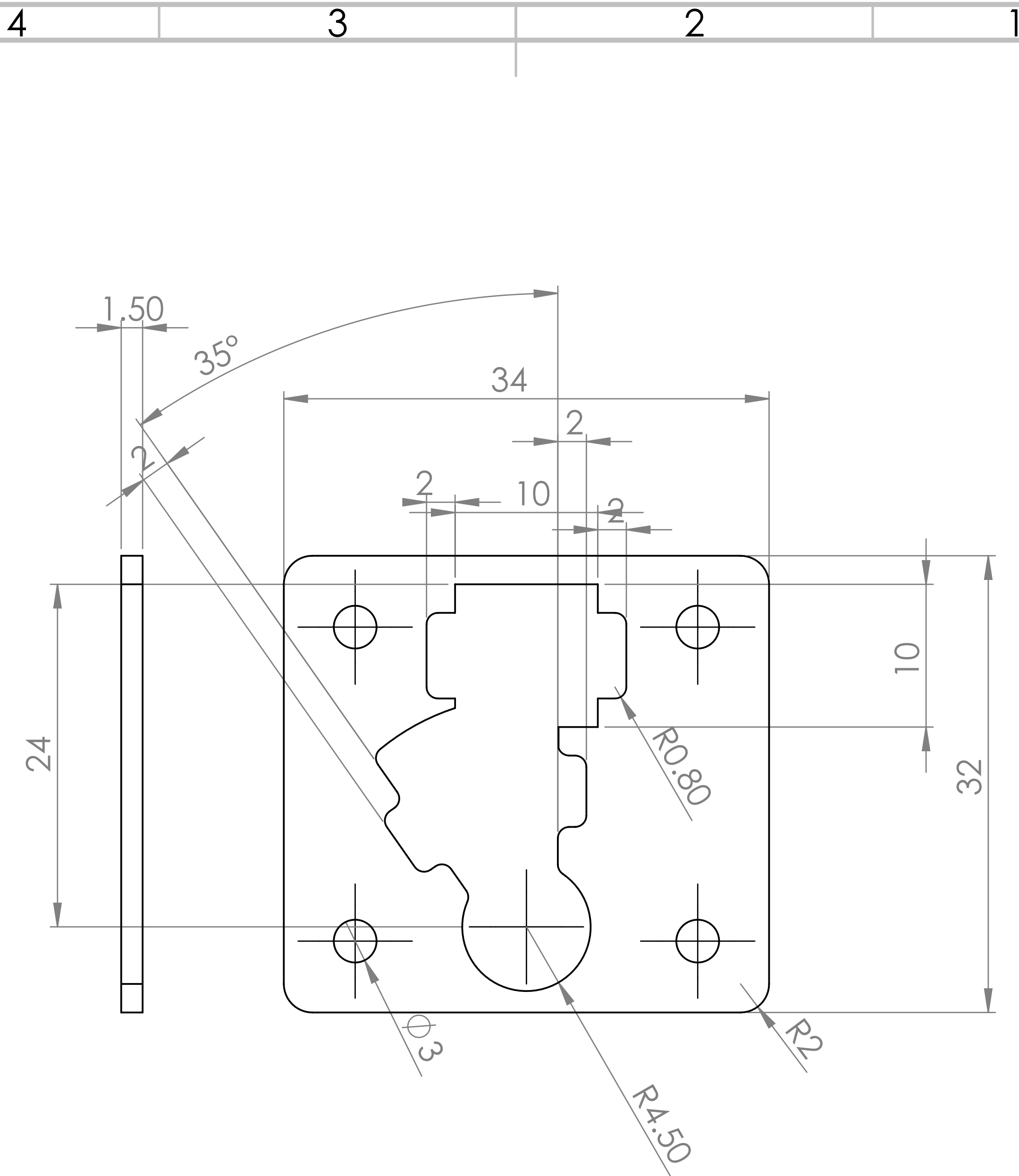

UNLESS OTHERWISE SPECIFIED:
DIMENSIONS ARE IN MILLIMETERS
SURFACE FINISH:
TOLERANCES:
LINEAR:
ANGULAR:

FINISH:

DEBURR AND BREAK SHARP EDGES

DO NOT SCALE DRAWING

REVISION

	NAME	SIGNATURE	DATE
DRAWN			
CHK'D			
APPV'D			
MFG			
Q.A			

TITLE:

Sample holder top

MATERIAL:

PMMA

WEIGHT:

DWG NO.

A4

SCALE:2:1

SHEET 1 OF 1

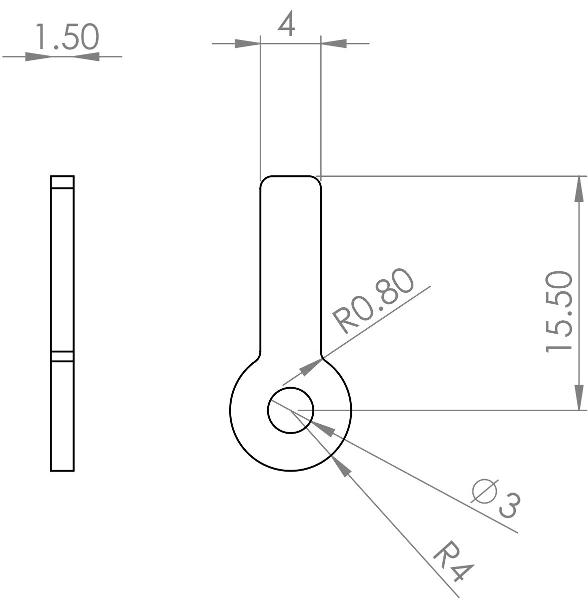

UNLESS OTHERWISE SPECIFIED: DIMENSIONS ARE IN MILLIMETERS SURFACE FINISH: TOLERANCES: LINEAR: ANGULAR:	FINISH:	DEBURR AND BREAK SHARP EDGES	DO NOT SCALE DRAWING	REVISION

	NAME	SIGNATURE	DATE	TITLE:
DRAWN				Sample holder clamp
CHK'D				
APPV'D				
MFG				
Q.A				MATERIAL: DWG NO. A4
				WEIGHT: SCALE:2:1 SHEET 1 OF 1

Appendix F

Measurement data

This appendix contains the raw measurement data of the experiments.

Date	Oxidation temperature	Furnace	Oxide thickness [nm]	Annealing time	Orientation	Marking	Beam	Beam thickness [um]			Initial displacement [um]	Total displacement [um]	Disp. after ox. removal [um]
18-Oct	1100 °C	B2	1004.16	16h	100	100 1100-1	5a				-2	59	3
							5b	4.54	4.31	4.42	-1	54	-1
							10a				0	32	2
							10b	9.44	9.55	10.11	-1	29	-1
							15a				-3	21	-1
							15b	14.67	14.56	14.78	-1	20	-1
					110	110 1100-1	5a				-3	40	-5
							5b	4.94	5.06	4.71	-3	40	-2
							10a				-3	23	-2
							10b	9.59	9.94	9.6	-2	22	-1
							15a				-3	16	-1
							15b	14.83	15.06	14.83	-2	14	-3
19-Oct	900 °C	D1	802.31 802.09 800.13	60h	100	100 900-1	5a				-3	45	-1
							5b	5.43	5.53	5.09	-2	47	0
							10a				-2	26	0
							10b	10.45	10.34	10.11	-2	25	-1
							15a				-3	18	-1
							15b	15.14	15.14	15.47	-2	18	-1
					110	110 900-1	5a				-3	36	-1
							5b	6.06	6.06	5.39	-3	38	1
							10a				-3	21	0
							10b	10.19	10.19	10.08	-2	21	0
							15a				-2	16	0
							15b	15.43	15.32	15.77	-2	16	1
22-Oct	950 °C	D1	943.79 938.93 938.30	16h	100	100 950-2	5a				-3	45	-2
							5b	5.26	5.43	5.22	-2	45	-2
							10a				-1	27	1
							10b	10.15	10.15	10.26	-2	26	-1
							15a				-2	19	-1
							15b	15.29	14.96	15.29	-2	19	0
					110	110 950-1	5a				-4	36	-3
							5b	5.58	5.24	5.69	-3	39	0
							10a				-3	22	-2
							10b	10.59	10.15	10.48	-3	21	-1
							15a				-3	16	0
							15b	15.72	15.39	15.4	-3	15	-1
22-Oct	1100 °C	B2	1994.79 1993.80 1993.75	16h	100	100 1050-2	5a				-3	99	0
							5b	2.81	3.04	2.92	-3	100	-2
							10a				-1	58	0
							10b	7.63	7.61	7.95	-2	57	0
							15a				-3	42	0
							15b	12.52	12.85	12.63	-2	40	-1
					110	110 1000-2	5a				-4	98	1
							5b	2.65	2.65	3.09	-3	85	0
							10a				-4	53	1
							10b	7.59	7.73	7.2	-3	46	-1
							15a				-3	39	2
							15b	12.59	12.5	12.38	-3	32	-1

Date	Oxidation temperature	Furnace	Oxide thickness [nm]	Annealing time	Orientation	Marking	Beam		Beam thickness [um]		Initial Displacement [um]	Total displacement [um]	Displacement after oxide removal [um]
22-Oct	1100 °C	B2	1996.87 1996.40 1996.02	30h	100	100 900-2	5a				-2	101	-1
							5b	2.79	2.91	3.02	-2	102	0
							10a				1	61	2
							10b	7.83	7.7	8.03	-1	56	0
							15a				-1	45	1
							15b	12.75	12.53	12.41	-1	40	0
					110	110 1100-2	5a				-4	80	-3
							5b	2.97	2.85	2.62	-3	79	-2
							10a				2	90	0
							10b	7.31	7.87	7.98	-3	43	-2
							15a				-5	32	-1
							15b	12.67	12.67	12.89	-3	30	0
23-Oct	1000 °C	D1	966.19 964.29 965.67	16h	100	100 1000-1	5a				-3	47	-3
							5b	5.55	5.44	5.43	-2	48	-2
							10a				-2	29	0
							10b	10.11	10.67	10.69	-1		
							15a				-4	19	-1
							15b	15.13	15.58	15.45	-2	19	-1
					110	110 1000-1	5a				-5	38	-5
							5b	4.99	4.85	5.08	-4	39	-2
							10a				-3	20	-2
							10b	10.1	10.1	10.19	-3	21	-1
							15a				-4	16	-1
							15b	15.04	14.8	15	-3	14	-3
24-Oct	1050 °C	D1	985.55 985.55 988.09	16h	100	100 1050-1	5a				-4	53	-3
							5b	4.91	5.13	5.13	-2	53	-2
							10a				-1	33	-2
							10b	9.93	10.49	9.81	-2	29	-2
							15a				-3	21	-2
							15b	15.06	15.17	14.85	-2	21	-2
					110	110 1050-1	5a				-4	40	-3
							5b	5.1	5.33	5.12	-2	38	-2
							10a				-2	22	-4
							10b	10.26	10.26	10.03	-3	21	-3
							15a				-4	17	-2
							15b	15.28	15.17	14.72	-3	15	-2

Bibliography

[1] Yin Zhang and Ya-pu Zhao. An effective method of determining the residual stress gradients in a micro-cantilever. *Microsystem technologies*, 12(4):357–364, 2006.

[2] Fariborz Maseeh and Stephen D Senturia. Plastic deformation of highly doped silicon. Technical report, Massachusetts Inst of Tech, 1989.

[3] Seungmock Lee, Tsunehisa Tanaka, and Koji Inoue. Residual stress influences on the sensitivity of ultrasonic sensor having composite membrane structure. *Sensors and Actuators A: Physical*, 125(2):242–248, 2006.

[4] Jongbaeg Kim, Hyuck Choo, Liwei Lin, and Richard S Muller. Microfabricated torsional actuators using self-aligned plastic deformation of silicon. *Journal of Microelectromechanical Systems*, 15 (3):553–562, 2006.

[5] Ichiro Yonenaga. An overview of plasticity of si crystals governed by dislocation motion. *Engineering Fracture Mechanics*, 147:468–479, 2015.

[6] Bing Gao, Satoshi Nakano, H Harada, Y Miyamura, and K Kakimoto. Effect of cooling rate on the activation of slip systems in seed cast-grown monocrystalline silicon in the [001] and [111] directions. *Crystal Growth & Design*, 13(6):2661–2669, 2013.

[7] Koji Sumino. Deformation behavior of silicon. *Metallurgical and Materials Transactions A*, 30(6): 1465–1479, 1999.

[8] Deformation of single crystals. URL `http://academic.uprm.edu/pcaceres/Courses/MechMet/MET-3A.pdf`.

[9] E Orowan. Problems of plastic gliding. *Proceedings of the Physical Society*, 52(1):8, 1940.

[10] H Alexander and P Haasen. Dislocations and plastic flow in the diamond structure. In *Solid state physics*, volume 22, pages 27–158. Elsevier, 1969.

[11] Ichiro Yonenaga and K Sumino. Dislocation dynamics in the plastic deformation of silicon crystals ii. experiments. *Physica status solidi (a)*, 51(2):217, 1979.

[12] Ichiro Yonenaga and K Sumino. Dislocation dynamics in the plastic deformation of silicon crystals i. experiments. *Physica status solidi (a)*, 50(2):685–693, 1978.

[13] Alex Masolin, Pierre-Olivier Bouchard, Roberto Martini, and Marc Bernacki. Thermo-mechanical and fracture properties in single-crystal silicon. *Journal of Materials Science*, 48(3):979–988, 2013.

[14] EA Irene, E Tierney, and J Angilello. A viscous flow model to explain the appearance of high density thermal sio2 at low oxidation temperatures. *Journal of the Electrochemical Society*, 129 (11):2594–2597, 1982.

[15] Matthew A Hopcroft, William D Nix, and Thomas W Kenny. What is the young's modulus of silicon? *Journal of microelectromechanical systems*, 19(2):229–238, 2010.

[16] C Bourgeois, E Steinsland, N Blanc, and NF De Rooij. Design of resonators for the determination of the temperature coefficients of elastic constants of monocrystalline silicon. In *Frequency Control Symposium, 1997., Proceedings of the 1997 IEEE International*, pages 791–799. IEEE, 1997.

[17] Haruna Tada, Amy E Kumpel, Richard E Lathrop, John B Slanina, Patricia Nieva, Paul Zavracky, Ioannis N Miaoulis, and Peter Y Wong. Thermal expansion coefficient of polycrystalline silicon and silicon dioxide thin films at high temperatures. *Journal of Applied Physics*, 87(9):4189–4193, 2000.

[18] Yasumasa Okada and Yozo Tokumaru. Precise determination of lattice parameter and thermal expansion coefficient of silicon between 300 and 1500 k. *Journal of Applied Physics*, 56(2):314–320, 1984.